Autonomous Wheel Off-Loading Strategies for Deep-Space CubeSats

Author: Andrea Pizzetti

Advisor: Prof. Francesco Topputo

Co-advisor: Antonio Rizza

Academic year: 2020-2021

1. Introduction

In the last years, the space sector has been characterized by a strong push in the nano-satellite class development enabling possibilities that before could only be dreamed. When they were first designed, CubeSats were addressed to Earth-observation missions in Low Earth Orbits (LEO), mainly for educational purposes, but in recent years it has been proven that they can be used also for interplanetary missions, with a high scientific return. Following the success of MarCO, several deep-space CubeSats missions have been scheduled, such as NEA Scout, Lunar IceCube, Lumio, VMMO, Juventas & Milani and M-Argo [1]. All of them use Reaction Wheels (RWs) to reject the attitude disturbances and control the orientation of the platform. A RW is a highly reactive and precise actuator; however, when the wheel reaches its maximum angular rate, it is said to be saturated and the angular momentum must be unloaded from it by external means, otherwise it can no more produce torques.

The scope of the dissertation is the demonstration of novel and autonomous techniques for the RWs *desaturation*, a procedure also known as Wheel Off-Loading (WOL). The developed strategies will not employ the use of any ded-

icated momentum-management device that is usually carried on-board, like Reaction Control System (RCS) or Magnetotorquers. Instead, they will exploit components of the Spacecraft (S/C) that are devoted to other main duties: the propulsion system, if coupled with a pointing mechanism, and the Solar Arrays (SAs), if they can be differently tilted by a Solar Array Drive Mechanism (SADM).

One of the most important motivation for this work is the fact that RCS and Magnetotorquers require respectively the presence of additional propellant and magnetic field to properly work. These are not resources easily available in deep-space missions, where the satellite has heavy constraints in terms of mass and spends most of its lifetime in heliocentric orbits far from the magnetic influence of the planets. Instead, employing the same thruster that is used for the orbital cruising also for de-saturation allows to keep on-board only the main propellant tank and save mass thanks to the inherent higher efficiency of thrusters with respect to RCS. Furthermore, strategies based on SAs require solar illumination, which is typically always achieved in interplanetary missions.

The techniques will be therefore demonstrated using a deep-space mission as a test-case scenario. The choice has fallen on the Minia-

turised Asteroid Remote Geophysical Observer (M-Argo), a 12 Unit (U) CubeSat aiming to rendezvous with a Near-Earth Asteroid (NEA) after an autonomous deep-space travel. The satellite is characterized by an assembly of 4 RWs, a gimballed gridded ion thruster, and two large SAs. It is therefore the perfect candidate to prove these techniques. Moreover, since the CubeSat platforms are very good technology demonstrators and they experienced exponential success in the last years, it is natural to consider this class of satellites, in view of a future in-orbit demonstration.

2. Case Study

THE CubeSat will be released in a parking orbit around the Sun-Earth L2 point between 2023 and 2024. A NEA target screening has been carried out during the mission analysis phase to identify the envelope of the most promising asteroids reachable by M-Argo in the provided time frame. In this work, the fuel-optimal trajectory to reach asteroid 2010-UE51 will be considered since it grants both the shortest Time of Flight (TOF) and lowest fuel consumption. The correspondent thrust profile, reported in *Figure 1*, presents *thrust bins* because it is characterized by 1-week activity segments, where cruising arcs of 6 days and coasting arcs of 1 day are identified during which the thruster is switched on and off respectively [2].
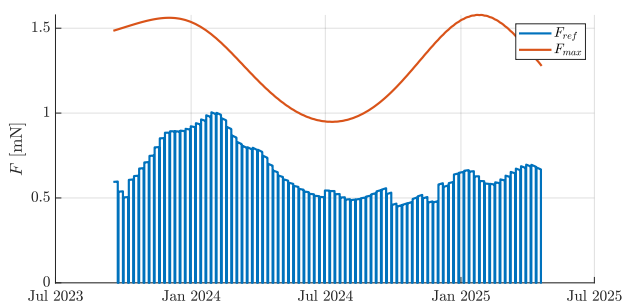

Figure 1: Maximum and reference thrust during the fuel-optimal trajectory

The cruising arc that gives the worst-case scenario is the one where there is the lowest difference between the reference thrust level and the maximum one. This is explained by the fact that during WOL the thrust will likely need to be higher than the reference value due to the offsetting of the gimbal. According to these consider-

ations, the chosen cruising arc is between 4 and 10 February 2024. The WOL strategies based on SAs can be simulated in any coasting arc because there are no restrictions in terms of thrust. For simplicity, the coasting arc chosen is consequent to the cruising one.

For what concerns the S/C, its properties are reported in *Table 2* and a rendering in packed and deployed configuration can be seen in *Figure 2*. M-Argo is characterized by two huge SAs, each one with 4 6U-XL panels. The absorption, specular and diffusive coefficients considered are the ones associated with anodized aluminum for the body faces and the last-generation solar cells for the Solar Panels (SPs).
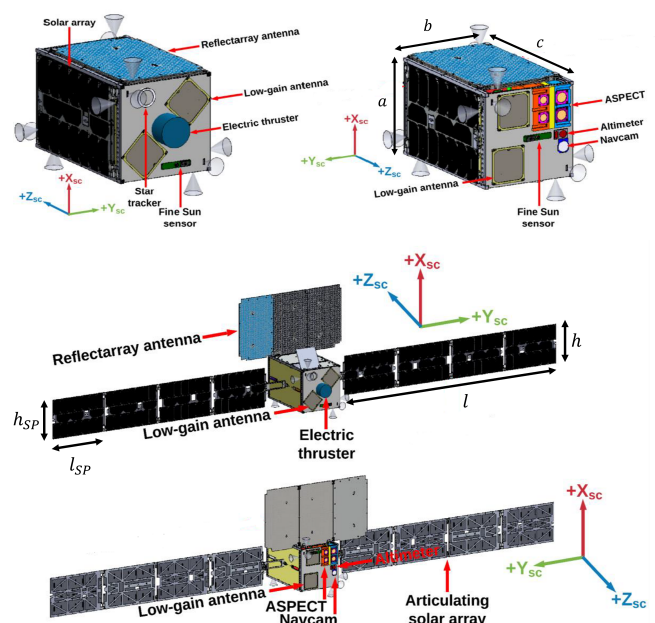

Figure 2: M-Argo in packed and deployed configuration. Courtesy of GomSpace [3]

The CubeSat encompasses 4 RWs in a pyramid configuration along -x and a set of 12 RCS distributed in triads in the corners. The actuators data is reported in *Table 1*.

RWs		RCS	
T_{max}	2 mNm	F_{max}	1 mN
h_{max}	19 mNms	I_{sp}	16 s

Table 1: Data of M-Argo actuators [3]

The propulsion system is radiofrequency-based gridded ion engine with a gimbal mechanism that can have excursions up to 15°. Xenon is

Body	
a	$0.25\,\text{m}$
b	$0.25\,\text{m}$
c	$0.366\,\text{m}$
m_{tot}	$27.5\,\text{kg}$

SP	
h_{SP}	$0.209\,\text{m}$
l_{SP}	$0.3265\,\text{m}$
m_{SP}	$0.453\,\text{kg}$

SA	
h	$0.209\,\text{m}$
l	$1.306\,\text{m}$
m_{SW}	$1.812\,\text{kg}$
l_h	$0.1633\,\text{m}$

	Body	SP
ρ_s	0.8	0.0727
ρ_d	0.08	0.007

Table 2: Physical and optical properties of M-Argo body, solar panels and solar arrays [3–5]

used as propellant by both thruster and RCS and stored in shared tanks. The maximum thrust level and specific impulse are computed through 4th order polynomial fitting from the input power, which is in turn retrieved from the S/C distance from the Sun.

3. WOL Strategies

THREE reference frames are identified in *Figure 3*. Other than the inertial frame XYZ, denoted with n, and the body frame xyz, denoted with b, the pointing frame $\delta\beta\alpha$, denoted with p, is also defined.
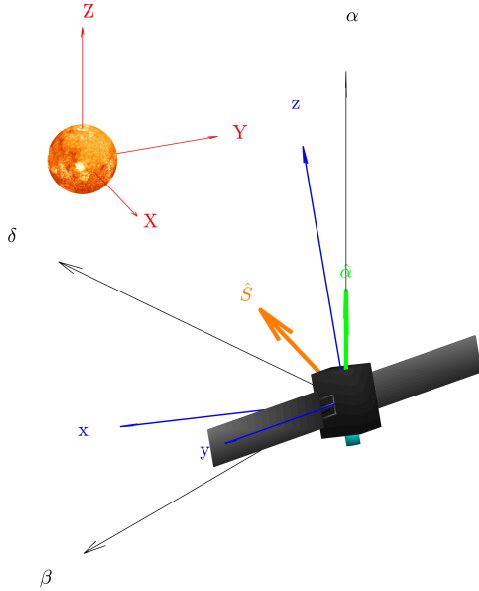

Figure 3: Inertial, pointing and body frames

This frame is slowly rotating according to the s/c pointing vector $\hat{\boldsymbol{\alpha}}$ and to the sun direction $\hat{\boldsymbol{S}}$: the α-axis is aligned with the pointing vector, the β-axis is perpendicular to the sun direction and to the α-axis, and the δ-axis completes the triad. The orientation of p with respect to n is obtained with (1) in terms of Direction Cosines Matrix (DCM).

$$\alpha = \hat{\boldsymbol{\alpha}}$$
$$A_{p/n} = \begin{bmatrix} \delta & \beta & \alpha \end{bmatrix}^T \qquad \beta = \hat{\boldsymbol{\alpha}} \wedge \hat{\boldsymbol{S}} \qquad (1)$$
$$\delta = (\hat{\boldsymbol{\alpha}} \wedge \hat{\boldsymbol{S}}) \wedge \hat{\boldsymbol{\alpha}}$$

During cruising, b should ideally coincide with p, because the z-axis should be pointed along $\hat{\boldsymbol{\alpha}}$ and the SAs should be aligned perpendicularly to the Sun to maximize the power income. However, during WOL strategies that involve an attitude motion, the two frames could become misaligned. In these cases, it is convenient to express the attitude guidance trajectories of the body with respect to the p frame, using $A_{b/p}$.

3.1. Cruising

The WOL strategies during cruising involve the use of the gimbal mechanism of the thruster to produce torques by off-setting the thrust from the Center Of Mass (COM).
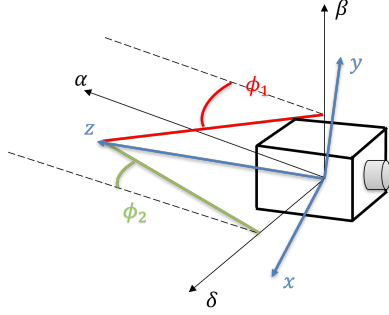
The gimballed thrust direction $\hat{\boldsymbol{g}}$ can be expressed in terms of the excursion angles θ_1 and θ_2 about the y-axis and x-axis respectively:
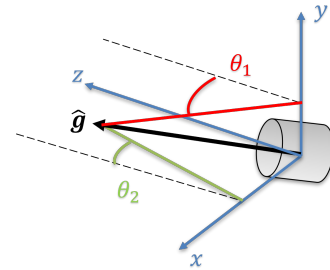
$$\hat{\boldsymbol{g}}_b = \begin{bmatrix} \sin\theta_1 \\ \sin\theta_2 \\ \sqrt{1 - (\sin\theta_1)^2 - (\sin\theta_2)^2} \end{bmatrix}$$

For the strategies that will require an attitude motion, $A_{b/p}$ can be expressed in therms of the attitude angles ϕ_1 and ϕ_2, which represents the

slewing around the β-axis and δ-axis respectively:

$$A_{b/p} = \begin{bmatrix} \cos\phi_1 & 0 & -\sin\phi_1 \\ 0 & \cos\phi_2 & -\sin\phi_2 \\ \sin\phi_1 & \sin\phi_2 & \sqrt{1-(\sin\phi_1)^2-(\sin\phi_2)^2} \end{bmatrix}$$

By imposing the desired angles at each instant, the guidance trajectory for the attitude of the s/c is obtained.

During cruising, the satellite is nominally subjected to a reference thrust force $\boldsymbol{F}_{ref}$ aligned along $\hat{\boldsymbol{\alpha}}$. If the gimbal mechanism is used, the direction of the thrust changes to $\hat{\boldsymbol{g}}$ and the thrust must eventually increase to a new level $F_{com} > F_{ref}$ to still have the same intensity along the pointing vector. In other words, the projection of the actual thrust force $\boldsymbol{F}_{com}$ along $\hat{\boldsymbol{\alpha}}$ must be equal to F_{ref}. This condition can be imposed to obtain the commanded throttle level:

$$\boldsymbol{F}_{ref} = F_{ref}\,\hat{\boldsymbol{\alpha}}$$
$$\boldsymbol{F}_{com} = F_{com}\,\hat{\boldsymbol{g}} = F_{com}\left(A_{n/b}\,\hat{\boldsymbol{g}}_b\right)$$
$$\boldsymbol{F}_{com}\cdot\hat{\boldsymbol{\alpha}} \equiv F_{ref} \quad \rightarrow \quad F_{com} = \frac{F_{ref}}{\left(A_{n/b}\,\hat{\boldsymbol{g}}_b\right)\cdot\hat{\boldsymbol{\alpha}}}$$

3.1.1   Gimbal

The torque components are directly proportional to the sine of the gimbal angles:

$$\boldsymbol{T} = \boldsymbol{d}_{thr}\times\boldsymbol{F}_b = \begin{bmatrix}0\\0\\-\frac{c}{2}\end{bmatrix}\times F\hat{\boldsymbol{g}}_b = F\begin{bmatrix}\frac{c}{2}\sin\theta_2\\-\frac{c}{2}\sin\theta_1\\0\end{bmatrix}$$

The higher the torque, the larger the value of momentum that can be off-loaded. Therefore, the ratio of the angular momentum can be approximated to the ratio of the torques required to dump them:

$$\frac{h_y}{h_x} \approx \frac{T_y}{T_x} = \frac{-\frac{c}{2}\sin\theta_1}{\frac{c}{2}\sin\theta_2} = -\frac{\sin\theta_1}{\sin\theta_2} \qquad (2)$$

The angle that is first imposed is the one associated with the highest angular momentum and is set equal to a pre-selected maximum value of $\theta_{max} = 5\,°$. Depending on the signs of the angular momentum, the other gimbal angle is computed using (3).

$$|h_x| > |h_y| \rightarrow \begin{cases} \theta_2 = -\theta_{max}\,\mathrm{sgn}\,(h_x) \\[2mm] \theta_1 = \arcsin\left(-\frac{h_y}{h_x}\,\sin\theta_2\right) \end{cases}$$

$$|h_x| < |h_y| \rightarrow \begin{cases} \theta_1 = \theta_{max}\,\mathrm{sgn}\,(h_y) \\[2mm] \theta_2 = \arcsin\left(-\frac{h_x}{h_y}\,\sin\theta_1\right) \end{cases} \qquad (3)$$

3.1.2   BETA

In a general case, only torques around x and y axes can be produced. However, this does not imply that the momentum accumulated on z can not be off-loaded. In fact, by coupling a gimbal trajectory with an attitude motion, torques around the α-axis can be obtained, which will eventually dump the momentum on z.

The concept is based on the fact that, as long as no external torques are applied, angular momentum components are conserved in a *fixed* frame. When the attitude changes, and therefore the body frame displaces from the pointing frame, the momentum stored in the RWs will change its distribution, but not its norm nor the value of its components if these are expressed in an inertial frame. Due to its slow dynamics, the pointing frame can be considered inertial in a first approximation. This means that the momentum along the α-axis will remain constant unless external torques are applied. Therefore, the goal of this strategy is to generate a torque around α, such that when the attitude is restored, the momentum in the RWs will re-distribute itself again, but the one along z will be eventually removed. The solution to this problem involves coupled circular attitude and gimbal trajectories, shifted of $90\,°$ [6]. From a fixed observer point of view, both the gimbal axis and the z-axis would perform a helix while the CubeSat proceeds along its track. This strategy has been therefore called Bi-Elicoidal Thruster-Attitude (BETA) trajectory. The guidance laws can be expressed in such a way to account for the sign of h_z, impos-

ing clockwise or anticlockwise motions:

$$\phi_1 = \phi_{max} \sin(\omega t)\,\mathrm{sgn}(h_z)$$
$$\phi_2 = \phi_{max} \cos(\omega t)$$
$$\omega = 2\pi f = \frac{2\pi}{T}$$
$$\theta_1 = -\theta_{max}\cos(\omega t)\,\mathrm{sgn}(h_z)$$
$$\theta_2 = \theta_{max}\sin(\omega t)$$

The tunable parameters are the maximum attitude angle ϕ_{max}, the maximum thruster angle θ_{max} and the period of the circular motions T. For the simulations, values of $5\,^\circ$ for the two angles and $20\,\mathrm{min}$ for the period have been considered.

## 3.2. Coasting

The WOL coasting strategies exploit the Solar Radiation Pressure (SRP) to generate desaturation torques on the S/C by differentialy tilting the SAs. During normal operations, the Solar Array Drive Mechanism (SADM) is in charge of maintaining them always in face of the Sun. The overall tilt angle will be therefore the sum of two contributions, the offset angle $\Delta_\odot$ and the relative tilting angle Δ_{rel}:
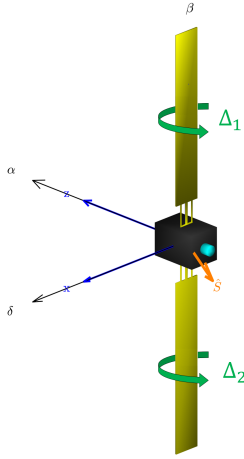
$$\Delta_1 = \Delta_\odot + \Delta_{rel_1}$$
$$\Delta_2 = \Delta_\odot + \Delta_{rel_2}$$
$$\Delta_\odot = \arctan\left(\frac{S_\delta}{S_\alpha}\right) \tag{4}$$

When an attitude motion is required, the orientation of the body with respect to the pointing frame can be linked to the attitude angles ϕ_1 and ϕ_2. However, in this case, the two angles will represent the slewing around the δ-axis and α-axis respectively:
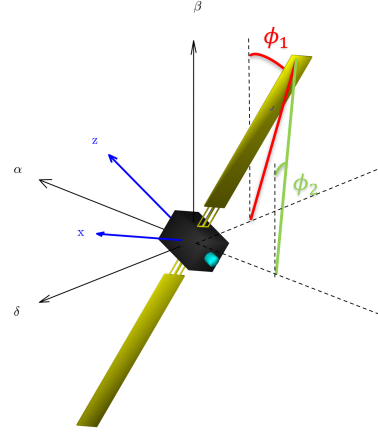
$$A_{b/p} = \begin{bmatrix} \cos\phi_2 & \sin\phi_2 & 0 \\ -\sin\phi_2 & \sqrt{1-(\sin\phi_1)^2-(\sin\phi_2)^2} & -\sin\phi_1 \\ 0 & \sin\phi_1 & \cos\phi_1 \end{bmatrix}$$

3.2.1 SSA & PW

When the attitude is fixed, it is possible to generate torques thanks to SA tilting only about axes perpendicular to β. In particular, two types of effects can be accomplished:

- For the Single Solar Array (SSA) strategy, an entire solar wing is kept in shadow such to have a net force on the other one, producing a torque T_{SSA} aligned with $\beta\times\hat{\boldsymbol{S}}$.

- For the PinWheel (PW) strategy, the two wings are tilted one with respect to the other of $70\,^\circ$, just like a pinwheel, in order to produce a torque T_{PW} aligned with $\hat{\boldsymbol{S}}$.

The required combinations of tilting angles to accomplish these torques are reported in *Table 3*. While the choice of $90\,^\circ$ in SSA is straightforward, the value of $35\,^\circ$ for PW comes from the fact that the SRP torque is the highest at that angle, as it can be seen in *Figure 4*.

Strategy	SSA_1	SSA_2	PW_1	PW_2
Δ_{rel_1}	$0\,^\circ$	$90\,^\circ$	$-35\,^\circ$	$+35\,^\circ$
Δ_{rel_2}	$90\,^\circ$	$0\,^\circ$	$+35\,^\circ$	$-35\,^\circ$
$\boldsymbol{T}$	$-\boldsymbol{T}_{SSA}$	$+\boldsymbol{T}_{SSA}$	$-\boldsymbol{T}_{PW}$	$+\boldsymbol{T}_{PW}$

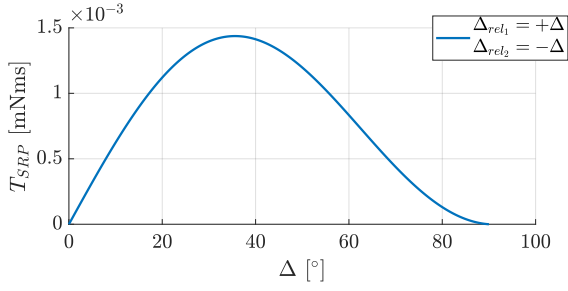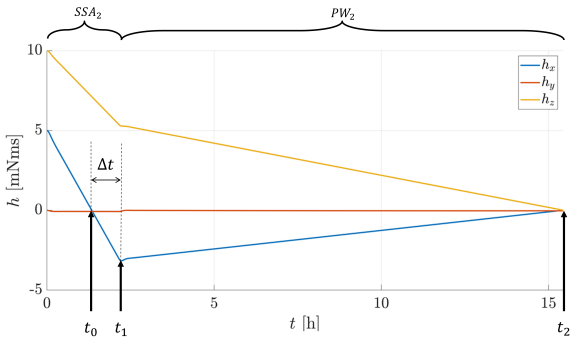Table 3: Combinations of the relative tilting angles for the SSA and PW strategies

Figure 4: SRP torque generated in PW strategy by different relative tilting angles

By selecting the correct combination, both h_x and h_z are guaranteed to approach zero in any situation but not reach it at the same time, since the slopes depend on the Sun direction. To solve this issue, a coupling of PW and SSA is employed. Intuitively, this could be a solution since the main difference between the two strategies is that in one case the momentum slopes are of the same sign, in the other case they have opposite signs. This means that after the zero crossing of either h_x or h_z, after a certain time delay Δt the configuration can be changed in such a way to have both of them reach zero at the same time. The problem is stated in *Figure 5* with an example of a SSA_2 strategy followed by a PW_2.

$$\begin{cases} T_{SSA_x} = \dfrac{h_{x_1} - h_{x_0}}{\Delta t} \\[2mm] T_{SSA_z} = \dfrac{h_{z_1} - h_{z_0}}{\Delta t} \\[2mm] T_{PW_x} = \dfrac{h_{x_2} - h_{x_1}}{t_2 - t_1} \\[2mm] T_{PW_z} = \dfrac{h_{z_2} - h_{z_1}}{t_2 - t_1} \end{cases} \quad \begin{array}{l} \text{find} \quad \Delta t \\[2mm] \text{s.t.} \quad h_{x_2} = h_{z_2} = 0 \end{array}$$

Figure 5: Coupling of SSA with PW

The time delay can be found re-arranging the equations and applying the final conditions:

$$\Delta t = \frac{h_{x_0} T_{FW_Z} - h_{z_0} T_{FW_x}}{T_{SSP_z} T_{FW_x} - T_{SSP_x} T_{FW_Z}}$$

The torques are assumed to be estimated on-board prior to the WOL maneuver. In this way, the computer just needs to record the value of the angular momentum that has not crossed zero and apply the reported formula.

3.2.2 SRPW

Also during coasting, a full WOL can not be completed employing strategies that are based only on a fixed attitude, because there is no possibility to produce torques about the y-axis.

To desaturate this axis, the property of conservation of momentum in a fixed frame can be exploited again. In particular, by coupling a specific SADM trajectory with an attitude motion, torques about the β-axis can be produced, which will eventually dump the momentum on y. The imposed attitude motion and SA trajectory are circular, but the latter is shifted of $90°$ in amplitude and of $\Delta_\odot$ in phase:

$$\phi_1 = \phi_{max} \sin(\omega t)$$
$$\phi_2 = \phi_{max} \cos(\omega t)$$

$$\Delta_{rel_1} = 90° \min\left(1, 1 + \cos\left(\omega t + \Delta_\odot\right)\right)$$
$$\Delta_{rel_2} = 90° \min\left(1, 1 - \cos\left(\omega t + \Delta_\odot\right)\right)$$

The two consequences are that the face that should point the Sun is kept close to $\Delta_{rel} = 0°$ for a reasonable fraction of time, and this time slot is consistent with the Sun direction. Moreover, every half period the amplitude of one SA is capped to $90°$ while the second one follows the nominal trajectory. In this way, the Sun provides a force only to one SA at a time and since this force is always offset from the β-axis on the same "side", a periodic torque about that axis is generated. From an external observer, the CubeSat seems to "wade" against the Solar wind, and therefore this strategy has been called Solar Radiation Pressure Wading (SRPW).

The tunable parameters are again the maximum attitude angle ϕ_{max} and the period of the circular motions T. A good compromise has been found in the simulations using $20°$ and $2\,\text{h}$.

3.3. Pyramid Configuration

Since the momentum is conserved inertially, all the WOL strategies can be still used. However,

as momentum to dump, they will consider an *equivalent* momentum, that is just the projection of the actual RWs momentum on the body axis. Therefore, the 4 RWs problem is re-written as a 3 RWs case, using the configuration matrix:

$$\boldsymbol{h}_{eq} = R\,\boldsymbol{h}_{RW}$$

When more than 3 wheels are employed, a *singularity* can occur, in the sense that for specific combinations of the components of $\boldsymbol{h}_{RW}$, the correspondent $\boldsymbol{h}_{eq}$ goes to zero:

$$\boldsymbol{h}_{eq} = \frac{1}{\sqrt{3}} \begin{bmatrix} -1 & -1 & -1 & -1 \\ 1 & -1 & 1 & -1 \\ 1 & 1 & -1 & -1 \end{bmatrix} \begin{bmatrix} 4 \\ -4 \\ -4 \\ 4 \end{bmatrix} = \begin{bmatrix} 0 \\ 0 \\ 0 \end{bmatrix}$$

For a pyramid configuration oriented along $-x$, any momentum $\boldsymbol{h}_{RW} = [k\ -k\ -k\ \ k]$ can not be off-loaded with the strategies presented so far, because the "sensed" momentum will always be zero. When such a singularity is detected, the commanded torque should be by-passed and each wheel speed should be decreased directly reducing its rotor spin rate with a proper gain:

$$\dot{\boldsymbol{h}}_{RW} = -k\,\mathrm{sgn}(\boldsymbol{h}_{RW}) \qquad (5)$$

3.4. State Machine

The final model should be able to recognize the angular momentum levels and behave accordingly, choosing the correct strategies to perform a full WOL on the entire RW assembly.

To accomplish this, it is convenient to exploit a State Machine (SM) in StateFlow, whose architecture is presented in *Figure 6*. An exhaustive explanation can be found in the thesis, but some important aspects characterize the general decision-making logic:

- The first strategy to be used, regardless of the scenario, is a fixed-attitude one. This choice allows removing firstly the momentum on "non-singular" axes. In this way, when the following strategy will start, the oscillations on the momentum components will have a mean value of zero.

- The last strategy to be used, regardless of the scenario, is a fixed-attitude one. In fact, after completing BETA or SRPW, the reset of the orientation to the pointing frame requires the RWs to store a little amount of momentum, that has to be eventually off-loaded again with fixed-attitude strategies.
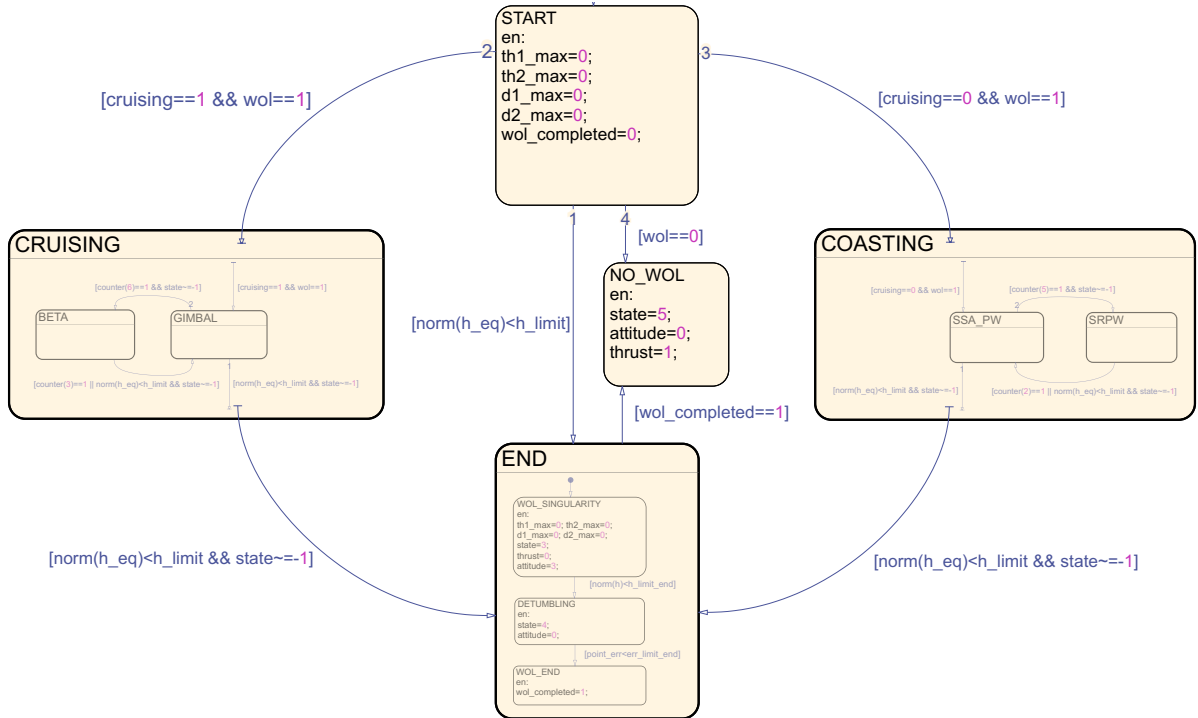

Figure 6: State Machine

- Any strategy state has two inner micro-states. The first one is a re-pointing state and the second one is related to the actual WOL strategy. Any transition to another state is prevented when the current state is re-pointing. This precaution is used to avoid fast and unexpected consecutive transitions between two states.

- The strategies that dump two momentum components at the same time use as exit condition the zero-crossing of the difference between the two components. In this way, there is the assurance that the state will be exited even if the algorithms fail the dumping because one momentum will surely cross the other, sooner or later.

4. Simulation Results

THE detailed description of the astrodynamics simulator used for the simulations can be found in the thesis main body. Even if it allows to test the WOL strategies in any type of scenario, only the results of the simulations for a 4 RWs assembly along the selected activity arc will be presented right now.

4.1. WOL in Cruising

The results of the cruising simulation are reported in *Figure 7*. The momentum is almost completely dumped: after the de-tumbling and final re-pointing the value of the norm is $h = 0.27\,\mathrm{mNms}$, the 0.91% of the initial value. The WOL is accomplished in $t = 3.15\,\mathrm{h}$.

The actual momentum stored in the wheel follow a different trend than the equivalent one. However, in both cases the norm decreases, confirming the fact that the 4 RWs case can be solved as a 3 RWs one. The procedure begins with a Gimbal strategy to remove the momentum on x and y. Then, as soon as h_x crosses h_y, the BETA trajectory is initiated. As it can be seen in the third plot, the torque generated by the thruster, expressed in the pointing frame, has a non-null component around α-axis, and this is why the momentum accumulated on that quasi-inertial direction can be off-loaded. The torques generated about the other two axes have a much larger magnitude, but their periodic nature does not
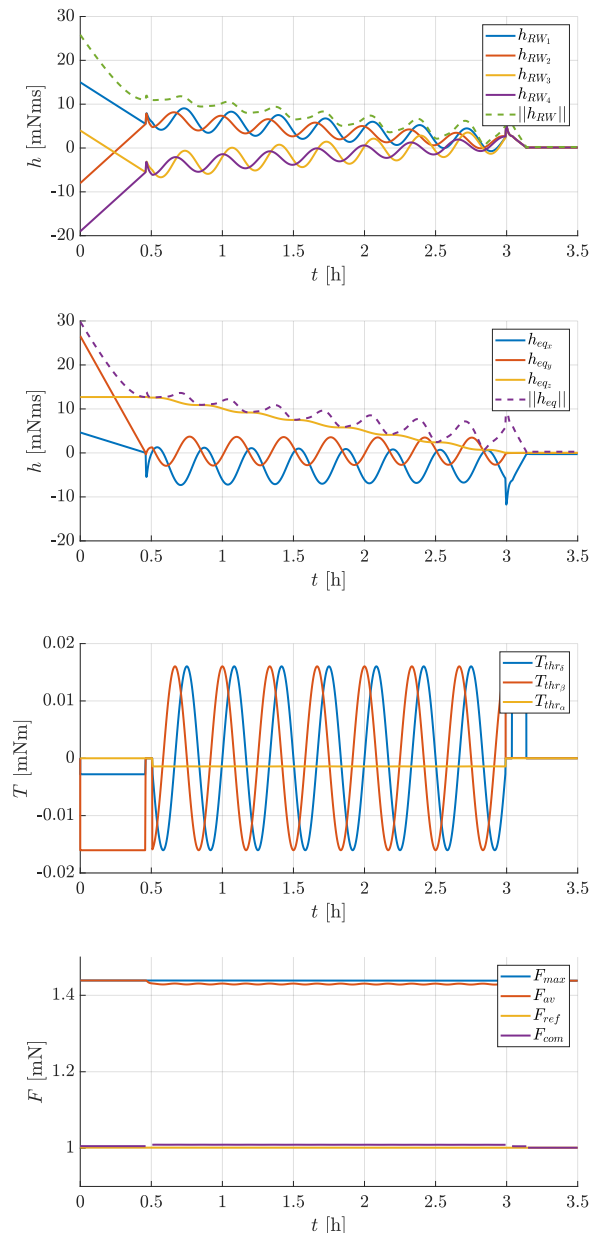

Figure 7: Angular momentum, thruster torque in pointing frame and thrust amplitude during WOL in a cruising arc

cause any momentum accumulation on β and δ. However, since h_z crosses zero before the trajectory ends its harmonic period, a final additional Gimbal strategy is required to dump the remaining momentum.

An interesting aspect is the over-thrust required to accomplish such torques. F_{com} is only 0.4% higher than F_{ref} during the first gimbal strategy and only 0.7% during BETA. These low values of over-thrust, together with the very high specific impulse of the thruster, allow saving a

relatively high amount of propellant, when compared to the case where the RCS is used to obtain the same torques. In particular, the additional consumption with respect to the case without WOL is respectively $\Delta m_p \approx 0.002\,\text{g}$ and $\Delta m_{p_{RCS}} \approx 2\,\text{g}$, resulting in mass savings of more than 99% when employing the new techniques.

4.2. WOL in Coasting

The coasting strategies require a much longer time than the cruising ones due to the lightness of the SRP disturbances. The simulation results for a coasting scenario are depicted in *Figure 8*. In this case the remaining momentum percentage is about 1.33%, completing the WOL in more or less $t = 12\,\text{h}$.

The procedure begins with a SSA strategy, followed by a PW after about 5 h, to remove the momentum on x and z. Then, as soon as h_x crosses h_z, the SRPW trajectory is initiated. As it can be seen in the plot, the torque generated by the SAs, expressed in the pointing frame, has oscillatory components on all the axes. However, the component on the β-axis is shifted in magnitude and this results in a net torque effect during the trajectory. The other two components are larger, but they are centered on zero and therefore no momentum is accumulated on δ and α.

It can be clearly noticed the occurrence, at about $t = 11.5$, of the WOL singularity. The equivalent momentum $||\boldsymbol{h}_{eq}||$ has practically reached the zero value, but the actual momentum $||\boldsymbol{h}_{RW}||$ is still high, about 14 mNms. The spin rate is then forcefully decreased bypassing the commanded torque. This action has the effect to dump the actual momentum stored on the wheel and not produce at the same time an attitude drift because the equivalent torque produced by the wheels is zero.

The main drawback of using such strategies is the decrease in power production. As it can be seen in the last plot, during SSA the power is halved, during PW is around the 80% and in SRPW it oscillates between 0% and 50%. Only during the re-pointing phases, the tilting angles are set to zero and the power produced is equal to the nominal. By carrying out a real-time integration of the power during the simulation, the energy produced is computed to be the 64.5% with respect to the case where no WOL is per-
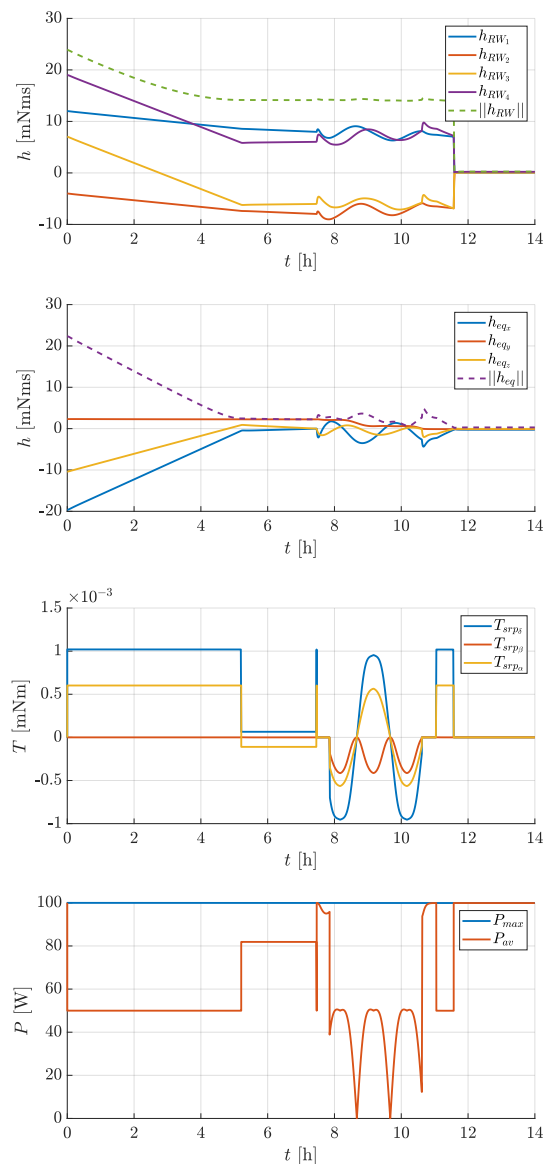

Figure 8: Angular momentum, thruster torque in pointing frame and thrust amplitude during WOL in a coasting arc

formed along the same track. This is the price to pay to use these strategies, which are, on the other hand, free of propellant consumption.

4.3. Validation

The simulations have been validated through the use of CUBesat ORbit and GNC tool (CUBORG), an ephemerides-based Guidance Navigation and Control (GNC) simulator developed in Politecnico di Milano by the Deep-space Astrodynamics Research & Technology (DART) group [7]. Due to its flexibility in terms of modifications and simplicity of use, it was possible to also con-

sider the sensors noises in further simulations to confirm the feasibility of the strategies also in a non-ideal case.

The ultimate objective of the WOL during cruising is to not affect the mission trajectory. During the re-pointing and de-tumbling phases the thruster is switched off and therefore is not following the reference thrust level. When the WOL is being carried out, on the other hand, it is switched on but is never aligned to the reference pointing vector $\hat{\boldsymbol{\alpha}}$. The trajectory comparison of a typical $3\,\mathrm{h}$ WOL with respect to the case without WOL revealed negligible differences at the end of the propagation, of about $\approx 100\,\mathrm{m}$, that in terms of relative error is on the order of $\approx 10^{-7}$. Therefore, the WOL can be performed without any significant risk of deviating from the nominal trajectory.

4.4. Sensitivity Analysis

The two main uncertainties to face are the initial angular momentum when the WOL is initiated and the displacement of the COM from the geometric center.

4.4.1 Initial Momentum

The sensitivity analysis has been performed for a total of $n = 500$ samples, considering as norm constraint the value of $||\boldsymbol{h}_0|| = 25\,\mathrm{mNms}$ and for saturation limit the usual value of $h_{max} = 19\,\mathrm{mNms}$. The Empiric Cumulative Distribution Functions (ECDFs) generated from the results are reported in *Figure 9*. In 80% of the cases the WOL is completed in less than $4\,\mathrm{h}$ and leaves as residual momentum a norm lower than $0.3\,\mathrm{mNms}$.
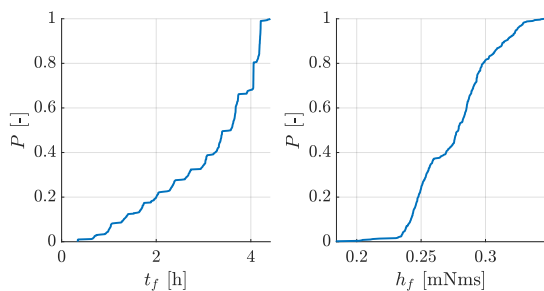

Figure 9: ECDFs of the total WOL time and norm of the final momentum with uncertainties on the initial momentum

4.4.2 COM Displacement

The algorithms can be corrected to account for the COM displacement $\boldsymbol{d}_{\oplus} = [x_{\oplus}\, y_{\oplus}\, z_{\oplus}]$. The relation in (2) can be re-written with proper approximations into (6).

$$\frac{h_y}{h_x} \approx \frac{T_y}{T_x} = \frac{-x_{\oplus} + \left(z_{\oplus} - \frac{c}{2}\right)\sin\theta_1}{y_{\oplus} - \left(z_{\oplus} - \frac{c}{2}\right)\sin\theta_2} \qquad (6)$$

Regarding the BETA strategy, the problem can be solved by shifting the gimbal angles trajectory of specific offset angles in such a way to bring the gimbal vector $\hat{\boldsymbol{g}}$ nominally aligned with the vector linking the COM with the thruster position. The offset angles to add to (3) are then given by (7).

$$\begin{aligned}\Delta\theta_1 &= \arctan\left(\frac{x_{\oplus}}{z_{\oplus} + \frac{c}{2}}\right) \\ \Delta\theta_2 &= \arctan\left(\frac{y_{\oplus}}{z_{\oplus} + \frac{c}{2}}\right)\end{aligned} \qquad (7)$$

If the COM displacement is assumed to be known with a certain degree of accuracy, it is therefore possible to apply the corrected WOL strategies without consequences.

The sensitivity analysis has been performed with the corrected algorithms considering a norm of the displacement vector of $1.2\,\mathrm{cm}$ and again 500 samples. In only 4 cases the WOL takes more than $10\,\mathrm{h}$, which means a percentage of success of 99.2%. For the successful cases the mean final angular momentum is around $0.26\,\mathrm{mNms}$ with a total WOL duration of about $3.5\,\mathrm{h}$. The values are close to the results of the previous analysis, therefore the corrections made to the algorithms to account for the COM shift can be considered correct and validated.

5. Conclusions

THE simulations demonstrated the validity of the new techniques in performing the WOL under different deep-space scenarios and initial conditions, in full autonomy. When coming to uncertainties, the algorithms are robust and can still accomplish the goal with mild differences, that in any case do not affect the mission operations nor the trajectory.

5.1. Lessons Learned

All the presented strategies require the use either of a gimbal mechanism or a SADM. The potentially higher cost that these devices could lead to

is balanced by the fact that the architecture no more needs dedicated momentum-management actuators, such as RCS and Magnetotorquers. This is beneficial from the design viewpoint both in terms of mass and volume savings. The additional propellant that the main thruster should provide for the WOL is a very small percentage of the theoretical one that the RCS requires, due to the former's typical higher specific impulse. In the case of coasting strategies, the mass is completely saved, in exchange for a reduced power production capability.

These advantages, coupled with the possibility to completely automate these techniques, are huge advantages when looking at future deep-space CubeSats missions based on miniaturized architectures. It seems that the space industry is becoming more and more biased in favor of this paradigm, and the WOL techniques presented can be considered a promising and effective way to expand both the capabilities and the lifetime of such satellites.

In particular, a possible way to estimate the overall impact of the WOL strategies on M-Argo mission could be to consider the *swirl torque*, a disturbance typical of ion engines that produces a parasitic torque around the thruster axis. From preliminary analyses, it can be shown that the expected additional consumption of propellant to account for this torque can be reduced from $\approx 400\,\mathrm{g}$ to $\approx 1\,\mathrm{g}$, employing the BETA strategy instead of de-saturating with the RCS. This results in a mass savings of over 99%.

5.2.   Future Works

The coasting and the cruising strategies have been presented and simulated in a complete decoupled way, but one could think of using them at the same time to have a faster or in some cases more efficient de-saturation. The most straightforward example is given by a Gimbal strategy coupled with SSA. The two strategies can be super-imposed to de-saturate at the same time all of the three axes, the x and y with the thruster and the z with the SA tilting. An exploration of the possible combined strategies could be carried out, with special regards to the power availability, that inevitably has to degrade.

Moreover, the SSA and PW strategies could be merged into a single strategy, where an optimal value for the tilting angles should be sought

through a minimization process, in order to de-saturate two axes and ending with zero momentum at the same time. This procedure would require an even more accurate model of SRP to be used for onboard estimation, and maybe also the possibility to change the optical properties of the SP in real-time.

At last but not least, the most interesting and challenging future work would be represented by the actual testing of these strategies, first with a hardware-in-the-loop integration, and then on an actual in-orbit demonstration. The candidate that should be considered as the straightforward choice is M-Argo, but eventually the strategies could also be tested on other CubeSat platforms such as the ones mentioned in the introduction. Eventually, the concepts could be applied to any future mission, integrating the S/C architecture with the required components, but on the other hand ending with a design that is free of dedicated momentum-management actuators and potentially more compact and efficient.

References

[1] Benjamin K Malphrus, Anthony Freeman, Robert Staehle, Andrew T Klesh, and Roger Walker. Interplanetary cubesat missions. In *Cubesat Handbook*, pages 85–121. Elsevier, 2021.

[2] V Franzese, F Topputo, F Ankersen, and R Walker. Deep-space optical navigation for m-argo mission. *The Journal of the Astronautical Sciences*, pages 1–22, 2021.

[3] ESA. 5th esa cubesat industry days.

[4] GomSpace. Nanopower msp. URL https://gomspace.com/shop/subsystems/power/msp-solar-panels.aspx.

[5] Meike List, Stefanie Bremer, Benny Rievers, and Hanns Selig. Modelling of solar radiation pressure effects: Parameter analysis for the microscope mission. *International Journal of Aerospace Engineering*, 2015, 2015.

[6] Thomas Randolph, Timothy McElrath, Steven Collins, and David Oh. Three-axis electric propulsion attitude control system with a dual-axis gimbaled thruster. In *47th AIAA/ASME/SAE/ASEE Joint Propulsion Conference & Exhibit*, page 5586, 2011.

[7] DART Group. *A CUBesat ORbit and GNC tool*. Politecnico di Milano, 2021.

School of Industrial and Information Engineering
Department of Aerospace Science and Technology

Master of Science in Space Engineering

POLITECNICO
MILANO 1863

Autonomous Wheel Off-Loading Strategies for Deep-Space Cubesats

Supervisor:
Francesco Topputo

Co-supervisor:
Antonio Rizza

Author:
Andrea Pizzetti
944547

A.Y. 2020/2021

Acknowledgements

I would first like to thanks my advisor Francesco Topputo and my co-advisor Antonio Rizza for their support throughout these months. Even if due to the current pandemic situation we could not manage to have frequent in presence meetings, the communications have always been smooth and pleasant and I really enjoyed these months of work on such a challenging subject. Before starting, I was already a bit interested in this field, but this thesis made me realize that this is the subject I want to work on in the near future.

I also want to express my gratitude to all the people that have been of constant support in these years: my old friends of Treì, and the new ones I met during my university studies in Milan. Time is something that an engineering student is not always given in abundance; Nevertheless, these years have been full of experiences that have strengthened our ties and that I will certainly take with me in the coming years.

At last but not least, I feel compelled to profoundly thank my family for all they have taught me and for having shaped me into the person that I am today. I am not exaggerating when I say that without you, I could hardly have completed my studies with the same peace of mind and at the same time have time to devote to friends, sports and hobbies. When I've been in need, you've always been there, and that's the thing I appreciate the most in people.

Abstract

In the last years, several deep-space CubeSats missions were announced, since such platforms enable possibilities of exploration and scientific return with relatively low-budget and short development times. However, they require careful trade-offs on design drivers such as mass, volume, and cost, while ensuring the possibility to perform autonomous operations. This work addresses the problem of saturation of the reaction wheels, proving the achievement of de-saturation, also known as wheel off-loading, without the need of using dedicated momentum-management actuators. The presented techniques show how it is possible to produce torques along at least two body axes by offsetting the main thruster or tilting differentially the solar arrays. The dumping on the third axis can be still accomplished by coupling a specific attitude trajectory with the motion of either the gimbal mechanism or the solar array drive mechanism. The M-Argo CubeSat is selected as a case study and an astrodynamics simulator is developed to test the techniques along its deep-space trajectory. The off-loading during the cruising arcs employs the gimballed thruster and dumps momentum to a residual value lower than $0.3\,\mathrm{mNms}$ in typically $3\,\mathrm{h}$, granting a mass savings of more than 99% with respect to the usage of a reaction control system. During the coasting arcs, the solar arrays are tilted and several hours are required, depending on the Sun direction and intensity, but the propellant is completely saved. The autonomous decision-making for the different strategies is carried out with a state machine, which allows the accomplishment of the desaturation in any scenario. The simulator is validated and the trajectory is shown to have negligible differences with respect to the nominal one, since the thrust is corrected in such a way to account for the offset of the thruster and still provide the reference value along the original pointing vector. Finally, sensitivity analyses are carried out on the initial angular momentum components and the center of mass displacement to check the robustness of the algorithms.

Keywords: M-Argo; Reaction Wheel; Off-Loading; Desaturation; Deep Space CubeSat; Autonomy

Sommario

Negli ultimi anni sono state annunciate diverse missioni di CubeSat in spazio profondo, in quanto consentono ampie possibilità di esplorazione e ritorno scientifico con un budget relativamente basso e tempi di sviluppo brevi. Ciò nonostante, il design di queste piattaforme richiede compromessi su diverse figure di merito, quali massa, volume e costo, e allo stesso tempo deve garantire la possibilità di eseguire operazioni in autonomia. Questa tesi affronta il problema della saturazione delle ruote di reazione, dimostrando la possibilità di effettuare la desaturazione senza la necessità di equipaggiare il satellite con degli attuatori dedicati alla gestione di questa problematica. Le tecniche presentate mostrano come sia possibile produrre momenti attno ad almeno due assi del satellite, disallineando il propulsore principale o ruotando in modo differenziale i pannelli solari. La rimozione del momento accumulato sul terzo asse può essere comunque realizzata, accoppiando una specifica traiettoria di assetto con una relativa al meccanismo di puntamento del propulsore o alla rotazione dei pannelli. Come caso di prova, la missione M-Argo è stata scelta ed un simulatore astrodinamico è stato sviluppato ad hoc per testare le tecniche durante la traiettoria del CubeSat. Le manovre effettuate durante gli archi di crociera sfruttano il meccanismo di puntamento del propulsore e permettono di ridurre il momento angolare ad un valore residuo inferiore a 0.3 mNms in tipicamente 3 ore, garantendo un risparmio di massa di oltre 99% rispetto all'uso dei razzetti di controllo a reazione. Durante gli archi di coasting, invece, i pannelli solari vengono ruotati e la manovra richiede diverse ore, a seconda della direzione e dell'intensità della radiazione solare, ma il propellente non viene consumato affatto. Il processo di scelta tra le diverse strategie è autonomo e realizzato con una macchina a stati, che permette di ottenere la desaturazione in un qualsiasi scenario. Il simulatore è stato validato ed è stato dimostrato che la traiettoria ha differenze trascurabili rispetto a quella nominale, poiché la spinta viene corretta in modo tale da tenere conto del disallineamento del propulsore e da fornire il valore di riferimento lungo il vettore di puntamento originale. Infine vengono effettuate analisi di sensitività sul valore iniziale di momento angolare e sullo spostamento del centro di massa, per verificare la robustezza degli algoritmi.

Parole Chiave: M-Argo; Ruote di Reazione; Off-Loading; Desaturazione; CubeSat in Spazio Profondo; Autonomia

Contents

Acronyms

AOCS	Attitude and Orbit Control System.
ARW	Angle Random Walk.
ASPECT	Asteroid SPECTral imager.
AU	Astronomic Unit.
BETA	Bi-Elicoidal Thruster-Attitude.
CDF	Concurrent Design Facility.
CDS	CubeSat Design Specification.
CMG	Control Moment Gyro.
COM	Center Of Mass.
COTS	Components Off The Shelf.
CP	Center of Pressure.
CUBORG	CUBesat ORbit and GNC tool.
DART	Deep-space Astrodynamics Research & Technology.
DCM	Direction Cosines Matrix.
DOF	Degree Of Freedom.
ECDF	Empiric Cumulative Distribution Function.
EOM	Equation Of Motion.
ESA	European Space Agency.
FOV	Field Of View.
FSS	Fine Sun Sensor.
GG	Gravity Gradient.
GNC	Guidance Navigation and Control.
HK	House-Keeping.
IC	Initial Condition.

IMU	Inertial Measurement Unit.
ISS	International Space Station.
LEO	Low Earth Orbits.
LQR	Linear Quadratic Regulator.
MEMS	Micro Electro-Mechanical Systems.
NAIF	Navigation and Ancillary Information Facility.
NEA	Near-Earth Asteroid.
NLP	Non-Linear Programming.
OBC	On-Board Computer.
OBDH	On-Board Data Handling.
PPU	Power Processing Unit.
PW	PinWheel.
RCS	Reaction Control System.
RW	Reaction Wheel.
S/C	Spacecraft.
SA	Solar Array.
SAA	Sun Aspect Angle.
SADM	Solar Array Drive Mechanism.
SLS	Space Launch System.
SM	State Machine.
SP	Solar Panel.
SRP	Solar Radiation Pressure.
SRPW	Solar Radiation Pressure Wading.
SSA	Single Solar Array.
STR	Star Tracker.
TOF	Time of Flight.
TRL	Technology Readiness Level.
U	Unit.
WOL	Wheel Off-Loading.
ZPM	Zero Propellant Maneuver.

1 Introduction

1.1 Context

A CubeSat is a miniaturized Spacecraft (s/c) designed in a modular way. The basic element is called Unit (u) and it's a cube of 10 cm size. There are different form factor that can be used, starting from 1u, 2u, 3u till 12u and more recently 24u. The standardization started almost two decades ago from an initiative of the California Polytechnic State University and we are now arrived at the 14th revision of the CubeSat Design Specification (cds). CubeSat projects are usually completed after less than 2 years because this standardization allows much easier and faster development and integration phases [1].

From the first launch in 2003, this kind of platform experienced exponential success over the years, as it can be seen in *Figure 1.1*.

These numbers are explained by the fact that these projects have a much lower budget than the usual, and are therefore accessible to a larger share of possible developers, such as universities. Not only the CubeSats are characterized by cheaper Components Off The Shelf (cots), but also the launch cost is decreased because they are usually released as complementary payloads, in the so-called *piggyback* launches.

For these reasons, in the last years, the space sector has been characterized by a strong push in the nano-satellite class development enabling possibilities that before could only be dreamed. When they were first designed, CubeSats were addressed to Earth-observation missions in Low Earth Orbits (leo), mainly for educational purposes, but in recent years it has been proven that they can be used also for interplanetary missions, with a high scientific return.
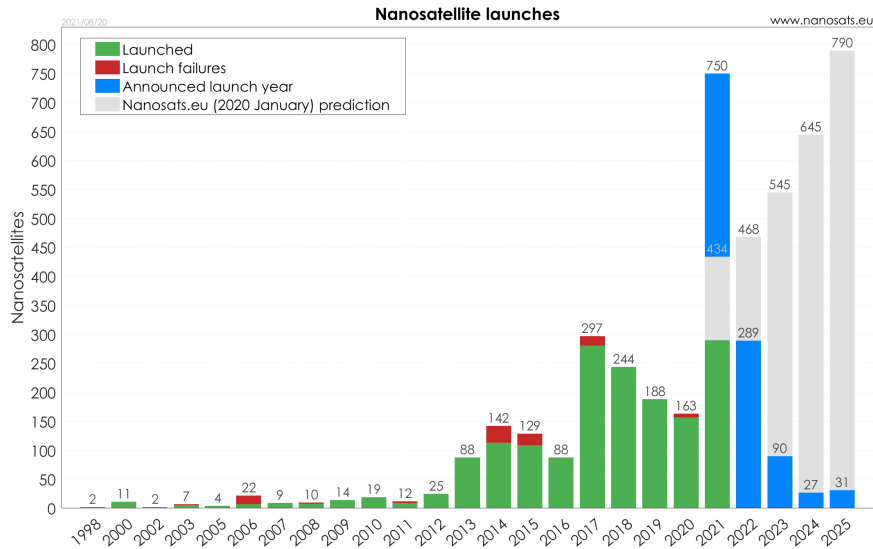
Figure 1.1: Past and projected numbers of CubeSats launches. Courtesy of Nanosats Database [2]

The most important milestone in deep-space CubeSat exploration was reached in May of 2018 in the context of the Mars Cube One mission, when the twin MarCO CubeSats succeeded in performing the first interplanetary travel. The mission objective of MarCO-A and MarCO-B was to provide a real-time communications-relay for Insight's entry, descent and landing at Mars. The 6u satellites accomplished a flyby around the red planet after about half year of autonomous cruising from the LEO orbit on which they were released [3]. A rendering of one of the CubeSat twins is depicted in *Figure 1.2*.
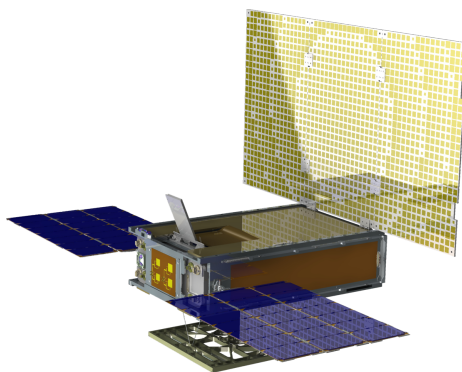
Figure 1.2: MarCO, first deep-space CubeSat. Courtesy of Klesh [3]

That success gave the input and the optimism required to start the design of CubeSats missions with the aim of reaching outer planets and asteroids. Several CubeSat missions outside LEO were indeed announced in the past years and the most promising have been

reported in the following bullet points:

- **NEA Scout (NASA)**. This mission will demonstrate the capability of a 6U CubeSat to perform imaging and characterization of a Near-Earth Asteroid (NEA) after reaching it using a low-thrust solar sail propulsion system. The NEA Scout, pictured in *Figure 1.3*, will be released on an Earth escape trajectory on the first flight of the Space Launch System (SLS), at the end of 2021. After a Lunar fly-by, the CubeSat will deploy the solar sail and begin its journey towards the asteroid [4].
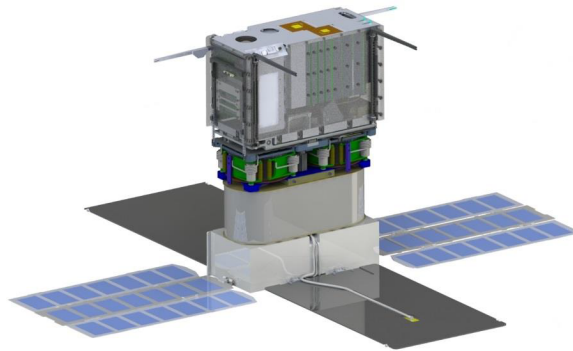
Figure 1.3: NEA Scout, deep-space CubeSat propelled by a solar sail. Courtesy of Stiltner [4]

- **Lunar IceCube (NASA)**. This 6U CubeSat, depicted in *Figure 1.4*, will also exploit the first flight of SLS, being injected into a direct lunar transfer. The transfer trajectory will be carried out with an innovative ion engine to attain a specific lunar science orbit. The mission will locate and measure volumes and composition of water ice deposits and other volatiles on the Moon [5].
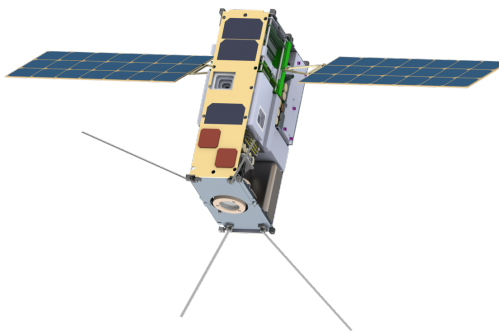

Figure 1.4: Lunar IceCube, mapping of ice deposits on Moon surface. Courtesy of Nanosats Database [6]

- **LUMIO (ESA)**. The Lunar Meteoroid Impact Observer will observe, quantify and characterize asteroid impacts on the lunar far-side by detecting the flashes generated

on the surface. The 12U CubeSat is scheduled to be released in an Earth-Moon L2 orbit in 2023 [7].

- **VMMO (ESA)**. The Volatile and Mineralogy Mapping Orbiter is a 12U CubeSat that will perform characterization of relevant in-situ usable resources on the Moon surface. A potential launch window could be between 2022 and 2023, as a hosted payload of the Lunar Communications Pathfinder Mission [8].

- **Juventas & Milani (ESA)**. In the context of the Hera mission, these two 6U CubeSats will be released from the mothership in the proximity of the Didymos binary system to respectively perform a global mapping of the two asteroids and a characterization of the internal structure of the secondary body. The launch is foreseen for late 2024 [9, 10].

- **M-Argo (ESA)**. The Miniaturised Asteroid Remote Geophysical Observer (M-Argo) is a 12U CubeSat aiming to rendezvous with a NEA after an autonomous deep-space travel using as propulsion system an innovative ion engine. It will be released in a parking orbit around the Sun-Earth L2 point between 2023 and 2024 [11].

1.2 Motivations

All of the previous missions use Reaction Wheels (RWs) to reject the attitude disturbances and control the orientation of the satellite. It becomes therefore a problem of primary importance the management of this kind of device, in particular regarding the problem of *saturation*, that once it is reached, causes the actuator to not work properly.

The scope of this dissertation is to simulate the feasibility of new techniques for the de-saturation of RW, also known as Wheel Off-Loading (WOL), in full autonomy. Such methodologies will not employ the use of any dedicated system that is usually carried on-board to manage the angular momentum accumulated by the wheels, like Reaction Control System (RCS) or Magnetotorquers. Instead, they will exploit components of the S/C that are devoted to other duties: the propulsion system, if coupled with a pointing mechanism, and the Solar Arrays (SAS), if they can be differently tilted by a Solar Array Drive Mechanism (SADM).

If proven, these concepts could lead to many advantages, such as the mass and volume savings due to the absence of the aforementioned momentum-management devices. On the other hand, if these last are present and they encounter a failure, the same strategies could be used for redundancy, allowing to regain control of the satellite and therefore increasing its lifetime. This is valid for either currently active or planned missions.

Another important aspect to consider is that RCS and Magnetotorquers require respectively the presence of additional propellant and magnetic field to properly work. These are not resources easily available in deep-space missions, where the satellite has heavy constraints in terms of mass and spends most of its lifetime in heliocentric orbits far from the magnetic influence of the planets. Instead, using the same thruster that is used for the orbital cruising also for de-saturation allows to keep on-board only the main propellant tank and save mass thanks to the inherent higher efficiency of thrusters with respect to RCS. Furthermore, strategies based on Solar Panel (SP) require solar illumination, typically always achieved in deep-space missions.

The strategies will be therefore demonstrated using a deep-space mission as a test-case scenario. The choice has fallen on M-Argo, which is characterized by an assembly of 4 RWs, a gimballed gridded ion thruster, and two large SAs. It is therefore the perfect candidate to prove these techniques. Moreover, since the CubeSat platforms are very good technology demonstrators and they experienced exponential success in the last years, it is natural to consider this class of satellites, in view of a future in-orbit demonstration.

Two different families of WOL strategies have been developed, depending on the scenario when they can be used:

- **Cruising Arc**. During the interplanetary trajectory cruising arcs, the thruster is active and produces a reference force along a pre-defined pointing vector. By making use of a gimbal mechanism and offsetting the thrust vector, it could be possible to generate de-saturation torques in specific directions. In this case, the challenge is to not affect the reference trajectory with spurious forces, while still having the same level of thrust along the pointing vector.

- **Coasting Arc**. During the coasting arcs, the power drawn from the thruster is not present, and therefore there is no need to have both SAs facing the Sun continuously. By rotating them in a differential way, it could be possible to produce torques due to Solar Radiation Pressure (SRP) differences between the two.

An astrodynamics model in Simulink will be developed to test the strategies in real-time simulations. Starting from any values of stored angular momentum, a State Machine (SM) will manage the transitions from one strategy to the other in order to end up with a fully de-saturated situation in complete autonomy.

The simulation results will be validated through the use of a CUBesat ORbit and GNC tool (CUBORG) developed in Politecnico di Milano [12]. This is a high-fidelity ephemeris-based 6 Degree Of Freedom (DOF) simulator with an architecture made in such a way to have future hardware-in-the-loop integrations. The trajectory output of the WOL simulation will be compared with the case without WOL to show that these maneuvers have a mild effect on the orbital propagation.

1.3 State of the Art

An overview of the current State-of-the-Art on the actuators that are present on M-Argo, as well as on the wol techniques currently used, is now presented.

1.3.1 Miniaturized Reaction Wheels

The rw is a momentum-exchange device widely used in attitude control, composed of a wheel and an electric motor that controls its spinning. As the name suggests, its working principle is based on the reaction torque that the satellite experiences when the wheel increase or decrease its speed. The concept is shown in *Figure 1.5*. This kind of device is highly reactive and can be very precise; however, when the angular rate reaches its maximum velocity, the wheel is said to be *saturated* and the angular momentum must be unloaded from it by external means, otherwise the wheel can no more produce torques. Moreover, the electric motor takes a maximum level of input power and therefore also the maximum torque that can be provided by the wheel is capped.
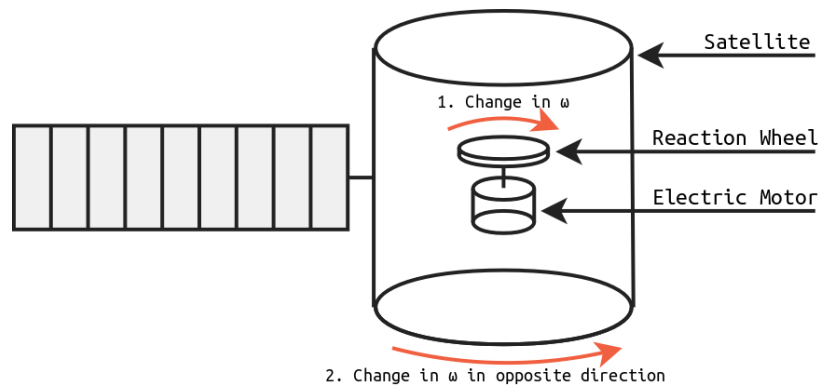
Figure 1.5: Working principle of a reaction wheel. Courtesy of Grassin [13]

By placing 3 wheels in a orthogonal configuration, it's possible to generate torques about all three directions and fully control the attitude of the body. For redundancy reasons, it is common to place an additional wheel and have a rws assembly in a pyramid configuration. In this case, the angular momentum stored in the 4 wheels can be projected into the three axes by using the configuration matrix R in (1.1), whose columns are the direction of the wheels spin axes expressed in the body axes.

$$\boldsymbol{h}_{eq} = R\,\boldsymbol{h}_{RW} \tag{1.1}$$

An example of a rws assembly in a pyramid configuration is depicted in *Figure 1.6*. In this case, the assembly is directed along z-axis with an angle of $45°$. However, different

configurations can be employed, according to the needs. In general, angled or *skewed* configurations are preferred because even if they reduce the control authority on any single axis, they add redundancies in case of failure of one of the RWs. It is even possible to compute the optimal number and directions of the wheels, according to a prediction of the external torques, to have the lowest power consumption [14, 15].
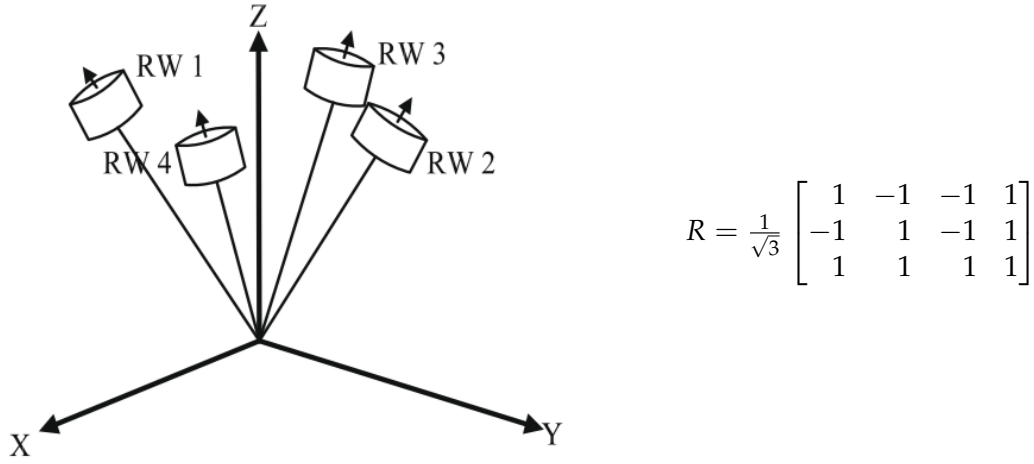

$$R = \frac{1}{\sqrt{3}} \begin{bmatrix} 1 & -1 & -1 & 1 \\ -1 & 1 & -1 & 1 \\ 1 & 1 & 1 & 1 \end{bmatrix}$$

Figure 1.6: Configuration matrix of a pyramid RWs assembly along z along z. Courtesy of Ismail [15]

The configuration matrix for more than 3 RWs is rectangular and its inverse $R^\star$ is given by the pseudo-inverse or Moon-Penrose inverse formula in (1.2).

$$R^\star = R^T \left(R R^T \right)^{-1} \tag{1.2}$$

The dynamics of the actuator takes as input a commanded torque $\boldsymbol{T}_{com}$ and outputs an effective torque $\boldsymbol{T}_{eff}$ that in general can be different because both the angular momentum and the torque are limited by bounds due to saturation and technological restrictions respectively. Moreover, if the satellite has a non-null angular rate $\boldsymbol{\omega}$, the gyroscopic coupling has to be considered. The full dynamics is reported in (1.3), where the bar means that the quantities have been capped [7].

$$\begin{aligned} \dot{\boldsymbol{h}}_{RW} &= -R^\star (\boldsymbol{T}_{com} + \boldsymbol{\omega} \times R \boldsymbol{h}_{RW}) \\ h_{min} &< \boldsymbol{h}_{RW} < h_{max} \\ T_{min} &< \dot{\boldsymbol{h}}_{RW} < T_{max} \\ \boldsymbol{T}_{eff} &= -R \bar{\dot{\boldsymbol{h}}}_{RW} - \boldsymbol{\omega} \times R \bar{\boldsymbol{h}}_{RW} \end{aligned} \tag{1.3}$$

When it comes to miniaturization, the torque capabilities are strongly reduced because of the small inertia of the wheels. Even if the spin rate is high, the angular momentum that derives from it remains low. Another issue is caused by the friction of the bearings, which can cause non-linearities in the response. In particular, a dead zone operation will

be present around the zero-speed value due to static friction [16]. This is a problem that should be addressed when the wheel frequently reverses its rotation sense.

There are several commercial products in the market and mostly have flight heritage. Their specifics from different manufacturers are reported in *Table 1.1*.

	m [kg]	T_{max} [mNm]	h_{max} [mNms]
Adcole Space — MAI-400	0.110	1	11
Blue Canyon Technologies — RWP015	0.130	4	15
GomSpace — GSW600	0.180	2	19
NanoAvionics — RW0	0.137	3	20
Sinclair Interplanetary — RW-0.01	0.120	1	18

Table 1.1: Miniaturized RW commercial solutions

1.3.2 Gridded Ion Engines

The ion propulsion working principle is based on the ionization of a gaseous propellant and its acceleration in form of plasma by means of electrostatic grids charged at different potentials. Once exhausted, a neutralizer is used to compensate for the positive charge of the plume to avoid its drifting and bouncing back to the s/c.

There are two distinct families of ion thrusters:

- **Direct Current Discharge**: the ionization is carried out by means of electron impact. An electrode cathode is required and therefore only noble gases such as Xenon can be employed to avoid their interaction with the electrode.

- **Radio Frequency Discharge**: the ionization is carried out by means of an oscillating electromagnetic field. A radio-frequency generator provides current to an induction coil wrapped around the ionizer vessel. The generated axial magnetic field induces a circular electrical eddy field that enables the ionization of the propellant. Since this process is cathode-less, besides Xenon also inert and reactive gases can be used.

A comparison between the two solutions is depicted in *Figure 1.7*.

When coming to miniaturization, there are few commercial solutions with flight heritage. The main issues are due to the complexity to miniaturize the Power Processing Unit (PPU), which must provide not only a certain amount of power but also very high voltages in order to effectively accelerate ions. The typical thrust values are between 0.1 mN and
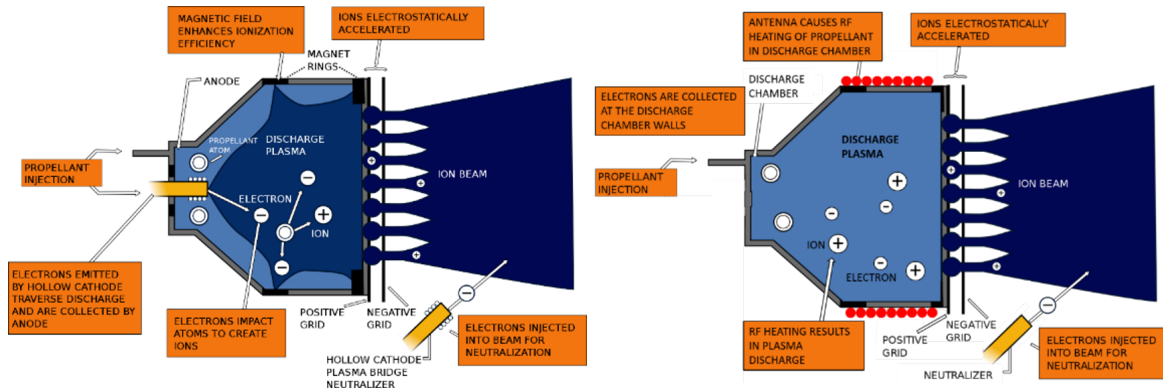
Figure 1.7: Comparison between DCD-based and RFD-based ion propulsion systems. Courtesy of NASA [16]

15 mN, while the specific impulse can reach up to 3500 s [16]. Data on thrust and specific impulse about the commercial solutions developed or under development are collected in *Table 1.2*, in order of descending Technology Readiness Level (TRL) [17–23]. The TRL is a method used to estimate the maturity of a technology with a scale from 1 to 9, being 9 a fully proven and tested device.

	F [mN]	I_{sp} [s]	Propellant	Status
Enpulsion — NANO	0.01/0.4	2000/6000	Indium	Orbit test in 2018
ThrustMe — NPT-30	0.3/1.1	2400	Iodine	Orbit test in 2020
Busek — BIT-3	1.25	2300	Iodine	Orbit test in 2021
UT/JAXA — I-COUPS	0.3	1000	Xenon	TRL 8 in 2015
Airbus — RIT-μX	0.4/3	300/3000	Xenon	TRL 5 in 2015
JPL/UCLA — MIXI	0.1/1.5	3000	Xenon	TRL 4 in 2017

Table 1.2: Miniaturized gridded ion engines developed or under development

An important aspect to consider in a mission that employs this kind of propulsion is the generation of a parasitic torque along the thruster axis. This so-called *swirl torque* is thought to be caused by misalignments in the grids or leakage of the magnetic field lines that swerves the trajectory of the ions [16, 24, 25]. A visual representation of such phenomena is shown in *Figure 1.8*.

The order of magnitude of this disturbance torque scales with the thrust level of the engine, as it can be seen from the data collected in *Table 1.3* and the empiric trend depicted in *Figure 1.9*, referred to the three ion thrusters of Dawn [25–27].
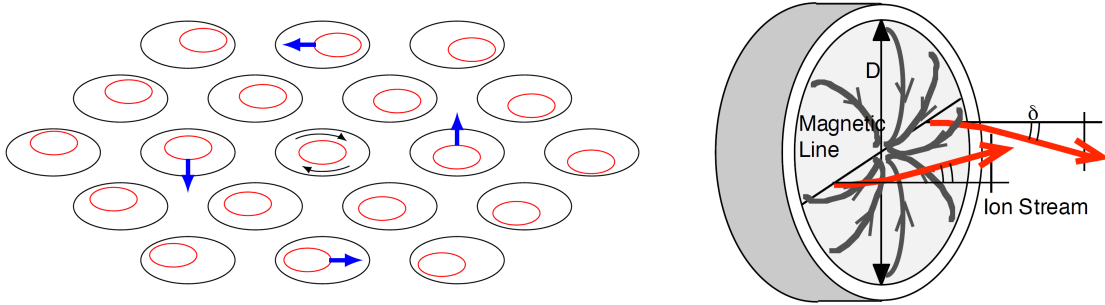
Figure 1.8: Swirl torque generated by grid misalignment and magnetic field leakage. Courtesy of Neil [24] & Hitoshi [25]

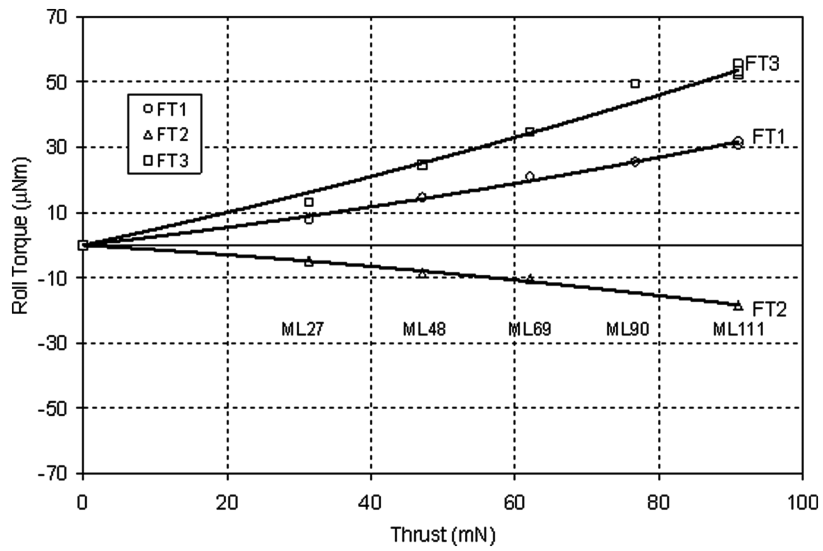|	F_{thr} [mN]	T_{swirl} [mNm]
Hayabusa	8	0.0016
Deep Space 1	20/90	0.01
Smart-1	70	0.06

Table 1.3: Swirl torques measured in different missions

Figure 1.9: Empiric fitting of the swirl torque for different values of thrust from measurements of the Dawn ion thrusters

1.3.3 WOL Techniques

The common procedure of wheel de-saturation is performed by keeping a fixed attitude and imposing a torque through RCS or Magnetotorquers in an opposite direction with respect to the angular momentum stored in the wheels. To maintain the attitude, the wheels commanded torque must be opposite, eventually leading to the decrease of their speed till the momentum is restored. This can be seen by looking at (1.4), where the gyroscopic coupling can be neglected from the dynamics since the attitude is fixed and therefore the angular rate is zero.

$$
\begin{aligned}
\boldsymbol{T}_{imp} &= -k\boldsymbol{h}_{eq} = -kR\boldsymbol{h}_{RW} \\
\boldsymbol{T}_{com} &= -\boldsymbol{T}_{imp} \\
\dot{\boldsymbol{h}}_{RW} &= -R^{\star}\boldsymbol{T}_{com} = R^{\star}\boldsymbol{T}_{imp} = -k\boldsymbol{h}_{RW}
\end{aligned}
\tag{1.4}
$$

A RCS consists of a set of micro-thrusters located at the edges of the satellite body that can be either switched on and off to provide torques about the desired directions. On the other hand, Magnetotorquers provide torques by the interaction of an internally generated magnetic dipole with an external magnetic field. The dipole is obtained by making currents flow inside conductive windings such as rods or coils. Even if a Magnetotorquer does not require to carry additional propellant, it is dependant on the presence and the intensity of the external field and can not provide torques along the external field direction. Examples of the two actuators are shown in *Figure 1.10*.
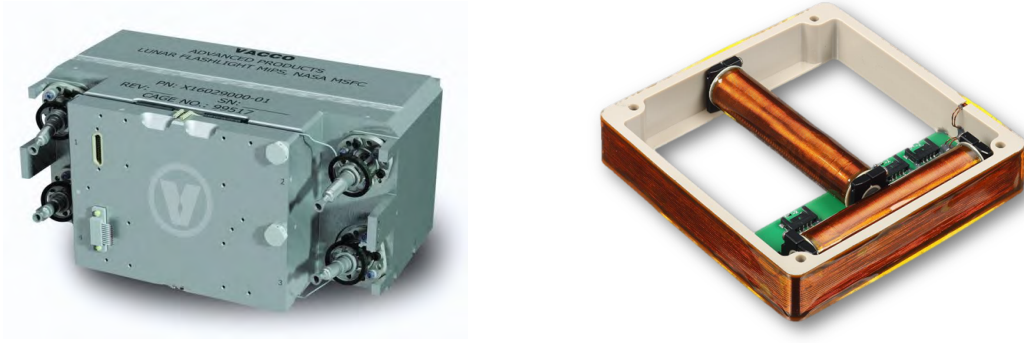
Figure 1.10: Examples of RCS and Magnetotorquers. Courtesy of Vacco [28] & Nano Avionics [29]

Other than these two methods, there are also examples in the literature of torque generation by means of a gimballed thruster and rotation of solar panels.

Gimballed Thrust

Some thrusters are characterized by a two-axis gimbal mechanism that allows the pointing of the thrust vector in the desired direction. For example, the two-axis gimballed thruster of Busek, shown in *Figure 1.11*, allows for excursion angles up to 10°.
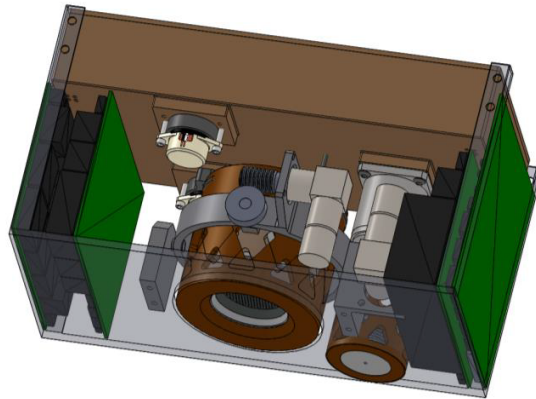

Figure 1.11: Example of a two-axes gimbal mechanism. Courtesy of Busek [30]

By making use of such devices, control torques about the two axes perpendicular to the thruster axis can be accomplished because of the offset of the thrust vector from the spacecraft Center Of Mass (com).

The big challenge is the management of the momentum about the third axis. This has been partially addressed by using the "natural" movement of this axis in specific cases, such as geostationary or lunar transfer orbits [31, 32]. A complete rotation of the body thruster axis generally occurs in one day for the former and in less than one month for the latter cases. The angular momentum stored along it can be dumped later in the orbital arc by off-setting the gimbal like the previous case because the angular momentum is fixed inertially in the axis in which it was originally generated. After sufficient movement along the trajectory, the previously stored momentum becomes orthogonal to the thruster axis and can be off-loaded. However, to use this approach, the rws must be sized to accommodate all the angular momentum generated along the inertial thrust axis until the s/c has moved sufficiently along the orbital arc. For typical deep space missions, with orbital periods around the Sun measured in years, such high capacity rws are not practical, especially in the case of CubeSats.

Alternatively, to produce the torque about the third axis, a series of consecutive mirror maneuvers can be performed by both slewing the s/c and rotating the gimbal, as shown in *Figure 1.12*. In the example, the s/c velocity vector is entering the page. The inertial axis J_i is maintained fixed with the body axis J_b. In the first firing, the s/c slews of 90° about J_i and gimbals the thruster to point the same axis. In the second firing, the slewing is of −90°

and the thruster points in the opposite direction. The sum of the two firings results in a net torque about K_i, without the generation of spurious forces. However, an high control authority is required to perform the slewing and the gimbal must have a large excursion range. Moreover, the propellant is wasted since the thrust is not directed in the desired direction [33].
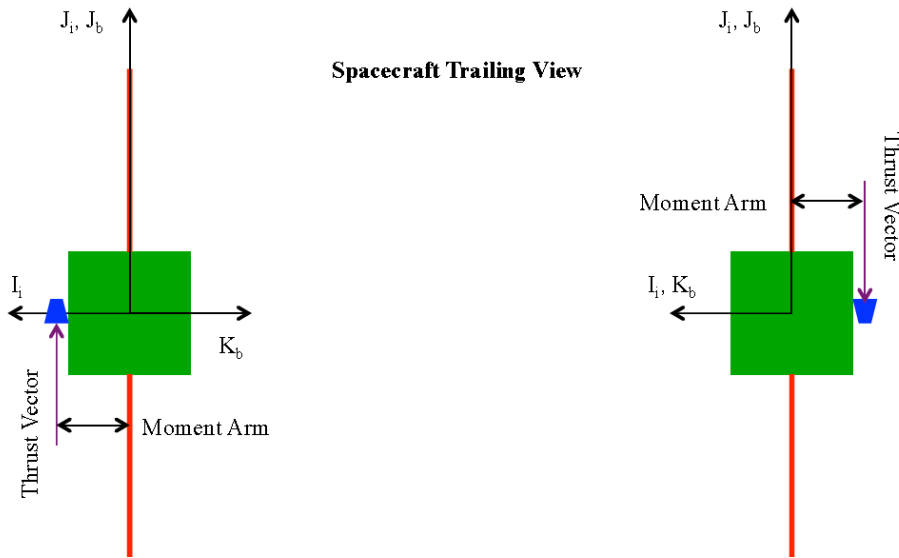

Figure 1.12: Mirror maneuvers to produce a net torque around the roll axis. Courtesy of M. Randolph [33]

As will be further discussed in *subsection 3.3.2*, this situation can be improved with a continuous series of smaller mirror image maneuvers, where both the s/c and the gimbal perform circular trajectories that results in the generation of a continuous torque around the inertial thrust axis, without spurious components.

Solar Panels Sailing

The solar panels sailing consists of the generation of a net force on the panels exposed to the Sun due to the presence of SRP. By using specific configurations of the solar panels, it is possible to generate very light torques, strictly dependant on the sun direction and distance, but that in theory could be used for WOL.

The SRP is obtained as the ratio of the Solar irradiance $\Phi_\odot$ over the light speed c, where the former depends on the Sun distance and the current Sun cycle. The force generated due to this pressure comprises three contributions: the specular reflection, the diffuse reflection, and the absorption. Their magnitude depends on the optical properties of the s/c. Each face is modeled as a flat plate and the force acting on its Center of Pressure (CP)

is computed using the model in (1.5). The torque is then obtained from the cross product with the CP location with respect to the COM [34].
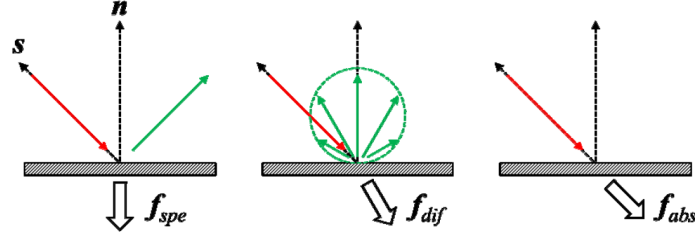
$$F_{SRP} = \begin{cases} -PA(\hat{S} \cdot \hat{n}) \left[\frac{2}{3}\rho_d \, \hat{n} + 2\rho_s(\hat{S} \cdot \hat{n}) \, \hat{n} + (1 - \rho_s) \, \hat{S} \right] & \hat{S} \cdot \hat{n} > 0 \\ 0 & \hat{S} \cdot \hat{n} \leq 0 \end{cases}$$

$$P = \frac{\Phi_\odot}{c}$$

$$\rho_s + \rho_d + \rho_a = 1$$

(1.5)

$$T_{SRP} = d_{CP} \times F$$

For BepiColombo, a differential tilt of the SAs is proposed to balance the disturbance torque that arises from the thruster misalignment with the COM, as shown in *Figure 1.13*. This method is shown to successfully avoid the accumulation of momentum and save RCS propellant with even a few degrees of tilting [35].
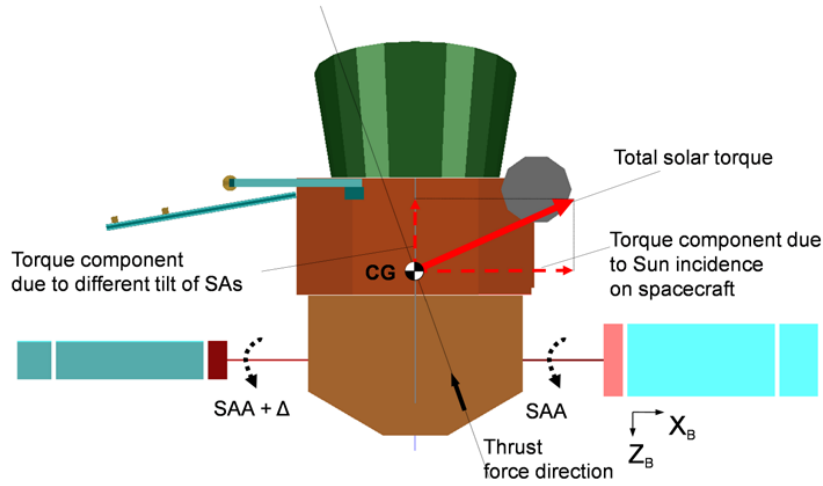
Figure 1.13: Disturbance torque rejection using SRP in BepiColombo

The concept of exploiting the SRP for WOL has been investigated for highly elliptical Keplerian orbit and interplanetary travels, but in both cases, the solutions presented are coupled with the orbital motion and therefore last several weeks [36, 37]. A dedicated WOL maneuver that can be accomplished in timeframes of hours, more versatile in terms of constraints on the satellite mode and nominal attitude, has not been studied yet.

ZPM

The Zero Propellant Maneuver (ZPM) can be defined as the development of an attitude trajectory shaped in a manner that takes advantage of the nonlinear system dynamics and environmental disturbance torques to reduce or eliminate the net cost of a rotation, hence reducing the accumulated momentum.

Euler's rotation theorem states that an arbitrary rotation of a rigid body can be performed by rotating about a body-fixed axis. The rotation axis is called the eigenaxis, while the eigenangle is the smallest angle of rotation about the eigenaxis that reorients the body from the initial attitude to the final attitude. A visual representation of this theorem is in *Figure 1.14*.
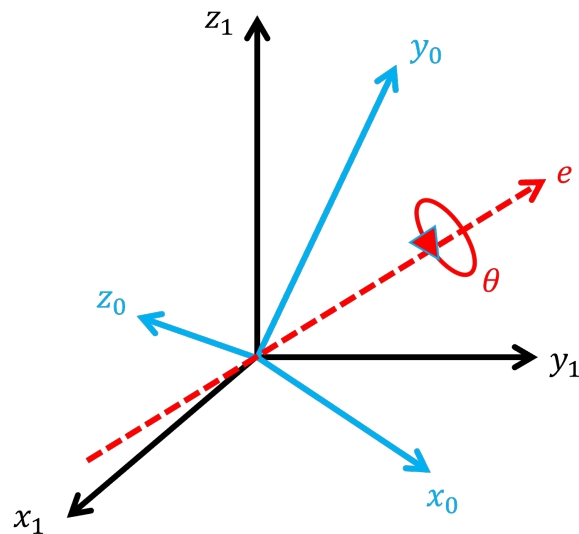
Figure 1.14: Euler's axis and angle

Most s/c rotations are performed about the eigenaxis because it is simple to implement in-flight software and is the shortest kinematic path. However, to follow the eigenaxis path, the controller must overcome environmental disturbance torques, which may saturate the actuators.

The concept of the ZPM is based on the fact that eigenaxis rotations are the shortest angular paths, but they are not time-optimal nor torque-optimal.

As proof of concept, in 2006 and 2007, respectively 90° and 180° rotation of the International Space Station (ISS) were performed with an attitude trajectory shaped so that the environmental disturbance torques were exploited to de-saturate the Control Moment Gyros (CMGs). This maneuver saved RCS propellant for an equivalent amount of about 1.5 million dollars [38].

The ZPM formulation is essentially an Optimal Control problem, where the goal is the minimization of the final momentum, transcribed into a Non-Linear Programming (NLP) problem with a Direct Collocation method. This last is used to parametrize the dynamical state and control variables into polynomials and transform the non-linear dynamics of the system into algebraic constraints to be fulfilled at the nodes of those polynomials. Once the problem is transcribed, the solution is retrieved numerically using NLP solver such as SNOPT or IPOPT.

The procedure is therefore predictive and not performed in real-time. Moreover, high computational capabilities are required by the platform to solve the ZPM problem, if the procedure is meant to be carried out on-board, such as in the case of an autonomous deep-space mission. Amongst all the literature researched, all the solutions rely on the presence of either aerodynamic drag or Gravity Gradient (GG) disturbance torques, if not both [39, 40]. This is another aspect that is not characteristic of a deep-space mission such as the one of M-Argo. For these reasons, the investigation of this WOL method has not been investigated further.

1.4 Research Question

The problem that this original work tries to address and solve can be summarized into the following research question:

> *"Is it possible to autonomously perform a full wheel off-loading in a deep-space scenario without using dedicated momentum-management actuators and without affecting the mission operations and trajectory?"*

1.5 Structure of the Thesis

The thesis is structured in 6 chapters.

In *chapter 1*, the context in terms of satellites and related missions has been firstly presented. Then, a quick overview of the problem and of the motivations that push this investigation has been carried out, followed by a State of the Art analysis in order to pose the proper research question.

In *chapter 2*, an overview of the selected case study will be performed for what regards its mission objectives, operations, and system architecture, to gather the data required for the simulations.

In *chapter 3*, the original work will be illustrated. Several WOL strategies have been developed and then linked together to be executed consequently in an autonomous way through the usage of a SM. Also, the problem of WOL singularity is addressed and a solution is proposed to complete the de-saturation.

In *chapter 4*, the simulation environment will be presented in the form of an astrodynamics simulator, that has been developed to demonstrate the feasibility of the proposed WOL strategies.

In *chapter 5*, the results of the simulations will be disclosed and then validated. The same simulations will be validated in CUBORG and a trajectory comparison will be carried out to understand the impact of the WOL strategies on the orbital path. Moreover, sensitivity analysis will be performed to account for the uncertainties of the model and to check the robustness of the algorithms.

In *chapter 6*, the concluding sections address the lessons learned throughout the previous chapters and the future works that may be carried out to enhance the value of the results and to open doors for a deeper analysis.

2 Case Study: M-Argo

2.1 Overview of the Mission

M-Argo will be the first European Space Agency (esa) stand-alone CubeSat to rendezvous with a nea. Its mission goals are the accomplishment of the first fully autonomous deep-space CubeSat cruise between Earth and an asteroid, the characterization of the asteroid's physical properties as well as the determination of its origin and evolution [11].

The idea was proposed in 2017 by ESA's Concurrent Design Facility (cdf), an highly networked facility aimed to design novel missions. The cdf study showed that the concept would have the potential of cutting the entry-level cost of deep-space exploration by about a factor of ten. While usually CubeSats assumes the availability of a mothership for transport and release into the nominal orbit, M–Argo by contrast will be completely stand-alone since it will be released in a halo parking orbit about the Sun-Earth L2 point. from where it will begin its journey.

M-Argo will demonstrate some innovative technologies, such as a reflectarray antenna for direct-to-Earth X-band communication, a high-performance electric propulsion system, a laser altimeter, and a payload for in-situ resource observation called Asteroid SPECTral imager (aspect).

Moreover, another mission objective will be the testing of autonomous Guidance Navigation and Control (gnc) techniques and components performance during the transfer. For instance, an autonomous navigation experiment will be carried out to estimate the state of the s/c with an optical camera called NavCam, without relying on ground station tracking.

2.2 Transfer Trajectory

The expected launch date is between 2023 and the end of 2024, with a maximum transfer time of 3 years. A NEA target screening has been carried out during the mission analysis phase to identify the envelope of the most promising asteroids reachable by M-Argo in the provided time frame [41]. The first filtering based on minimum-time and minimum-fuel criteria shortlisted to 148 the number of targets from the initial database of more than 700 000 asteroids. Then, after observation of the Porkchop plots and depending on the availability of already known information about the targets, such as the light curve or the spin rate, the envelope was reduced to 5. For each of them, a baseline and backup trajectory were established, whose data is reported in *Table 2.1*.

NEA	Type	t_{start}	TOF $[d]$	m_p [kg]
2000-SG344	Baseline	08 Nov 2023	833	1.156
	Backup	07 Nov 2024	707	1.051
2010-UE51	Baseline	17 Sep 2023	581	0.974
	Backup	16 Sep 2024	861	1.787
2011-MD	Baseline	05 Jun 2023	854	1.536
	Backup	13 Apr 2024	742	1.386
2012-UV136	Baseline	08 Nov 2023	805	1.895
	Backup	07 Nov 2024	861	2.313
2014-YD	Baseline	27 Jul 2023	721	1.966
	Backup	26 Jul 2024	651	1.518

Table 2.1: Selection results of the screening process of the reachable asteroids

In this work, the baseline trajectory to reach asteroid 2010-UE51 will be considered. Between the shortlisted targets, this NEA grants both the shortest TOF and lowest fuel consumption. M-Argo trajectory and thrust profile to reach it are reported in *Figure 2.1* and *Figure 2.2*.

The thrust profile presents *thrust bins* because it is characterized by activity segments of the duration of 7 days. In each segment, cruising arcs of 6 days and coasting arcs of 1 day are identified during which the thruster is switched on and off respectively. During the coasting arcs, maintenance operations are performed, like platform House-Keeping (HK) and communication with the ground, but also autonomous GNC experiments can be carried out [42].

In this work, WOL strategies based on the gimballed thruster will be simulated along the first 24 hours of a pre-selected cruising arc to check the consequences of the WOL maneuvers in the orbit propagation with respect to the case without WOL. The cruising arc
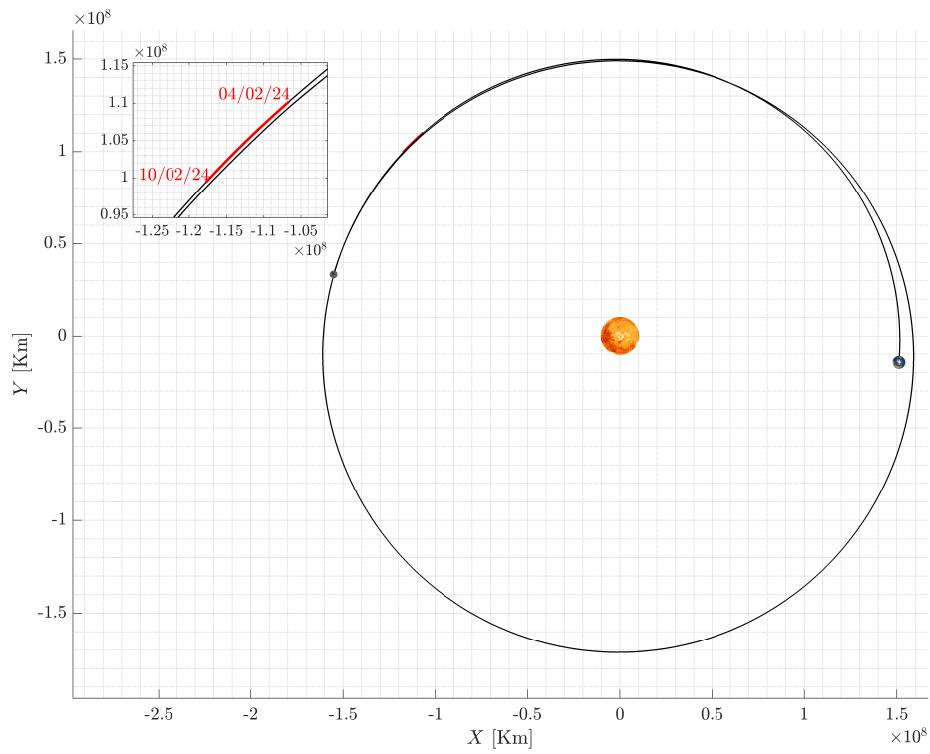
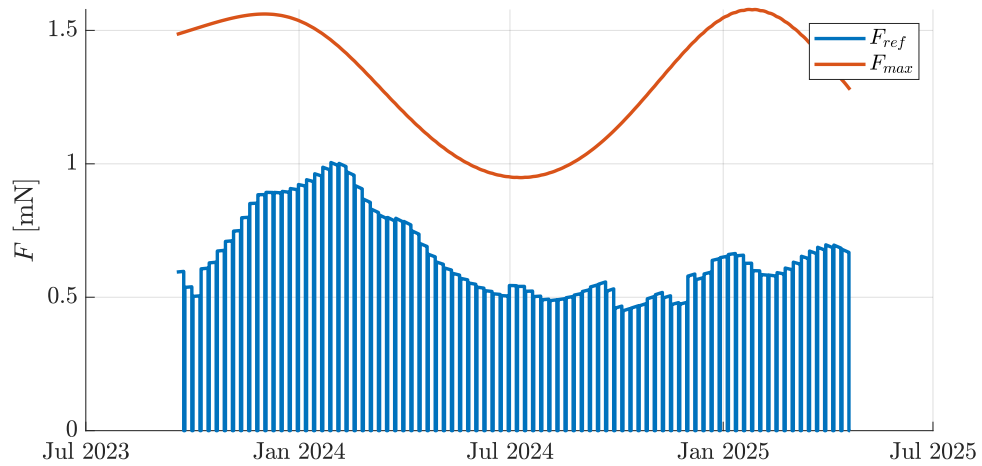Figure 2.1: Fuel-optimal trajectory to 2010-UE51 (planets not in scale)

Figure 2.2: Maximum and reference thrust during the fuel-optimal trajectory

that gives the worst-case scenario is the one where there is the lowest difference between the reference thrust level and the maximum one. This is explained by the fact that during WOL the thrust will likely need to be higher than the reference value due to the offsetting of the gimbal and this puts a constraint on the operations.

According to these considerations, the chosen cruising arc is between 4 and 10 February 2024. The WOL strategies based on SP can be simulated in any coasting arc because there are no restrictions in terms of thrust. For simplicity, the coasting arc chosen is consequent to the cruising one, between 10 and 11 February 2024. The orbital path and the correspondent pointing vector along the activity segment are depicted in *Figure 2.3*, while the power and thrust levels are reported in *Figure 2.4*.
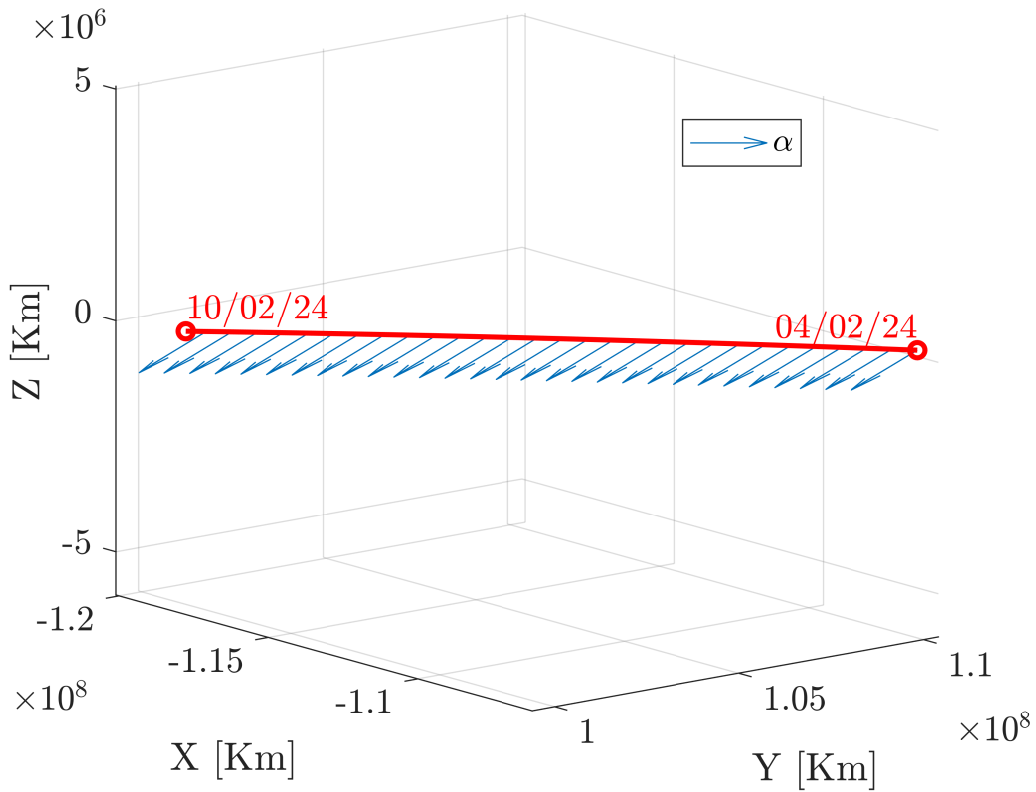
Figure 2.3: Pointing vector during the cruising arc of 4-10 February 2024
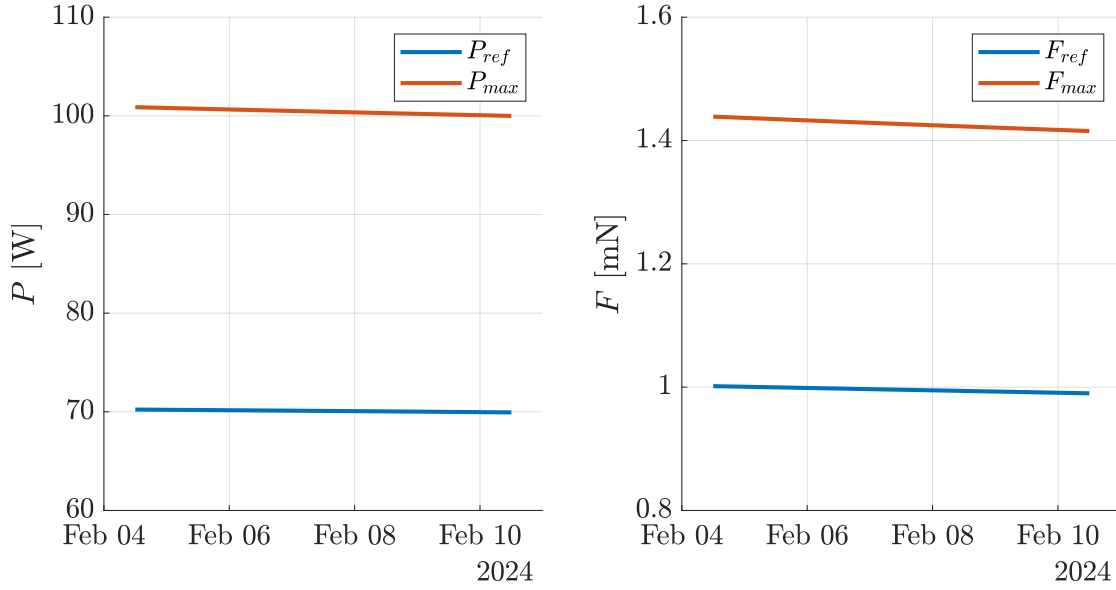
Figure 2.4: Reference and maximum thrust and power during the cruising arc of 4-10 February 2024

2.3 System Architecture

M-Argo is a 12U-XL CubeSat with the dimensions and mass reported in *Table 2.2*. It is characterized by two huge SAs, each one with 4 6U-XL panels. Since the SPs play an important role in the simulations of the coasting WOL strategies, accurate data must be used. As the design is still in phase A, the GomSpace MSP-B-8-2 has been selected as SP unit for the purpose of this work because it was the commercial product that most resembled the design described in the M-Argo system design report. Moreover, GomSpace is the main contractor for the mission so the choice was straightforward [43].

Body [43]	
a	0.25 m
b	0.25 m
c	0.366 m
m_{tot}	27.5 kg

SP [44]	
h_{SP}	0.209 m
l_{SP}	0.3265 m
m_{SP}	0.453 kg

SA	
h	0.209 m
l	1.306 m
m_{SW}	1.812 kg
l_h	0.1633 m

Table 2.2: Physical properties of M-Argo platform, solar panel and solar array

The size and mass of each SP are used to compute the SA physical properties. The hinge length l_h has been set equal to the half of l_{SP} because the SA are center-mounted and the deployment mechanism follows a 3-steps sequence.

A rendering of the s/c in packed and deployed configuration can be seen in *Figure 2.5* and *Figure 2.6* respectively. A CAD model in SolidWorks has been realized according to the aforementioned data, which will be used for the strategies explanations and consequent simulations in the following chapters.

The computation of the SRP torques requires the knowledge of the areas of the faces, as well as their normals and CP locations. The surfaces are computed from the body and SAS dimensions and collected in the vector A. Since the SAS can change orientation, their normals are parametrized on the tilting angles Δ_1 and Δ_2. The normals matrix N_b is constructed in such a way that the panels face $+z$ when the tilting angle is zero. Finally, the CP position vectors of each face are collected into the D_{CP} matrix. All the parameters are reported in (2.1).

$$A = \begin{bmatrix} b\,c & a\,c & a\,b & b\,c & a\,c & a\,b & h\,l & h\,l & h\,l & h\,l \end{bmatrix}$$

$$N_b = \begin{bmatrix} 1 & 0 & 0 & -1 & 0 & 0 & \sin\Delta_1 & -\sin\Delta_1 & \sin\Delta_2 & -\sin\Delta_2 \\ 0 & 1 & 0 & 0 & -1 & 0 & 0 & 0 & 0 & 0 \\ 0 & 0 & 1 & 0 & 0 & -1 & \cos\Delta_1 & -\cos\Delta_1 & \cos\Delta_2 & -\cos\Delta_2 \end{bmatrix}$$

$$D_{CP} = \begin{bmatrix} \frac{a}{2} & 0 & 0 & -\frac{a}{2} & 0 & 0 & 0 & 0 & 0 & 0 \\ 0 & \frac{b}{2} & 0 & 0 & -\frac{b}{2} & 0 & d_{SP} & d_{SP} & -d_{SP} & -d_{SP} \\ 0 & 0 & \frac{c}{2} & 0 & 0 & -\frac{c}{2} & 0 & 0 & 0 & 0 \end{bmatrix}$$

$$\text{where} \quad d_{SP} = \frac{b}{2} + l_h + \frac{l}{2}$$

(2.1)

Other physical properties that have a large weight in the simulation results are the optical properties of the surfaces. The absorption, specular and diffusive coefficients considered are the ones associated with anodized aluminum for the body faces and the last-generation solar cells for the SP [45]. The coefficients are reported in *Table 2.3*.

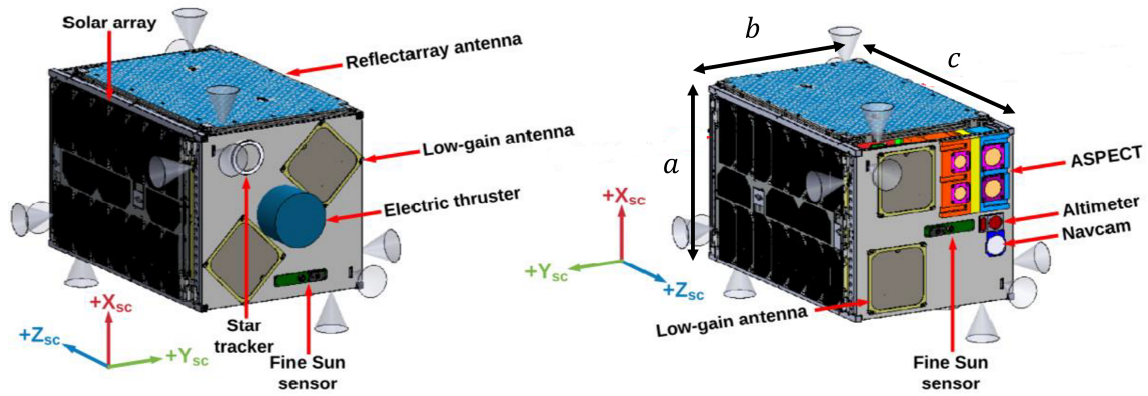|	Body	SP
ρ_s	0.8	0.0727
ρ_d	0.08	0.007

Table 2.3: Optical properties of M-Argo

Figure 2.5: M-Argo in packed configuration. Courtesy of GomSpace [43]
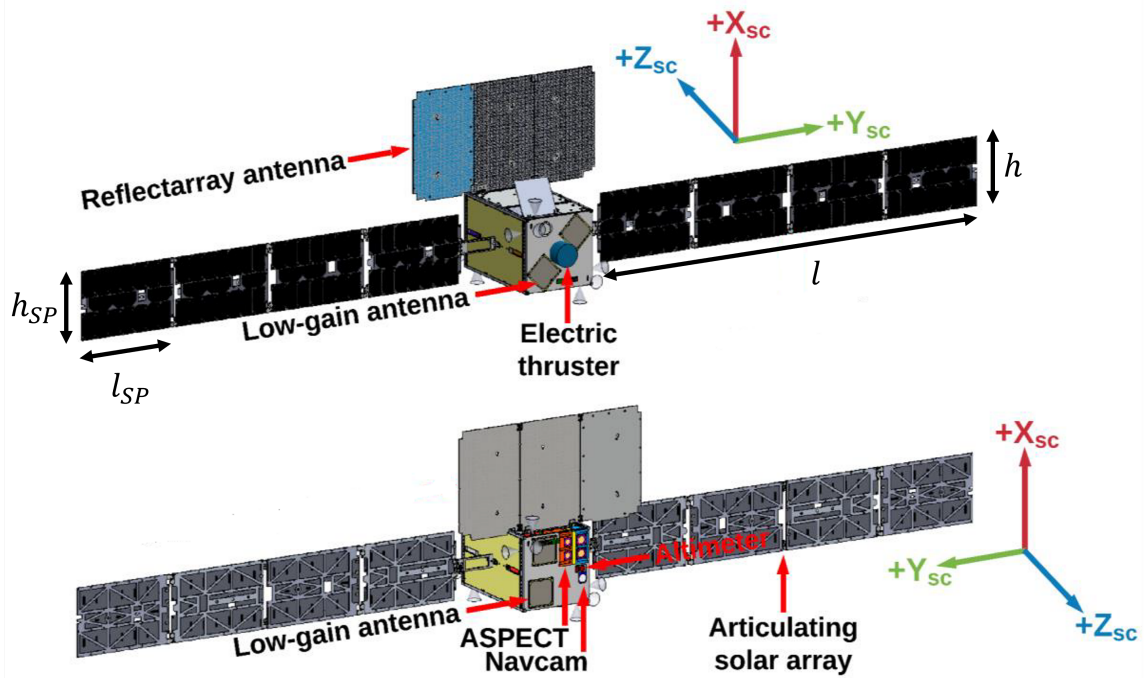

Figure 2.6: M-Argo in deployed configuration. Courtesy of GomSpace [43]

2.4 AOCS Architecture

The Attitude and Orbit Control System (AOCS) is the subsystem responsible for the determination and control of the position and the attitude of the satellite, exploiting onboard sensors and actuators. To this aim, three distinct functions can be identified:

- **Navigation**. This branch is dedicated to the estimation of position and attitude, also referred to as *pose*, from the sensors' measurement.

- **Guidance**. The guidance trajectories represent the desired state and they must be furnished to the control to compute the error. Usually, information on pointing direction and trajectory to follow are stored in the internal memory of the satellite and extracted when needed.

- **Control**. The goal of this function is to use actuators to have an ideally null error between the desired and actual pose of the satellite.

Regarding sensors, 2 Star Tracker (STR) and 6 Fine Sun Sensor (FSS) are used for attitude determination, while the angular rate and linear accelerations are measured by a Inertial Measurement Unit (IMU). The three sensors, together with their data, are shown in *Figure 2.7*.

STR [46]	
ϵ_{roll}	$10\,''$
$\epsilon_{\text{yaw/pitch}}$	$60\,''$

IMU [48]	
ω_{max}	$400\,°/\text{s}$
$\Delta\omega_{min}$	$0.2\,°/\text{s}$
$\Delta\omega_{bias}$	$0.3\,°/\text{s}$
ARW	$0.15\,°/\sqrt{\text{h}}$

FSS [47]	
FOV	$60\,°$
ϵ	$2\,°$
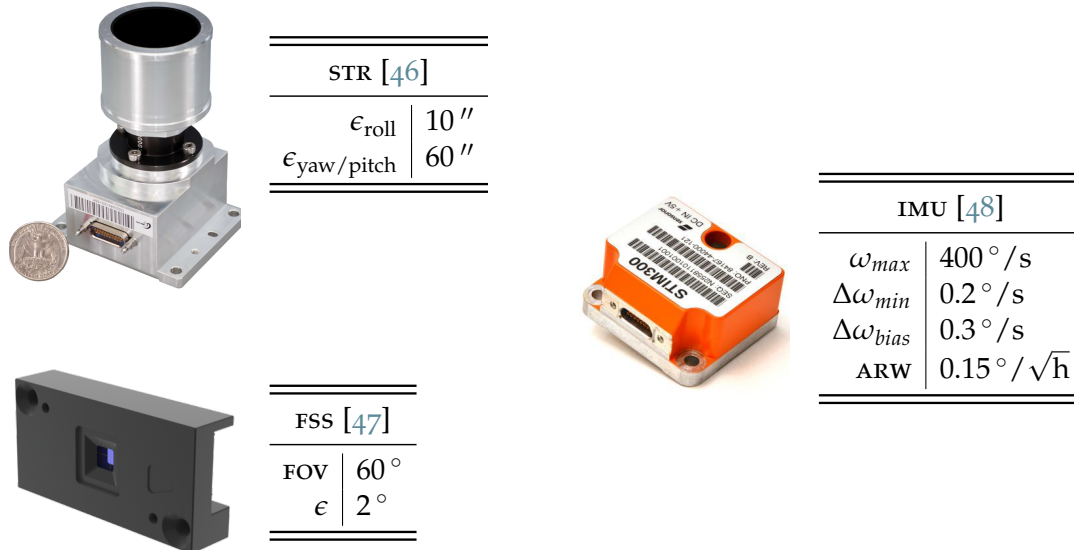
Figure 2.7: Pictures and data of M-Argo sensors

The STR is a high-precision but slow sensor that can retrieve the attitude by comparison of what it records in its Field Of View (FOV) with a star catalog stored in the internal memory.

The initial comparison takes a lot of time because of the high computational effort, but once the stars are identified, they can be tracked and the attitude knowledge is updated faster. Due to this issue, also FSS are employed. These are more reactive sensors that give a two-axis measurement of the Sun direction. Since the measure depends on the presence of the Sun, they are usually located on multiple faces of the CubeSat, to constantly retrieve its direction regardless of the attitude. Their measure is less precise than STR, but it is useful to track the Sun with SPS for power maximization and during de-tumbling, where the STR fails in performing the acquisition. The accuracy ϵ is typically on the order of arcseconds for a STR and on the order of degrees for a FSS.

Finally, the IMU exploits miniaturized Micro Electro-Mechanical Systems (MEMS) gyroscopes and accelerometers to measure the relative rate of change of attitude and velocity of the body. This sensor is characterized by a range ω_{max} of the maximum rate that can be measured, a minimum sensitivity tolerance $\Delta\omega_{min}$, and two type of errors: the bias instability $\Delta\omega_{bias}$ and the Angle Random Walk (ARW). While the former expresses the deviation that the sensor has from its mean value of the output rate, the latter will increase the longer the signal is integrated, and therefore provides a fundamental limitation to any angle measurement that relies solely on the integration of rate.

Regarding actuators, M-Argo encompasses 4 RWs in a pyramid configuration along -x and a set of 12 RCS distributed in triads in the corners, whose locations $\boldsymbol{d}_{RCS}$ and thrust directions $\hat{\boldsymbol{n}}_{RCS}$ are reported in (2.2). The pointing of the RCS thrusters is also labelled by cones in *Figure 2.5*.

$$
\boldsymbol{d}_{RCS} = \frac{1}{2}\begin{bmatrix} b & b & b & b & b & b & -b & -b & -b & -b & -b & -b \\ b & b & b & -b & -b & -b & -b & -b & -b & b & b & b \\ c & c & c & -c & -c & -c & c & c & c & -c & -c & -c \end{bmatrix}
$$
$$
\hat{\boldsymbol{n}}_{RCS} = \begin{bmatrix} 1 & 0 & 0 & 1 & 0 & 0 & -1 & 0 & 0 & -1 & 0 & 0 \\ 0 & 1 & 0 & 0 & -1 & 0 & 0 & -1 & 0 & 0 & 1 & 0 \\ 0 & 0 & 1 & 0 & 0 & -1 & 0 & 0 & 1 & 0 & 0 & -1 \end{bmatrix} \tag{2.2}
$$

The maximum torque and saturation level of the RWs are reported in *Table 2.4*, as well as the maximum thrust force and specific impulse of the RCS thrusters.

RWS [49]		RCS [43]	
T_{max}	2 mNm	F_{max}	1 mN
h_{max}	19 mNms	I_{sp}	16 s

Table 2.4: Data of M-Argo actuators

The propulsion system is based on a radiofrequency-based gridded ion engine with a

gimbal mechanism that can have excursions up to $15°$. Xenon is used as propellant by both thruster and RCS and stored in shared tanks.

Since a commercial solution for the engine has not been selected at the time of writing, the maximum thrust level and specific impulse are computed through 4th order polynomial fitting from the input power. This last is in turn retrieved again through fitting from the s/c distance from the Sun, expressed in Astronomic Unit (AU), and is bounded within a minimum and maximum value before being provided to the thruster. The fitting polynomials are reported in (2.3) and the correspondent set of coefficients in *Table 2.5*.

$$T_{\text{max}} = a_0 + a_1 P_{in} + a_2 P_{in}^2 + a_3 P_{in}^3 + a_4 P_{in}^4$$
$$I_{sp} = b_0 + b_1 P_{in} + b_2 P_{in}^2 + b_3 P_{in}^3 + b_4 P_{in}^4 \qquad 80 \text{ W} < P_{in} < 130 \text{ W} \qquad (2.3)$$
$$P_{in} = c_0 + c_1 r + c_2 r^2 + c_3 r^3 + c_4 r^4$$

i	a_i [mN]	b_i [s]	c_i [W]
0	-1.2343	-5519.5	840.11
1	0.026498	225.44	-1754.3
2	0	-1.8554	1625.01
3	0	0.005084	-739.87
4	0	0	134.45

Table 2.5: Fitting coefficients for thrust, specific impulse and power

3
WOL Strategies

3.1 Attitude Parameters

T-HE coordinates that describe the orientation of a given reference frame with respect to a second reference frame are called attitude parameters. In this chapter, the Direction Cosines Matrix (DCM) will be considered. This is a transformation matrix that is constructed concatenating three sets of direction cosines, where each set locates one of the three axes of the second frame in the first frame, respectively called *b* and *n* in *Figure 3.1*.

Once the DCM is found, it can be used to express the same vector from one frame to another by simple matrix multiply, as specified in (3.1). The inverse transformation employs the transpose of the DCM thanks to the property of transformation matrices of orthonormal reference frames to be orthonormal too.

$$
\begin{aligned}
\boldsymbol{r}_b &= A_{b/n}\boldsymbol{r}_n \\
\boldsymbol{r}_n &= A_{n/b}\boldsymbol{r}_b = A_{b/n}^{-1}\boldsymbol{r}_b \equiv A_{b/n}^{T}\boldsymbol{r}_b
\end{aligned}
\tag{3.1}
$$

$$\hat{b}_1 = \cos\alpha_{11}\hat{n}_1 + \cos\alpha_{12}\hat{n}_2 + \cos\alpha_{13}\hat{n}_3$$
$$\hat{b}_2 = \cos\alpha_{21}\hat{n}_1 + \cos\alpha_{22}\hat{n}_2 + \cos\alpha_{23}\hat{n}_3$$
$$\hat{b}_3 = \cos\alpha_{31}\hat{n}_1 + \cos\alpha_{32}\hat{n}_2 + \cos\alpha_{33}\hat{n}_3$$

$$A_{b/n} = \begin{bmatrix} \cos\alpha_{11} & \cos\alpha_{12} & \cos\alpha_{13} \\ \cos\alpha_{21} & \cos\alpha_{22} & \cos\alpha_{23} \\ \cos\alpha_{31} & \cos\alpha_{32} & \cos\alpha_{33} \end{bmatrix}$$
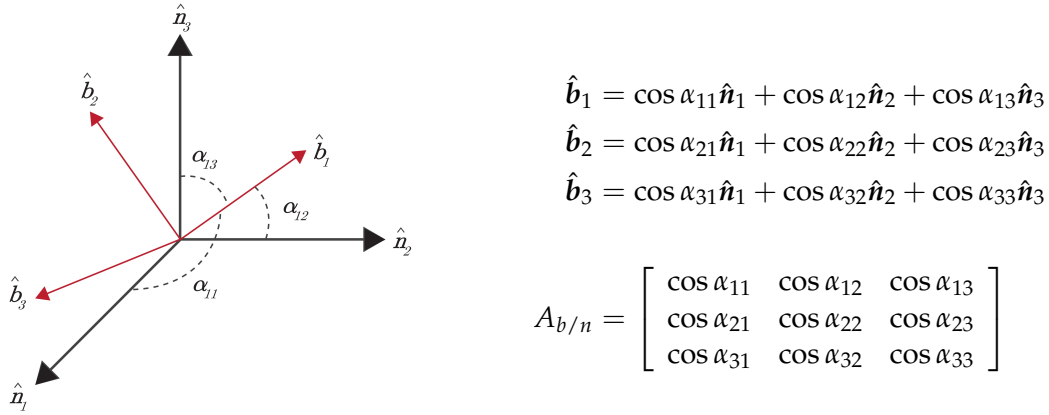
Figure 3.1: How to construct a DCM. Courtesy of VectorNav [50]

3.2 Reference Frames

Before proceeding with the strategies description, three reference frames are identified.

- **Inertial Frame**. Denoted with n, this frame is non-rotating with respect to stars and its origin is non-accelerating. The X-axis is aligned with Earth's mean equinox, obtained by the intersection of the Earth's equatorial and ecliptic planes on January 1st 2000 at midday. The Z-axis is aligned with the Earth's spin axis and the Y-axis completes the triad.

- **Pointing Frame**. Denoted with p, this frame is slowly rotating according to the s/c pointing vector $\hat{\alpha}$ and the sun direction $\hat{S}$. The α-axis is aligned with the pointing vector, the β-axis is perpendicular to the sun direction and to the α-axis, and the δ-axis completes the triad. This is the frame in which the guidance trajectories for the attitude and the gimbal mechanism will be expressed. The orientation of this frame with respect to the inertial frame is obtained with (3.2) in terms of DCM.

- **Body Frame**. Denoted with b, this frame is fixed with the s/c geometric axes. The z-axis is aligned with the thruster direction, the y-axis with the SA axis, and the x-axis completes the triad. During cruising, the body frame should ideally coincide with the pointing frame, because the thruster should be pointed along the pointing vector and the solar panels should be aligned perpendicularly to the Sun to maximize the power income. However, during WOL strategies that involve an attitude motion, the two frames could become misaligned.

$$\alpha = \hat{\boldsymbol{\alpha}}$$
$$A_{p/n} = \begin{bmatrix} \delta & \beta & \alpha \end{bmatrix}^T \qquad \beta = \hat{\boldsymbol{\alpha}} \wedge \hat{\boldsymbol{S}} \qquad (3.2)$$
$$\delta = (\hat{\boldsymbol{\alpha}} \wedge \hat{\boldsymbol{S}}) \wedge \hat{\boldsymbol{\alpha}}$$

A sketch of the three frames in a general situation is reported in *Figure 3.2*.
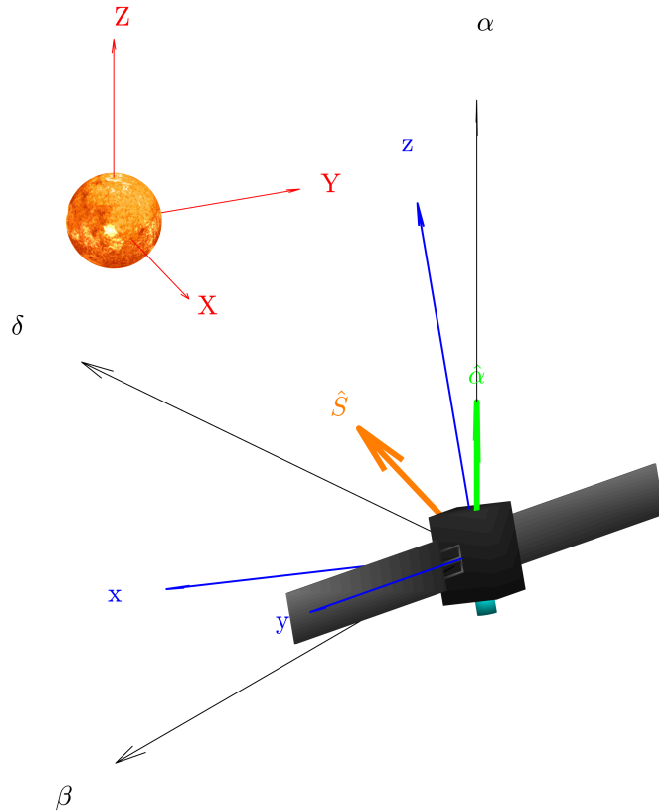

Figure 3.2: Inertial, pointing and body frames

3.3 Cruising Strategies

The WOL strategies during cruising involve the use of the gimbal mechanism of the thruster. As pointed out in (3.3), the gimballed thrust direction $\hat{\boldsymbol{g}}$ can be expressed in terms of the excursion angles θ_1, around the *y*-axis, and θ_2, around the *x*-axis. For the strategies that will require an attitude motion, the orientation of the body with respect to the pointing
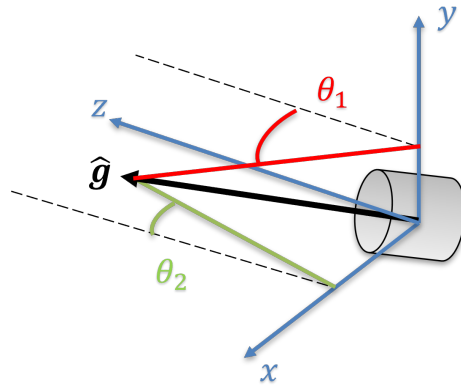
$$\hat{g}_b = \begin{bmatrix} \sin\theta_1 \\ \sin\theta_2 \\ \sqrt{1 - (\sin\theta_1)^2 - (\sin\theta_2)^2} \end{bmatrix} \tag{3.3}$$

frame can be linked to the attitude angles ϕ_1 and ϕ_2, which represents the slewing around the β-axis and δ-axis respectively. The DCM is expressed in (3.4), where each row is the projection of the correspondent body axis on the pointing frame. By imposing the desired angles at each instance, the guidance trajectory for the attitude of the S/C is obtained.
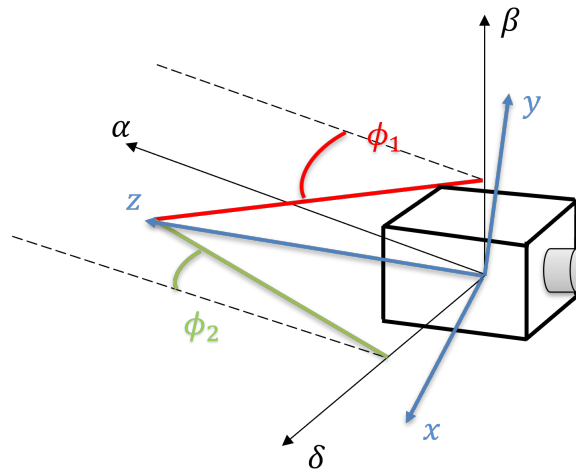
$$A_{b/p} = \begin{bmatrix} \cos\phi_1 & 0 & -\sin\phi_1 \\ 0 & \cos\phi_2 & -\sin\phi_2 \\ \sin\phi_1 & \sin\phi_2 & \sqrt{1 - (\sin\phi_1)^2 - (\sin\phi_2)^2} \end{bmatrix} \tag{3.4}$$

Both the previous expressions are not valid for large angles, because the term under the

square root becomes negative. However, this is not of concern since angles of no more than $25°$ will be imposed.

During cruising, the satellite is subjected to a reference thrust force $\boldsymbol{F}_{ref}$ aligned along $\hat{\boldsymbol{\alpha}}$. If the gimbal mechanism is used, the direction of the thrust changes to $\hat{\boldsymbol{g}}$ and the thrust must eventually increase to a new level $F_{com} > F_{ref}$ to still have the same intensity along the pointing vector. In other words, the projection of the actual thrust force $\boldsymbol{F}_{com}$ along $\hat{\boldsymbol{\alpha}}$ must be equal to F_{ref}. This condition is imposed in (3.5) to obtain the commanded throttle level. Note that the gimbal vector must be expressed in the inertial frame to have a valid dot product, so it is rotated accordingly by $A_{n/b}$.

$$
\begin{aligned}
\boldsymbol{F}_{ref} &= F_{ref}\,\hat{\boldsymbol{\alpha}} \\
\boldsymbol{F}_{com} &= F_{com}\,\hat{\boldsymbol{g}} = F_{com}\left(A_{n/b}\,\hat{\boldsymbol{g}}_b\right) \\
\boldsymbol{F}_{com}\cdot\hat{\boldsymbol{\alpha}} = F_{ref} \quad\rightarrow\quad F_{com} &= \frac{F_{ref}}{\left(A_{n/b}\,\hat{\boldsymbol{g}}_b\right)\cdot\hat{\boldsymbol{\alpha}}}
\end{aligned}
\tag{3.5}
$$

3.3.1 Gimbal

The previous expression maps the thrust level to the imposed gimbal angles, which are therefore the only DOFs if the attitude is fixed.

According to (3.6), the torques can be generated only around x-axis and y-axis because the thruster is located along the z-axis, assuming that the COM is coincident with the geometric center of the body. This last assumption will be relaxed in *subsection 5.5.2*.

$$
\boldsymbol{T} = \boldsymbol{d}_{thr}\times\boldsymbol{F}_b =
\begin{bmatrix} 0 \\ 0 \\ -\frac{c}{2} \end{bmatrix}
\times F\hat{\boldsymbol{g}}_b = F
\begin{bmatrix} \frac{c}{2}\sin\theta_2 \\ -\frac{c}{2}\sin\theta_1 \\ 0 \end{bmatrix}
\tag{3.6}
$$

As it can be seen, the torque magnitudes are directly proportional to the sine of the gimbal excursion angles. Therefore, this strategy aims to find a solution to the following problem:

"Which is the combination of θ_1 and θ_2 required to dump at the same time h_x and h_y, without ending with spurious momentum on the other axes?"

The higher the torque, the larger the value of momentum that can be off-loaded. Therefore, the ratio of the angular momentum can be approximated to the ratio of the torques required to dump them. The relation in (3.7) can be obtained.

$$
\frac{h_y}{h_x} \approx \frac{T_y}{T_x} = \frac{-\frac{c}{2}\sin\theta_1}{\frac{c}{2}\sin\theta_2} = -\frac{\sin\theta_1}{\sin\theta_2}
\tag{3.7}
$$

Thanks to the previous expression it is possible to compute one excursion angle once fixed the other one, depending on the initial angular momentum. The angle that is first imposed is the one associated with the highest angular momentum and is set equal to a pre-selected maximum value of 5°. Depending on the signs of the angular momentum, the other gimbal angle is computed using (3.8).

$$|h_x| > |h_y| \rightarrow \begin{cases} \theta_2 = -\theta_{max} \operatorname{sgn}(h_x) \\ \\ \theta_1 = \arcsin\left(-\frac{h_y}{h_x} \sin\theta_2\right) \end{cases}$$

$$|h_x| < |h_y| \rightarrow \begin{cases} \theta_1 = \theta_{max} \operatorname{sgn}(h_y) \\ \\ \theta_2 = \arcsin\left(-\frac{h_x}{h_y} \sin\theta_1\right) \end{cases}$$

(3.8)

The maximum angle is a tunable parameter according to how fast the WOL should be performed. However, it should be accounted that with higher off-sets the undesired components of the thrust increase, and the trajectory could be compromised.

This logic ends up dumping at the same time the momentum stored in x and y, as shown in *Figure 3.3*, where an initial momentum of $h_0 = [19 \ -4 \ \ 0]$ mNms is considered.
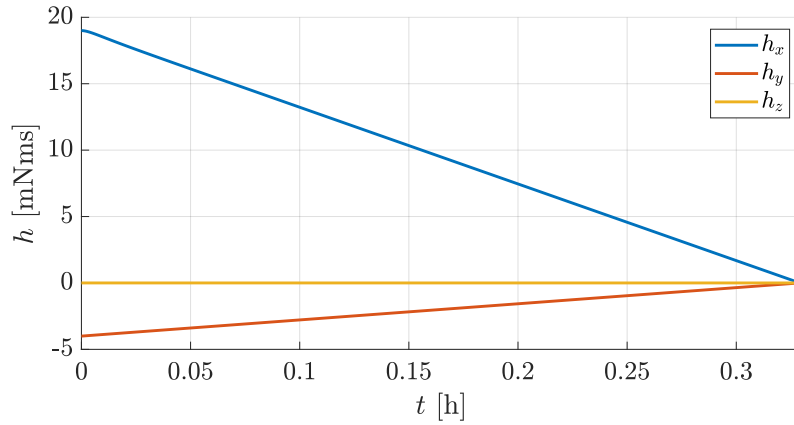
Figure 3.3: De-saturation of the x and y axes employing the Gimbal strategy

3.3.2 BETA Trajectory

In a general case, only torques around x-axis and y-axis can be produced, because regardless of the gimbal angles, the cross product between the thruster location and the thrust force will always be perpendicular to z. However, this does not imply that the momentum accumulated on the z-axis can not be off-loaded. In fact, by coupling a gimbal trajectory with an attitude motion, torques around the α-axis can be obtained, which will eventually dump the momentum on z.

The concept is based on the fact that, as long as no external torques are applied, angular momentum components are conserved in a *fixed* frame. When the attitude changes, and therefore the body frame displaces from the pointing frame, the momentum stored in the RWs will change its distribution, but not its norm nor the value of its components if these are expressed in an inertial frame. Due to its slow dynamics, the pointing frame can be considered inertial in a first approximation. This means that the momentum along the α-axis will remain constant unless external torques are applied. Therefore, the goal of this strategy is to generate a torque around this axis, such that when the attitude is restored, the momentum in the RWs will re-distribute itself again, but the one along z will be eventually removed.

This torque could be easily obtained with the mirror maneuvers presented in *section 1.3.3*. However, in the considered cruising scenario this would mean an interruption of the operations, with a consequent trajectory correction, as well as large slewing maneuvers. Instead, a solution that involves low gimbal and attitude angles excursions and does not produce net torques about x and y axes should be searched. In particular, the question to be answered is:

> *"Which are the guidance laws of θ_1, θ_2, ϕ_1 and ϕ_2 required to dump h_z, without ending with spurios momentum on the other axes?"*

The solution to this problem involves coupled circular attitude and gimbal trajectories, shifted of $90°$ [33]. From a fixed observer point of view, both the gimbal axis and the z-axis would perform a helix while the CubeSat proceeds along its track. This strategy has been therefore called Bi-Elicoidal Thruster-Attitude (BETA) trajectory.

The guidance laws are reported in (3.9) and account also for the sign of h_z, imposing clockwise or anticlockwise motions of the gimbal mechanism and of the attitude trajectory.

To ease the understanding, the sequence along one period T is shown in *Figure 3.4*.

For this strategy the tunable parameters are three:
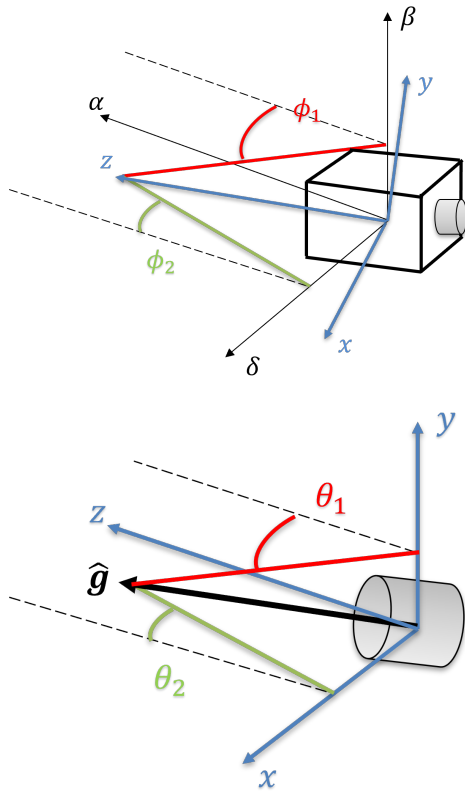
$$\phi_1 = \phi_{max} \sin(\omega t) \operatorname{sgn}(h_z)$$
$$\phi_2 = \phi_{max} \cos(\omega t)$$

$$\theta_1 = -\theta_{max} \cos(\omega t) \operatorname{sgn}(h_z)$$
$$\theta_2 = \theta_{max} \sin(\omega t)$$

(3.9)

$$\omega = 2\pi f = \frac{2\pi}{T}$$

- ϕ_{max} is the maximum attitude angle. The higher the maximum excursion, the larger the torque generated but the more pronounced will be the oscillations of h_x and h_y. A value of 5° is found to be a good compromise to perform the WOL in a reasonable time and avoid reaching too high values of angular momentum on the other axes.

- θ_{max} is the maximum thruster angle. The effects of increasing it are the same as before, with also the additional issue of higher consumption of propellant if the constraint on the reference thrust along $\hat{\alpha}$ must be respected. For this reason, the value is kept to 5°.

- T is the period of the circular motions. If the period is reduced, the oscillations will be faster and therefore the amplitudes would increase because a higher slope means a higher torque. On the other hand, if the period is too long, h_z could reach zero when the cycle is not finished yet, leaving spurious momentum on x and y axes. A period of 20 min has been found to be acceptable from both points of view.

Imposing the afore-mentioned parameters, the desired gimbal angles and attitude angles are reported in *Figure 3.5*. Considering an initial condition of $h = \begin{bmatrix} 0 & 0 & 10 \end{bmatrix}$ mNms, the correspondent angular momentum trend is depicted in *Figure 3.6*, where the oscillations of

$t = 0$

$t = \frac{T}{4}$

$t = \frac{3T}{4}$

$t = \frac{T}{2}$
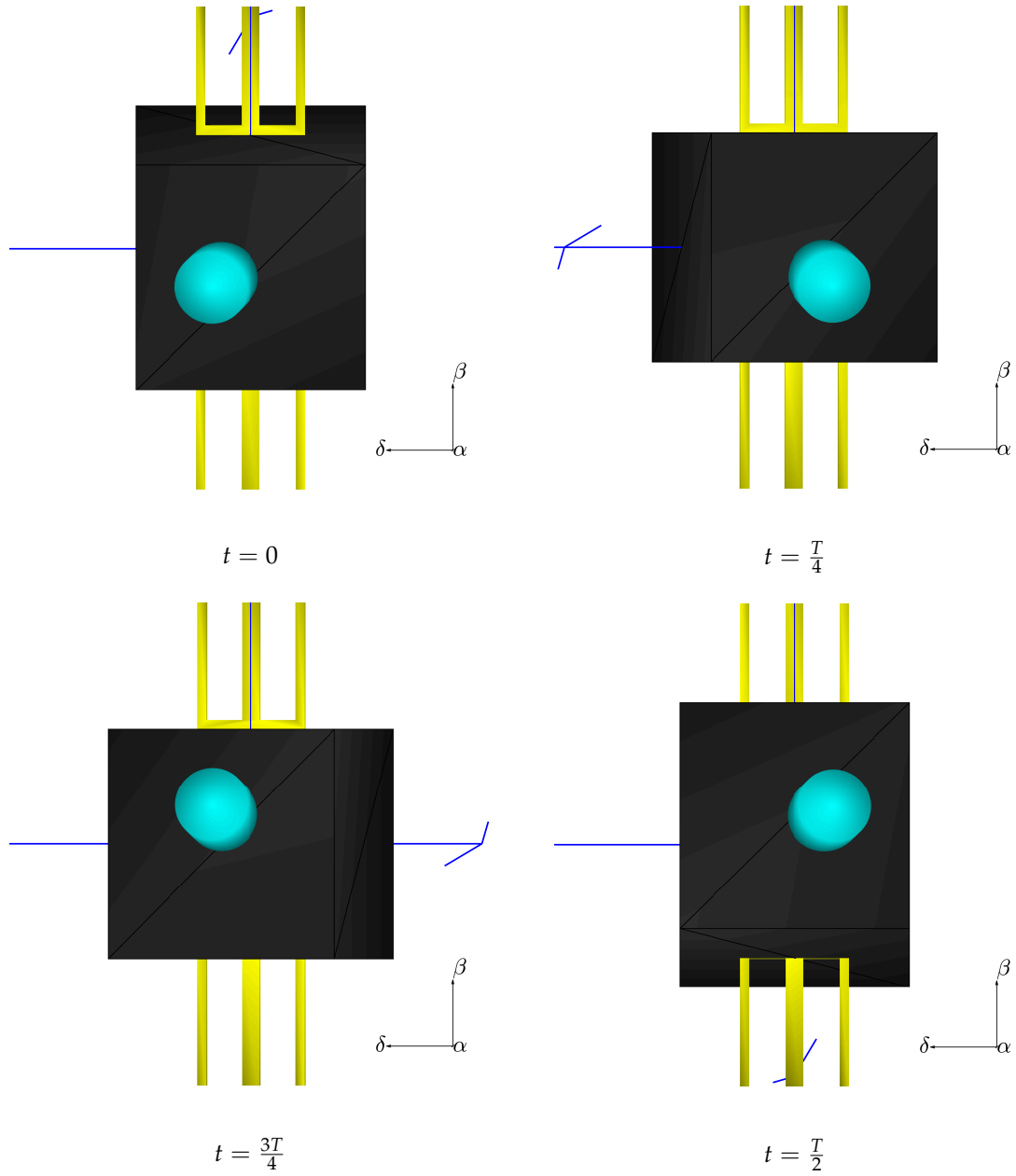
Figure 3.4: Sequence of the BETA trajectory along one period. The image should be read in a clockwise direction

h_x and h_y can be noticed.
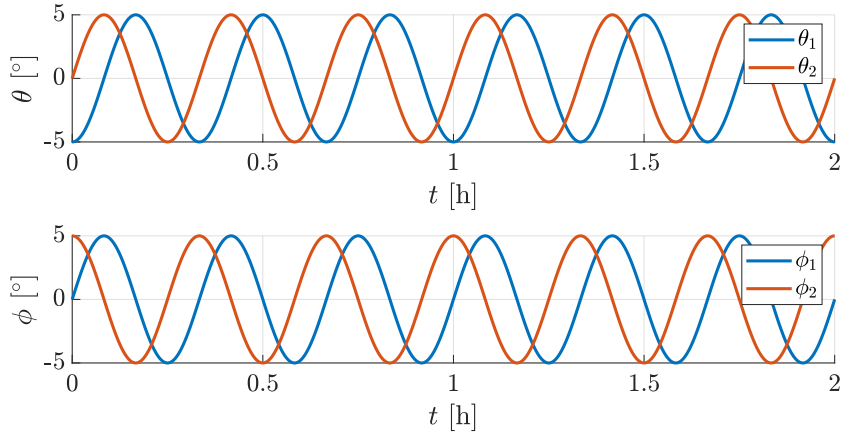
Figure 3.5: Gimbal and attitude angles during the BETA strategy
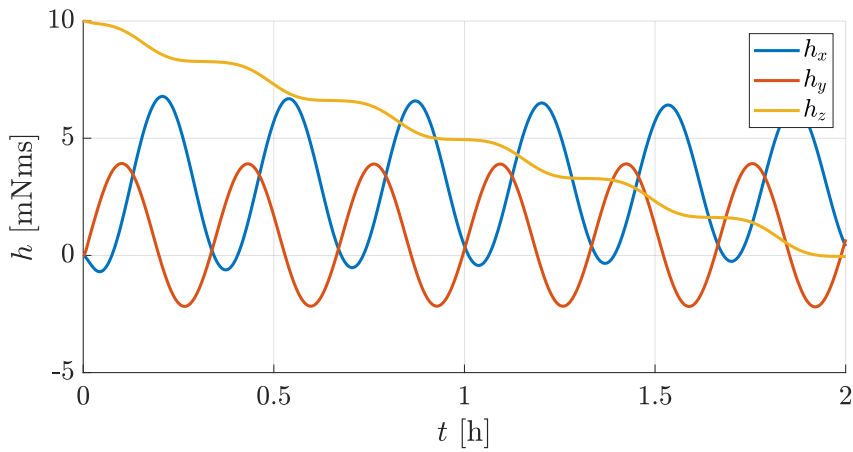
Figure 3.6: De-saturation of the z-axis employing the BETA strategy

By employing a suitable combination of the afore-mentioned strategies all the axes could be theoretically off-loaded without interruptions of the operations and mildly affecting the trajectory. This will be demonstrated in *section 5.2*, where simulations of a full WOL will be carried out in a cruising scenario.

3.4 Coasting Strategies

As previously stated, the coasting strategies exploit the SRP to generate de-saturation torques. Due to the inherent lightness of this disturbance, the WOL could take a much longer time with respect to the previous techniques. These strategies should be then considered as a last resource, accounting also for the fact that a tilt of the SA means a reduction of the generated power because of the increase of the Sun Aspect Angle (SAA), the angle between the normal of a SA and the Sun direction. Another possible scenario could be the failure of the gimbal mechanism, or a mission that does not actually involve a thruster nor momentum-management devices. In both cases, these strategies can be used to effectively perform the WOL.

To accomplish the goal, a tilting mechanism for the SAS is required. The SADM is in charge of maintaining them always in face of the Sun. The overall tilt angle will be therefore the sum of two contributions, the offset angle $\Delta_\odot$ and the relative tilting angle Δ_{rel}. The former can be directly computed from the Sun direction components in the pointing frame axes, since $\hat{S}_p$ is perpendicular to the β-axis. The latter will be imposed according to the WOL strategy. The overall tilting angles of the two SAS can be therefore computed using (3.10). The dynamics of the SADM will be neglected because as it will be shown, the tilting commands will be always smooth and slow.

$$\Delta_1 = \Delta_\odot + \Delta_{rel_1}$$
$$\Delta_2 = \Delta_\odot + \Delta_{rel_2}$$
$$\Delta_\odot = \arctan\left(\frac{S_\delta}{S_\alpha}\right)$$

(3.10)
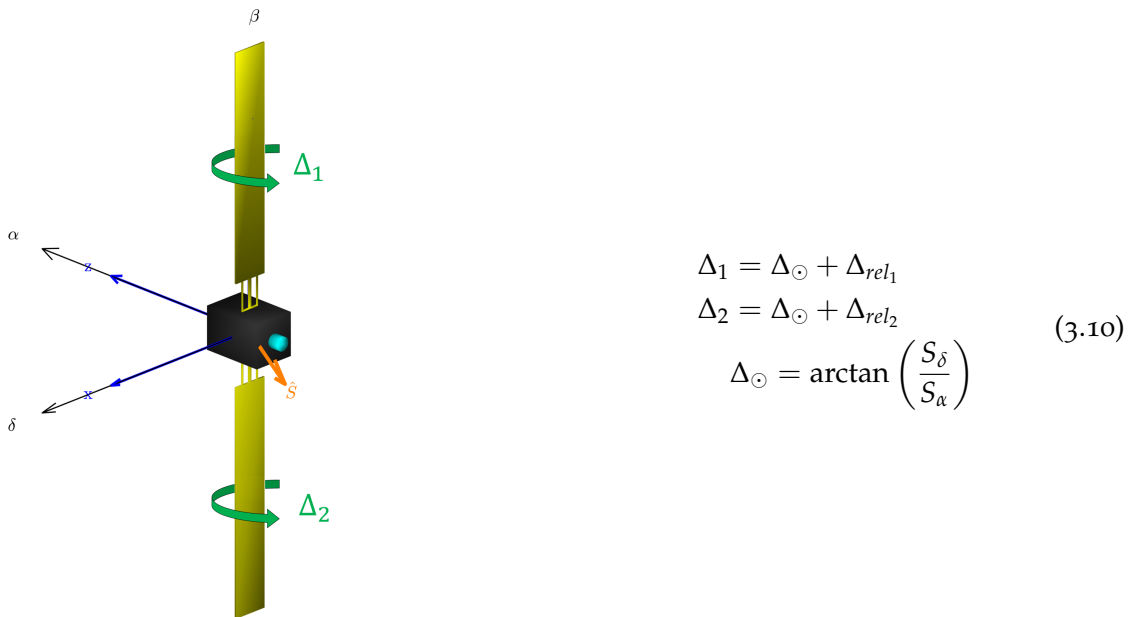
As it has been done in the cruising strategies, also in this case when an attitude motion is required, the orientation of the body with respect to the pointing frame can be linked to the attitude angles ϕ_1 and ϕ_2, as depicted in (3.11). However, in this case, they will
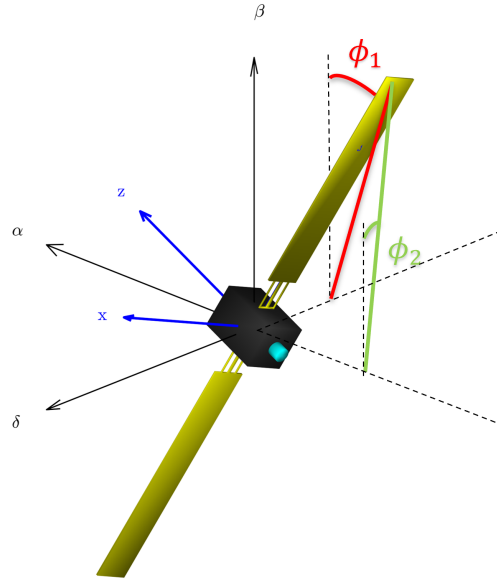
$$A_{b/p} = \begin{bmatrix} \cos\phi_2 & \sin\phi_2 & 0 \\ -\sin\phi_2 & \sqrt{1-(\sin\phi_1)^2-(\sin\phi_2)^2} & -\sin\phi_1 \\ 0 & \sin\phi_1 & \cos\phi_1 \end{bmatrix} \tag{3.11}$$

represent the slewing around the δ-axis and α-axis respectively. This is explained by the fact that in this case the *singular* axis, i.e. the axis that can not be de-saturated keeping a fixed attitude, is β.

3.4.1 Single Solar Array & PinWheel

The Single Solar Array (ssa) and PinWheel (pw) strategies are treated together in this section because they must be combined one consequently to the other to successfully perform a wol without spurious momentum components. As previously stated, when the attitude is fixed, it is possible to generate torques thanks to sa tilting only about axes perpendicular to β. In particular, two types of effects can be accomplished:

- For the ssa strategy, an entire solar wing is kept in shadow such to have a net force on the other one, producing a torque T_{SSA} aligned with $\beta \times \hat{S}$.

- For the pw strategy, the two wings are tilted one with respect to the other of $70°$, just like a pinwheel, in order to produce a torque T_{PW} aligned with $\hat{S}$.

The required combinations of tilting angles to accomplish these torques are reported in *Table 3.1*.

Strategy	SSA_1	SSA_2	PW_1	PW_2
Δ_{rel_1}	$0°$	$90°$	$-35°$	$+35°$
Δ_{rel_2}	$90°$	$0°$	$+35°$	$-35°$
T	$-T_{SSA}$	$+T_{SSA}$	$-T_{PW}$	$+T_{PW}$

Table 3.1: Combinations of the relative tilting angles for the ssa and pw strategies

While the choice of $90°$ in ssa is straightforward, the value of $35°$ for pw comes from the fact that the srp torque is the highest at that angle, as it can be seen in *Figure 3.7*.
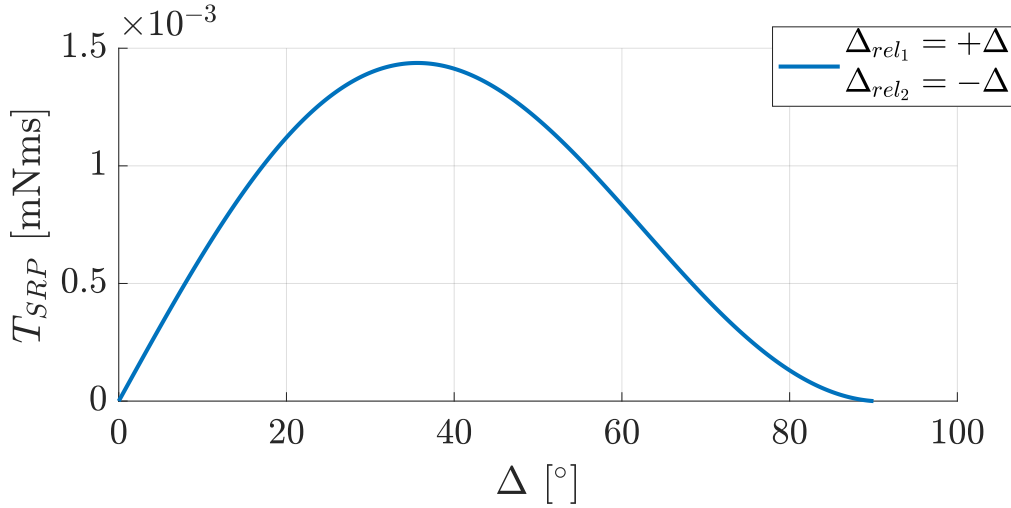
Figure 3.7: srp torque generated with relative tilting angles of the same absolute value but with opposite sign

The torques will be distributed along the x and z axes depending on the Sun direction. Moreover, the effect of these torques on the rws momentum components will be to increase or decrease them according to their initial sign. In general, all 4 signs permutations can be covered in order to have always both h_x and h_z approaching zero. In *Figure 3.8* and *Figure 3.9*, all the cases are reported with the correspondent effect on the stored angular momentum.

The Sun direction, indicated with an orange arrow in the previous figures, has been considered fixed up to now. In order to seek for a general solution, a *truth table* has been realized to choose the correct sa configuration according to the 4 variables of interest, the signs of h_x and h_z and the signs of S_δ and S_α. By entering *Table 3.2* with these conditions,

$$h_0 = \begin{bmatrix} -5 & 0 & -10 \end{bmatrix} \text{ mNms} \rightarrow SSA_1$$

$$h_0 = \begin{bmatrix} 5 & 0 & 10 \end{bmatrix} \text{ mNms} \rightarrow SSA_2$$
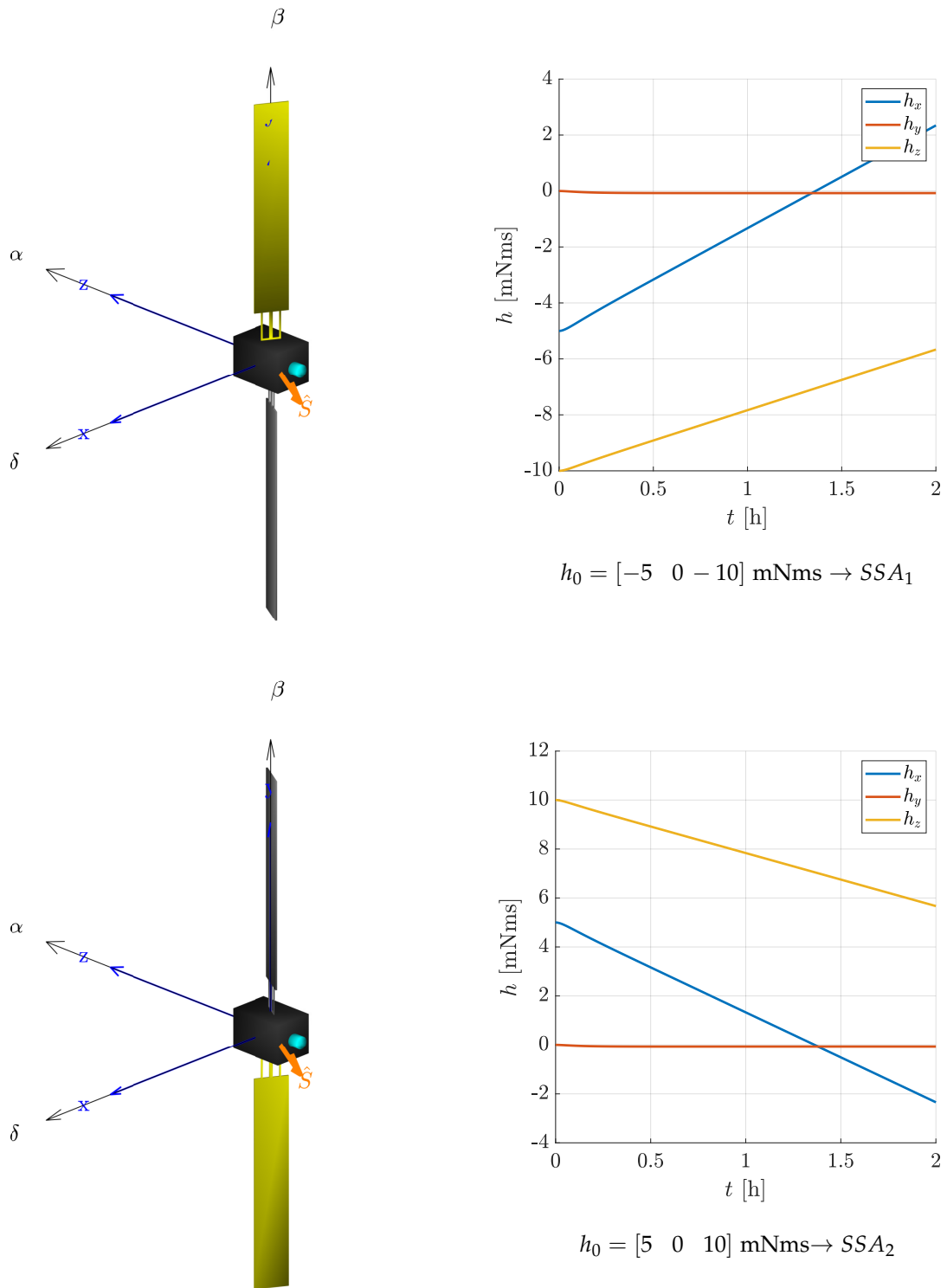
Figure 3.8: Single Solar Array Strategies

41

$h_0 = \begin{bmatrix} 5 & 0 & -10 \end{bmatrix}$ mNms $\rightarrow PW_1$

$h_0 = \begin{bmatrix} -5 & 0 & 10 \end{bmatrix}$ mNms $\rightarrow PW_2$
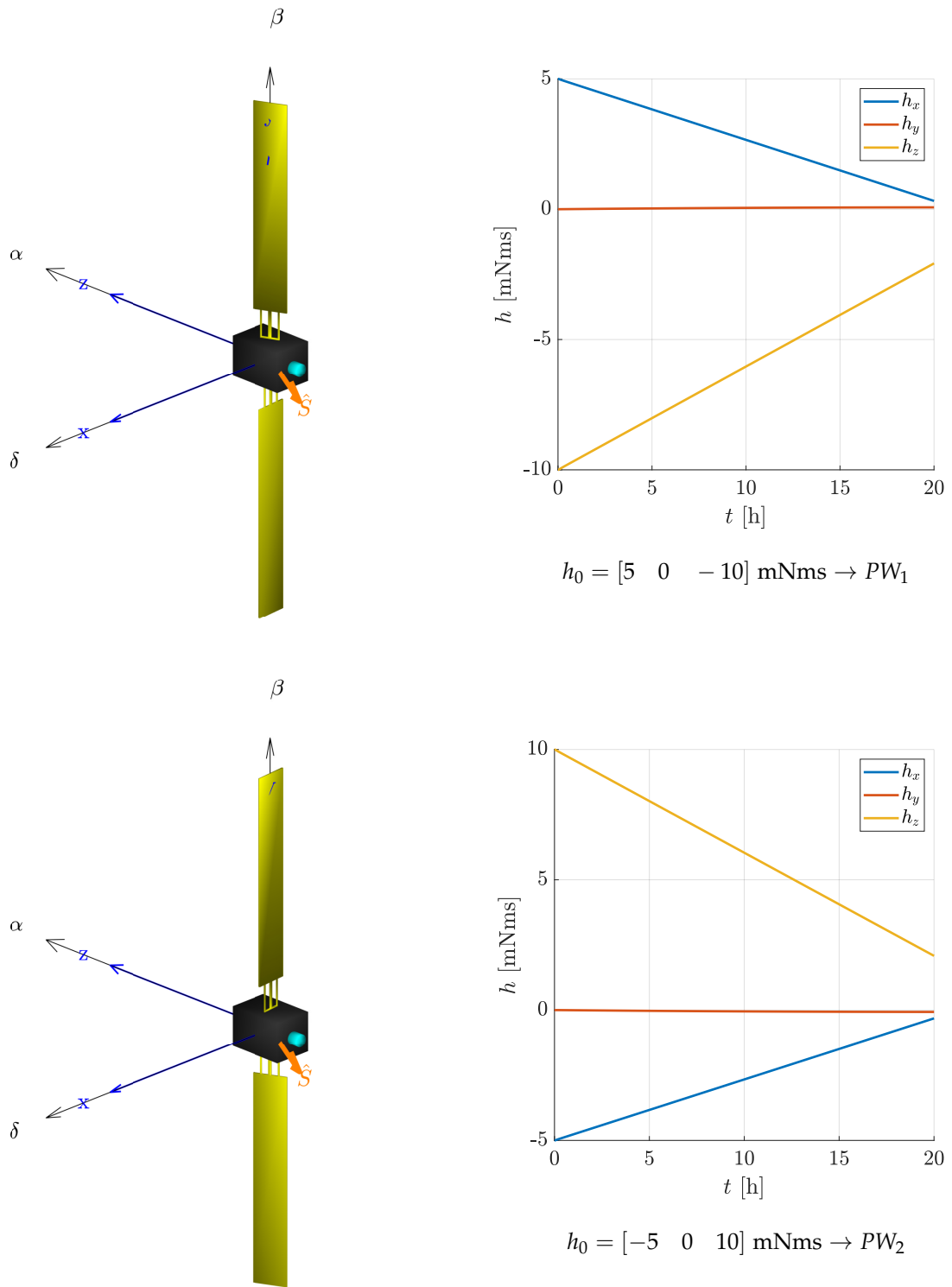
Figure 3.9: PinWheel Strategies

a total of 16 combinations is obtained and to each of the 4 of them, the right strategy is linked.

$S_\delta > 0$	T	T	F	F	T	T	F	F	T	T	F	F	T	T	F	F
$S_\alpha > 0$	T	F	T	F	T	F	T	F	T	F	T	F	T	F	T	F
$h_x > 0$	F	F	T	F	T	T	F	T	F	T	F	T	T	F	T	F
$h_z > 0$	T	F	T	T	F	T	F	F	F	F	T	T	T	T	F	F
Strategy	SSA_1				SSA_2				PW_1				PW_2			

Table 3.2: Truth table for the choice of ssa and pw strategies

Thanks to this, both h_x and h_z are guaranteed to approach zero in any situation. However, in this case, the difficulty is to make them reach zero at the same time, to avoid residual momentum. To this aim, as mentioned at the beginning of the section, a coupling of pw and ssa is employed. Intuitively, this could be a solution since the main difference between the two strategies is that in one case the momentum slopes are of the same sign, in the other case they have opposite signs. This means that after the zero crossing of either h_x or h_z, after a certain time delay Δt the configuration can be changed in such a way to have both of them reach zero at the same time. The task becomes therefore the computation of this time delay, and in particular the question to be answered is:

> *"If either h_x or h_z crosses the zero line at t_0, Which is the time delay $\Delta_t = t_1 - t_0$ after which the configuration should be changed to dump them at the same time?"*

The torques can be set equal to the ratios of momentum differences over time differences since they are constant for a fixed configuration. The problem in (3.12) can be stated.

By re-arranging the first two equations and applying the final conditions in the third one, the system can be simplified to a single equation where the delay time is computed from the angular momentum values at t_0, as shown in (3.13). The torques are assumed to be estimated on-board prior to the wol maneuver, using the same srp model used for the simulations in this work. In this way, the computer just needs to record the value of the angular momentum that has not crossed zero and apply the reported formula. The same equation can be used also in case the pw is performed first, by just exchanging T_{PW} with T_{SSA}. After the time delay, the truth table is applied again with the updated sign values of the momentum components and the wol is completed.
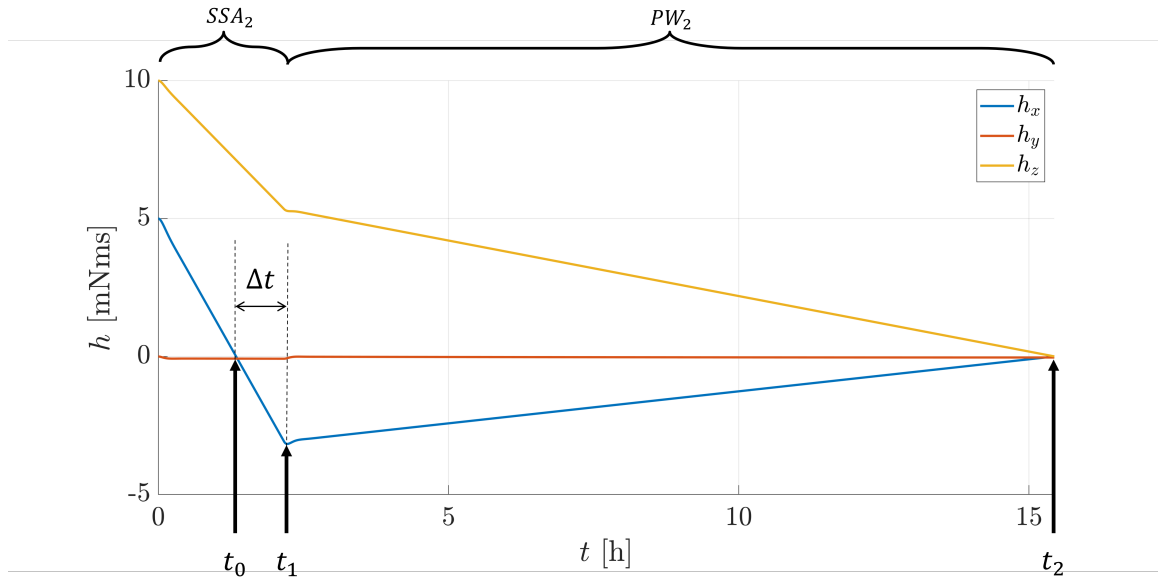
$$\begin{cases} T_{SSA_x} = \dfrac{h_{x_1} - h_{x_0}}{\Delta t} \\[2mm] T_{SSA_z} = \dfrac{h_{z_1} - h_{z_0}}{\Delta t} \\[2mm] T_{PW_x} = \dfrac{h_{x_2} - h_{x_1}}{t_2 - t_1} \\[2mm] T_{PW_z} = \dfrac{h_{z_2} - h_{z_1}}{t_2 - t_1} \end{cases} \qquad \begin{aligned} &\text{find} \quad \Delta t \\ &\text{s.t.} \quad h_{x_2} = h_{z_2} = 0 \end{aligned} \qquad (3.12)$$

$$\begin{cases} h_{x_1} = T_{SSA_x}\Delta t + h_{x_0} \\ h_{z_1} = T_{SSA_z}\Delta t + h_{z_0} \\ \dfrac{T_{PW_x}}{T_{PW_z}} = \dfrac{h_{x_1}}{h_{z_1}} \end{cases} \quad \rightarrow \quad \frac{T_{PW_x}}{T_{PW_z}} = \frac{T_{SSA_x}\Delta t + h_{x_0}}{T_{SSA_z}\Delta t + h_{z_0}} \tag{3.13}$$

$$\Delta t = \frac{h_{x_0} T_{FW_z} - h_{z_0} T_{FW_x}}{T_{SSP_z} T_{FW_x} - T_{SSP_x} T_{FW_z}}$$

3.4.2 SRP Wading

Also during coasting, a full WOL can not be completed employing strategies that are based only on a fixed attitude, because there is no possibility to produce torques about the y-axis since the SA faces never face this direction. Therefore, the last question to be answered is:

> *"Which are the guidance laws of Δ_{rel_1}, Δ_{rel_2}, ϕ_1 and ϕ_2 required to dump h_y, without ending with spurious momentum on the other axes?"*

To desaturate this axis, the property of conservation of momentum in a fixed frame can be exploited again. In particular, by coupling a specific SADM trajectory with an attitude motion, torques about the β-axis can be produced, which will eventually dump the momentum on y.

The sequence is shown in *Figure 3.10*, while the guidance laws are reported in (3.14). The imposed attitude motion is circular with a period equal to T, while the imposed SA trajectory is still circular but shifted of 90° in amplitude and of $\Delta_\odot$ in phase. The two consequences are that the face that should point the Sun is kept close to $\Delta_{rel} = 0°$ for a reasonable fraction of time, and this time slot is consistent with the Sun direction. Moreover, every half period the amplitude of one SA is capped to 90° while the second one follows the nominal trajectory. In this way, the Sun provides a force only to one SA at a time and since this force is always offset from the β-axis on the same "side", a periodic torque about that axis is generated. From an external observer, the CubeSat seems to "wade" against the Solar wind, and therefore this strategy has been called Solar Radiation Pressure Wading (SRPW).

The SRPW trajectory is characterized by the same tunable parameters of the BETA trajectory: the maximum attitude angle ϕ_{max} and the period of the circular motions T. Also their

$t = 0$

$t = \frac{T}{4}$

$t = \frac{3T}{4}$

$t = \frac{T}{2}$
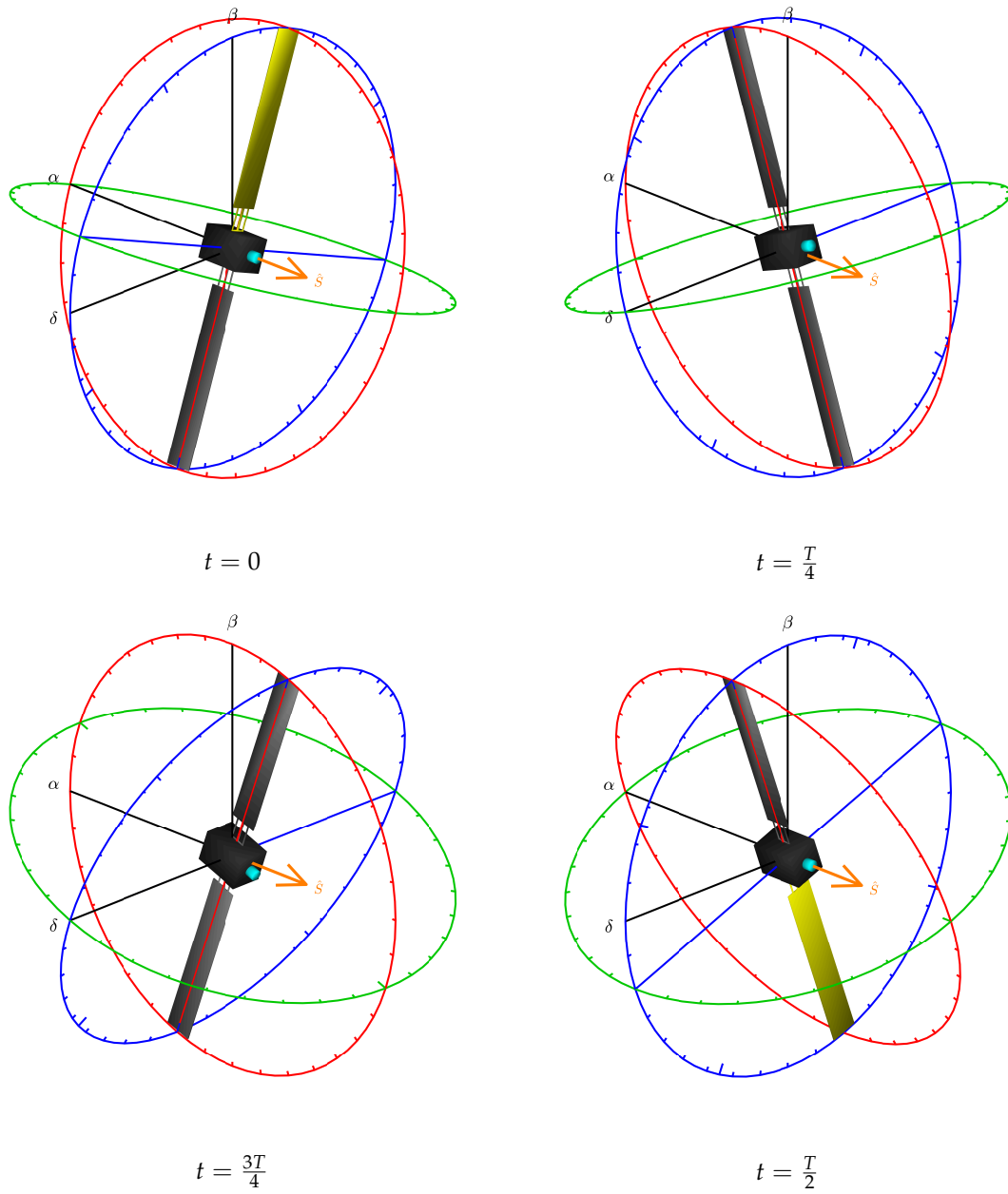
Figure 3.10: Sequence of the SRPW trajectory along one period. The image should be read in a clockwise direction
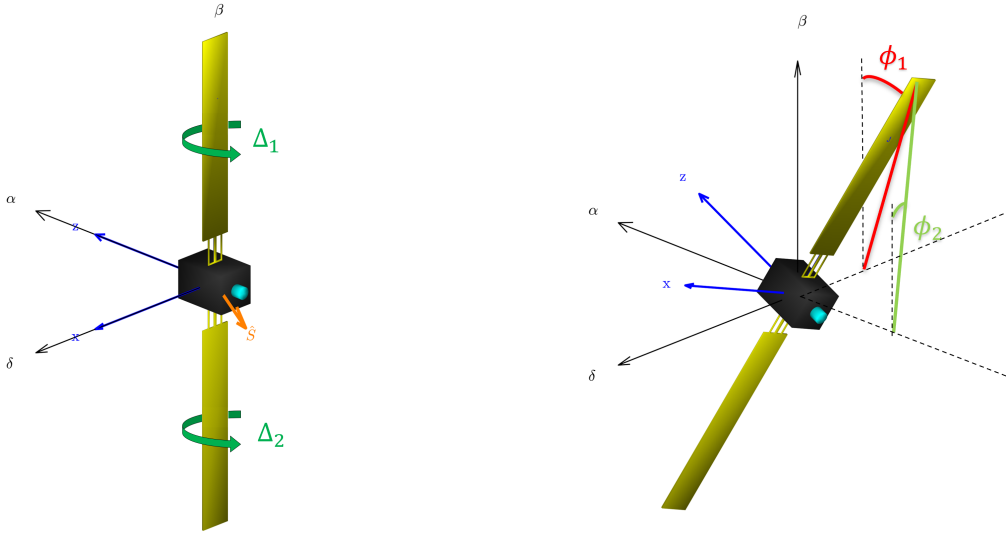
$$\phi_1 = \phi_{max}\sin(\omega t)$$
$$\phi_2 = \phi_{max}\cos(\omega t)$$

$$\Delta_{rel_1} = 90° \min\left(1, 1 + \cos\left(\omega t + \Delta_\odot\right)\right)$$
$$\Delta_{rel_2} = 90° \min\left(1, 1 - \cos\left(\omega t + \Delta_\odot\right)\right)$$

(3.14)

$$\omega = 2\pi f = \frac{2\pi}{T}$$

effects on the WOL will be the same, but in this case the oscillations will be on h_x and h_z. A good compromise has been found with $\phi_{max} = 20°$ and $T = 2\,\text{h}$.

Using these values, the imposed guidance laws for the relative tilting angles and the attitude angles are reported in *Figure 3.11*, while the expected angular momentum trend for an initial condition of $h = \begin{bmatrix} 0 & 10 & 0 \end{bmatrix}$ mNms is shown in *Figure 3.12*. When the momentum stored has a negative sign, the guidance laws of the relative tilting angles are simply exchanged in order to produce a torque of the opposite sign.

The coasting strategies just presented can be employed one consequent to the other to dump the momentum stored in all the axes, without consumption of propellant but with reductions in the power production. This will be demonstrated in *section 5.3*, where simulations of a full WOL in a coasting scenario will be carried out.
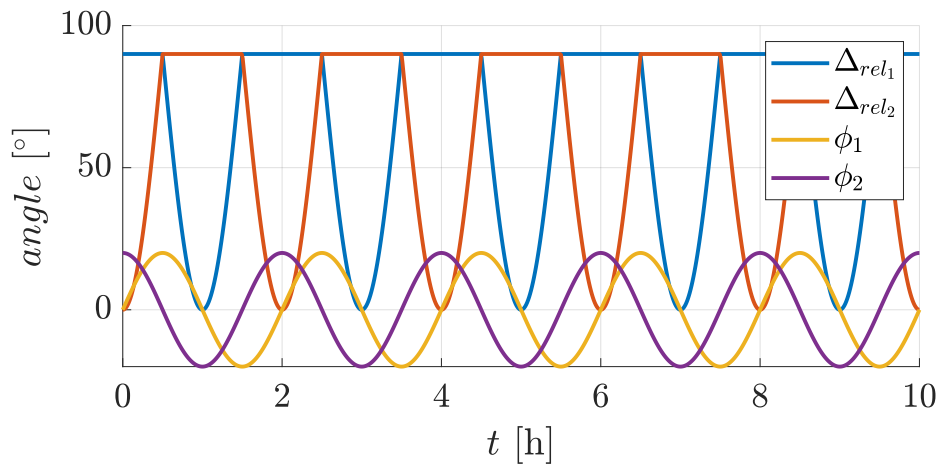
Figure 3.11: Relative tilting and attitude angles during the srpw strategy
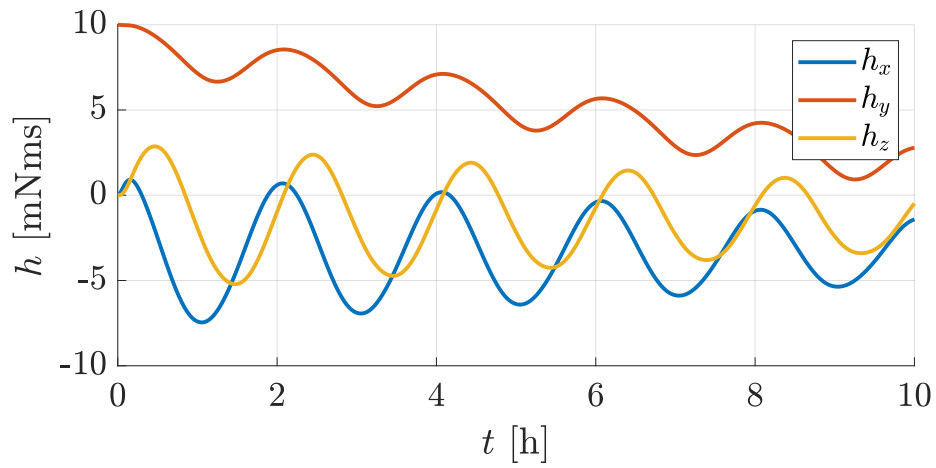
Figure 3.12: De-saturation of the y-axis employing the srpw strategy

3.5 Pyramid Configuration

An important aspect to consider is that up to now the strategies have been presented with a set of 3 RWs, aligned with the body axes. This is not in general true, and it is especially not true in the case of M-Argo, where the wheels are accommodated in a pyramid configuration.

The solution comes again from the principle of conservation of momentum. Since the momentum is conserved inertially, all the WOL strategies can be still used. However, as momentum to dump, they will consider an *equivalent* momentum, that is just the projection of the actual RWs momentum on the body axis. Therefore, the 4 RWs problem is re-written as a 3 RWs case, using the configuration matrix presented in *subsection 1.3.1*.

3.5.1 WOL Singularity

When more than 3 wheels are employed, a *singularity* can occur. If the WOL strategies manage to dump the equivalent momentum, this does not imply that also the momentum stored in RWs is zero. In fact, looking at the example in (3.15), it is clear that the equivalent momentum associated with h_{eq} is zero, even if the "real" momentum is not.

$$h_{eq} = R\, h_{RW} = \frac{1}{\sqrt{3}} \begin{bmatrix} -1 & -1 & -1 & -1 \\ 1 & -1 & 1 & -1 \\ 1 & 1 & -1 & -1 \end{bmatrix} \begin{bmatrix} 4 \\ -4 \\ -4 \\ 4 \end{bmatrix} = \begin{bmatrix} 0 \\ 0 \\ 0 \end{bmatrix} \tag{3.15}$$

In general, if the momentum absolute value is the same on each RW, for each R there is a combination of signs that leads to this singularity. For a pyramid configuration oriented along $-x$ as in the example, the combination of signs is $[+\ -\ -\ +]$. This means that any momentum $h = [k\ -k\ -k\ k]$ can not be off-loaded with the strategies presented so far, because the "sensed" momentum will always be zero.

In this case, to complete the de-saturation, a specific command should be sent to the RW in such a way to decrease their speed and at the same time not produce any torque on the s/c. In particular, the derivative of the momentum in each wheel should be opposite to its sign, as shown in (3.16).

$$\dot{h}_{RW} = -\operatorname{sgn}(h_{RW}) \tag{3.16}$$

In theory, to obtain the required commanded torque to do so, the dynamics should be

inverted. However, (3.17) clearly show that this operation results in a null command.

$$\dot{h}_{RW} = -R^{\star}(T_{com} + \omega \times Rh_{RW}) \equiv -\text{sgn}(h_{RW})$$

$$T_{com} = \underbrace{R\,\text{sgn}\,(h_{RW})}_{0} - \omega \times \underbrace{(Rh_{RW})}_{0} = 0 \tag{3.17}$$

This means that when such a singularity is detected, the commanded torque should be by-passed and each wheel speed should be decreased directly reducing its rotor spin rate with a proper gain, as shown in (3.18).

$$\dot{\omega}_{RW_i} = -\left(\frac{k}{J_{RW_i}}\right)\text{sgn}(h_{RW_i})$$

$$\quad \text{for } i = 1, ..., N_{RW} \tag{3.18}$$

$$\dot{h}_{RW_i} = J_{RW_i}\,\dot{\omega}_{RW_i} = -k\,\text{sgn}(h_{RW_i})$$

The resulting effect on the momentum is reported in *Figure 3.13*. Considering a wol during cruising and an initial momentum of $h_0 = [7 \quad -4 \quad -5 \quad 8]$, the plots show that a null equivalent momentum does not mean that the momentum stored in the rws is zero. At about $t = 0.06$ h the equivalent momentum is dumped but the actual stored momentum in the 4 rws is still high, around $h = 12$ mNms. At that point the commanded torque is by-passed and the wheels rate is forcefully decreased, completing the wol. During this last phase, according again to (3.17), a null torque is produced on the s/c and the attitude is therefore kept almost fixed.
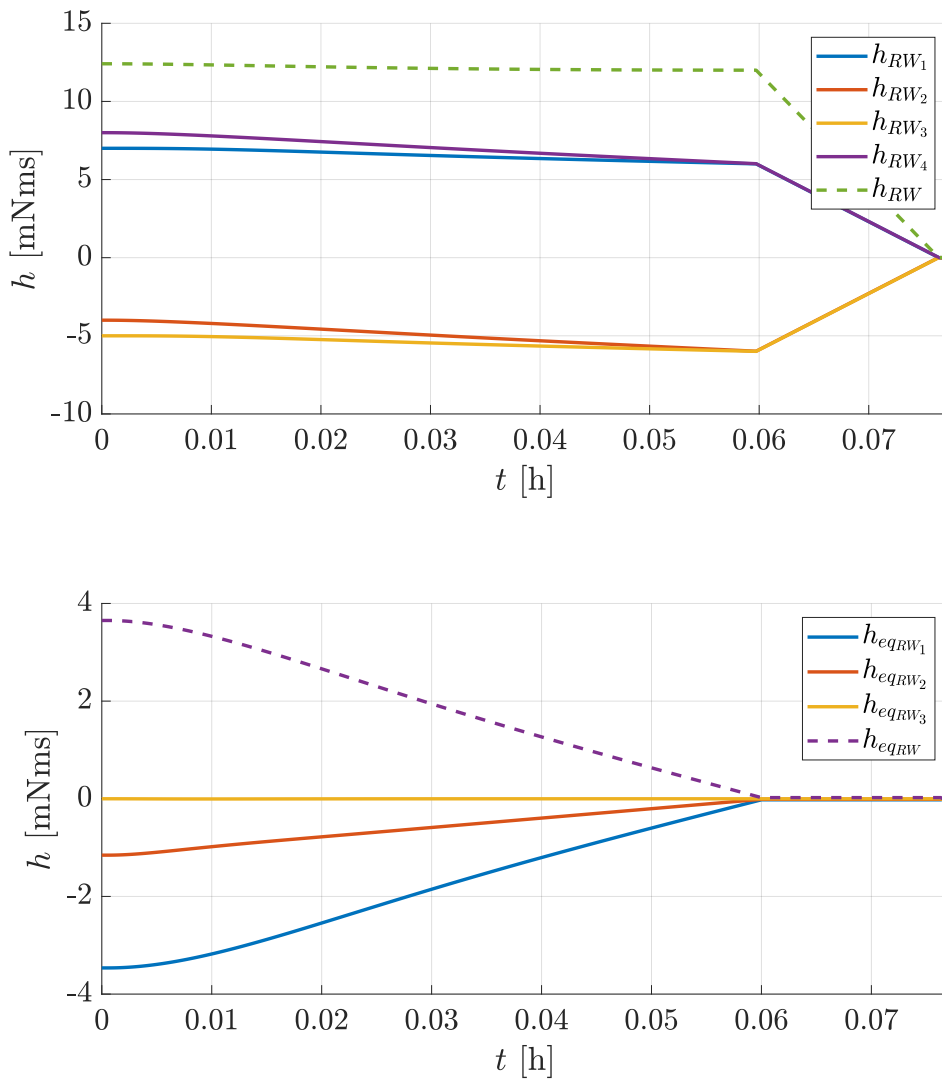
Figure 3.13: WOL singularity in a 4 RWS assembly during a cruising scenario

3.6 Autonomous WOL

The last section of this chapter addresses the problem of linking all the techniques previously presented in an autonomous procedure. The final model should be able to recognize the angular momentum levels and behave accordingly, choosing the correct strategies to perform a full wol on the entire rw assembly.

To accomplish this, it is convenient to exploit a State Machine (sm) where macro-states identify the different scenarios and each state represents a different wol strategy. The gimballed thrust and beta trajectory strategies will be then grouped into the cruising macro-state, while the ssa/pw and srpw strategies will be grouped into the coasting macro-state.

However, before proceeding, it is important to identify the trigger conditions that rule this autonomous process.

3.6.1 Trigger Conditions

The conditions for the transition from one state to the other are defined by the triggers reported in *Table 3.3*.

Flag	Meaning when true/false
Fixed type	
wol	wol/no wol scenario
cruising	Cruising/coasting scenario
Dynamic type	
wol_completed	wol finished/not finished
thrust	Thruster switched on/off
counter(1)	$h_{eq_x} = 0$
counter(2)	$h_{eq_y} = 0$
counter(3)	$h_{eq_z} = 0$
counter(4)	$h_{eq_y} - h_{eq_z} = 0$
counter(5)	$h_{eq_x} - h_{eq_z} = 0$
counter(6)	$h_{eq_x} - h_{eq_y} = 0$

State	ID
RE-POINTING	-1
GIMBAL/SSA/PW	0
BETA	1
SRPW	2
WOL SINGULARITY	3
DE-TUMBLING	4
NO WOL	5

Variable	Condition
$\boldsymbol{h}_{RW}$	$\|\boldsymbol{h}_{RW}\| < \bar{h}_{end}$
$\boldsymbol{h}_{eq_{RW}}$	$\|\boldsymbol{h}_{eq_{RW}}\| < \bar{h}$
$\boldsymbol{\epsilon}$	$\|\boldsymbol{\epsilon}_{point}\| < \bar{\epsilon}$

Table 3.3: Flags, states and variables used in the sm

In general, they derive from three entities:

- **Flags**. Flags are Boolean variables that can be fixed if they enter the simulation as constant parameters, or dynamics if they change during it. For instance, the type of scenario is an input constant parameter, while the zero-crossing of the momentum components occurs once in a while.

- **States**. States are identified by integer numbers. Some transitions can be prevented according to the current state.

- **Variables**. The variables of interest are the momentum components, that dictate the choice of one strategy with respect to another. In particular, the norm of the equivalent momentum and of the actual momentum are evaluated and compared to specific thresholds. Moreover, also the pointing error is used as a trigger condition to exit from re-pointing or de-tumbling states.

3.6.2 State Machine

Stateflow has been used to construct the transition diagrams, flow charts and truth tables, because the resulting sm can be subsequently linked to the MATLAB algorithms and Simulink models that will be presented in *chapter 4* [51].

The sm architecture is presented in *Figure 3.14*. A hierarchical decomposition will now be carried out, where different labels will be used for (macro-state) and (states).

- (START) This is the initial macro-state, that is immediately exited according to the scenario under consideration.

- (CRUISING) This macro-state, sketched in *Figure 3.15*, is entered from START if the cruising scenario is selected. The WOL is performed while thrusting, interchanging between two inner states:
  - ○ (GIMBAL) This state exploits the strategies based on the gimballed thruster presented in *subsection 3.3.1*. It is the entry and exit state for the CRUISING macro-state.

  - ○ (BETA) This state exploits the BETA trajectory presented in *subsection 3.3.2*. It is entered from GIMBAL if h_{eq_z} crosses zero, and return to the same state if h_{eq_x} crosses h_{eq_y}.

Figure 3.14: State Machine
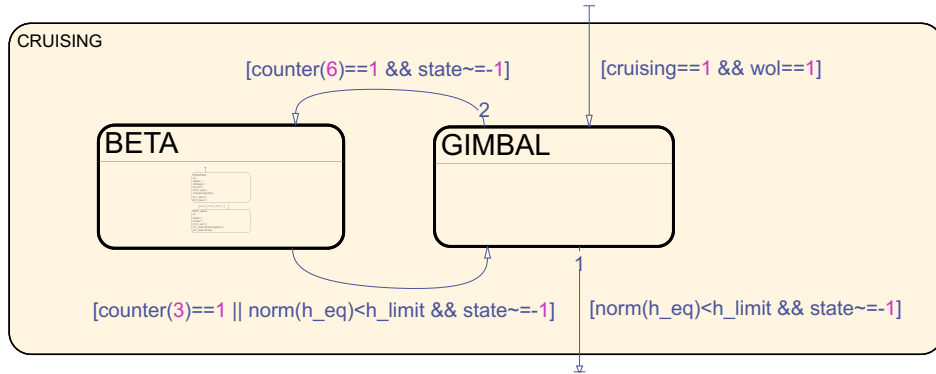
Figure 3.15: Cruising macro-state

- **COASTING** This macro-state, sketched in *Figure 3.16*, is entered if the coasting scenario is selected. The WOL is performed without thrusting, interchanging between two inner states:

    ○ **SSA/PW** This state exploits the strategies based on the SA tilting presented in *subsection 3.4.1*. It is the entry and exit state for the the COASTING macro-state.

    ○ **SRPW** This state exploits the SRPW trajectory presented in *subsection 3.4.2*. It is entered from SSA/PW if h_{eq_x} crosses h_{eq_z} and return to the same state if h_{eq_y} crosses zero.
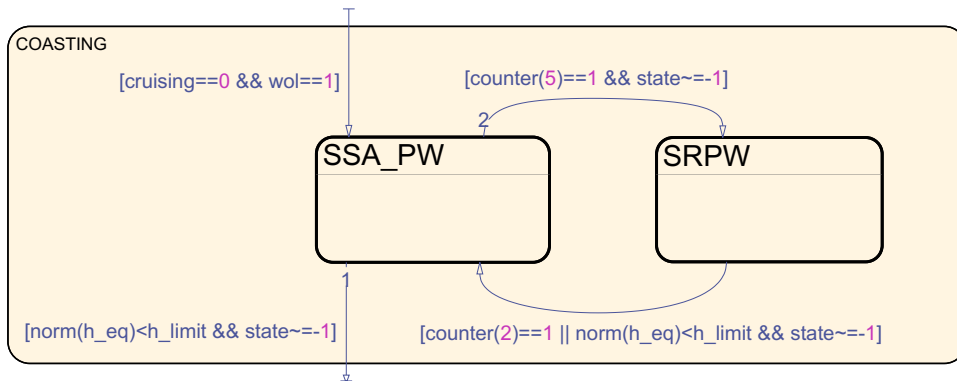
Figure 3.16: Coasting macro-state

- **END** This macro-state is entered from any other one when the equivalent momentum norm is under a specific threshold. The thruster is switched off till the exit of this macro-state. Its architecture is sketched in *Figure 3.17*. Three inner states are present:

    ○ **WOL SINGULARITY** This state completes the WOL in the case of a 4 RWS assembly,

as explained in *subsection 3.5.1*. It is the entry state for the END macro-state and its exit condition is on the norm of the actual momentum.

○ (DE-TUMBLING) This state is entered from WOL SINGULARITY and imposes the de-tumbling of the platform to bring the body frame coincident with the pointing frame before the end of the WOL. In fact, a drifting of the attitude could have been occurred during WOL SINGULARITY, where the nominal control is by-passed.

○ (WOL END) This state is entered from DE-TUMBLING as soon as the pointing error decreases under a specific threshold. It is the exit state for the END macro-state.
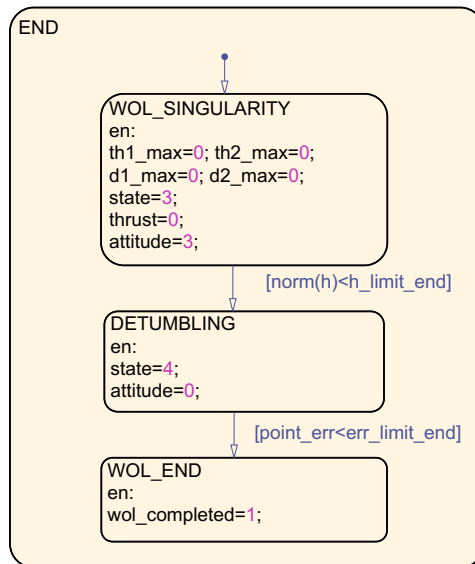
Figure 3.17: End macro-state

• (NO WOL) This macro-state is entered from START if the trajectory without WOL is required, or from END if the WOL has been completed. In this state the body frame coincides with the pointing frame and the thrust follows the reference profile.

Some important aspects characterizes the general SM behaviour:

• The first strategy to be used, regardless of the scenario, is a fixed-attitude one. This choice allows removing firstly the momentum on "non-singular" axes. In this way,

when the following strategy will start, the oscillations on the momentum components will have a mean value of zero. In fact, an offset on these momentum oscillations could cause saturation on axes that are not being off-loaded.

- The last strategy to be used, regardless of the scenario, is a fixed-attitude one. In fact, after completing BETA or SRPW, the reset of the orientation to the pointing frame requires the RWS to store a little amount of momentum, that has to be eventually off-loaded again with fixed-attitude strategies.

- Any strategy state has two inner micro-states. The first one is a re-pointing state and the second one is related to the actual WOL strategy. The moment the re-pointing state is entered, the guidance law changes to the new one in a discontinuous manner, and the pointing error must be reduced before starting the WOL. For this reason, the excursion angles of the gimbal and the SAS are set to zero and the thrust flag too. Moreover, any transition to another state is prevented when the current state is re-pointing (-1). This precaution is used to avoid fast and unexpected consecutive transitions between two states. In fact, during a re-pointing maneuver, the momentum could change in such a way as to trigger the counters and change strategy.

- The zero-crossing of momentum differences is used as exit condition for the strategies that dump two momentum components at the same time. This choice has been considered more versatile than just evaluating the norm of them and checking if it is lower than a threshold. In this way, there is the assurance that the state will be exited even if the algorithms fail the dumping because one momentum will surely cross the other, sooner or later.

The SM just presented will manage the full WOL in any scenario, allowing for smooth transitions between the different strategies in the simulations that will be carried out in *chapter 5*.

4

Astrodynamics Simulator

T-HE algorithms and the decision-making logic must be demonstrated through the development of an *astrodynamics simulator*. To this aim, Simulink has been selected as programming environment. This MATLAB-based software is widely used for modeling, simulating and tuning automatic control systems [52].

The simulator structure, shown in *Figure 4.1*, is separated in two main parts. The first one is related to the real world, where the dynamics and kinematics are propagated and the physical sensors and actuators work, while the second one is related to the virtual processes run by the software, that receives information from the sensors and is in charge of processing them, as well as providing commands to the actuators in order to follow the desired trajectories. The interactions between these functions and the decision-making processes are managed by the On-Board Computer (OBC).

In real life, the blocks on the left are a sort of "black box" for the s/c, because they are a representation of the physical world and associated phenomena. The only way of interfacing with it is by receiving information from sensors and sending commands to the actuators. These two linking points are represented by the buses FromSens and ToAct respectively. The role of the GNC engineer is to design and tune the blocks on the right in such a way to estimate the state from the sensors measurements with the highest accuracy possible (Navigation), provide the correct desired state according to the scenario and the decisions of the SM (Guidance), and finally compute the required actuators commands to cancel the error between the desired state and the estimated one (Control).

Each block will now be analyzed in detail, specifying the input and output signals and its role in the simulation process.
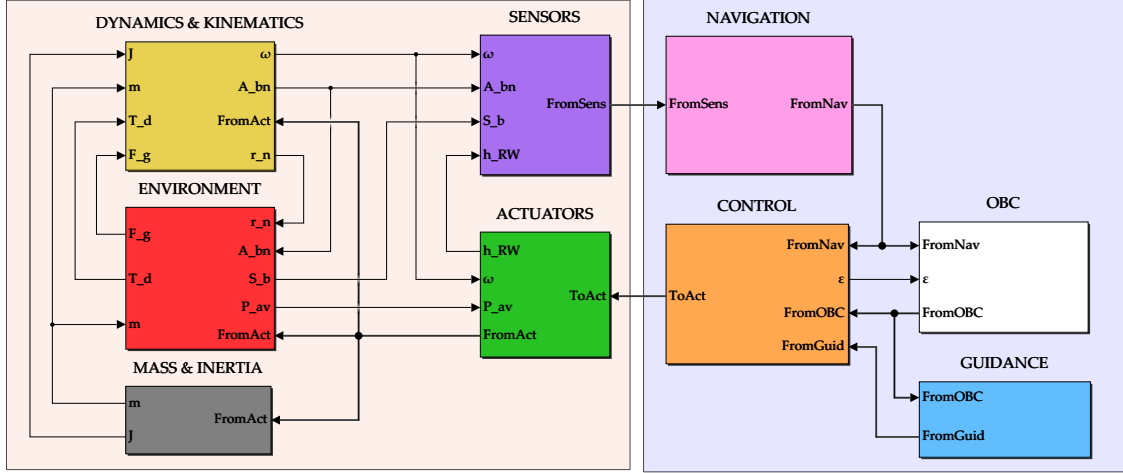
Figure 4.1: Astrodynamics simulator structure

4.1 Dynamics & Kinematics

This block integrates the Equation Of Motion (EOM) in (4.1) to obtain a 6-DOF propagation [53]. Its internal structure is shown in *Figure 4.2*.

$$
\begin{cases}
m\dot{v} = F \\
\dot{r} = v \\
J\dot{\omega} = -[\omega]^{\times}J\omega + T \\
\dot{A} = -[\omega]^{\times}A
\end{cases}
\qquad
[\omega]^{\times} =
\begin{bmatrix}
0 & -\omega_3 & \omega_2 \\
\omega_3 & 0 & -\omega_1 \\
-\omega_2 & \omega_1 & 0
\end{bmatrix}
\tag{4.1}
$$

Regarding the translational dynamics, the inputs are the mass m and the external force F, sum of the gravity force F_g and the thrust F_{thr}. The trajectory is integrated in the inertial frame using Newton's Second Law of Motion. The output is the state of the s/c in terms of position vector r_n.

Regarding the rotational dynamics, the Euler Equations are used and integrated in the body frame. The skew-symmetric matrix of ω can be used as replacement for the cross product operation. The inputs are the inertia J and the external torque T, sum of the thruster torque T_{thr}, the effective RWS control torque T_{eff} and the disturbance torque T_d. The output is the angular rate ω.
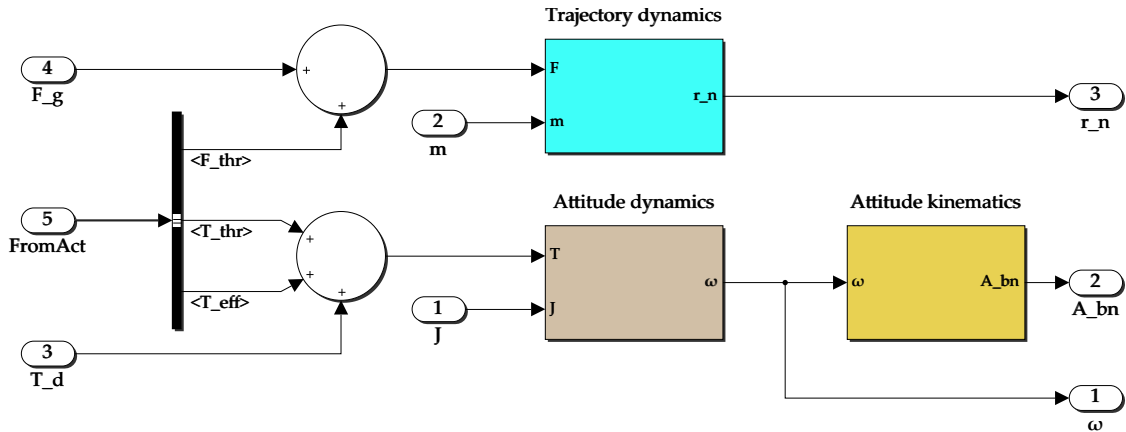
Figure 4.2: Dynamics & Kinematics block

The DCM kinematics is then propagated performing an ortho-normalization of the matrix at each integration step, to preserve the orthogonality [54]. This last formula is reported in (4.2).

$$A' = \left(\frac{3}{2} - \frac{1}{2} A A^T \right) A \tag{4.2}$$

4.2 Mass & Inertia

This block retrieves the mass of the S/C integrating the mass flow rate and computes the analytical inertia tensor at each time step. The inputs are the mass flow rate $\dot{m}$ and the tilting angles Δ_1 and Δ_2, extracted from the FromAct bus.

In most of the cases, the inertia variations are due only to the mass decrease or to changes in mass distribution due to depletion of the propellant tanks. For this reason, J is usually considered a fixed quantity because these variations are very slow in time. However, the high tilting angles that the SP experience during the coasting strategies are expected to cause relevant changes in the distribution of the inertia components. Moreover, M-Argo is characterized by huge solar wings and since the inertia scales with the distance from the COM, these oscillations could result in an even higher amplification. It becomes therefore important to check the robustness of the controller, that is usually tuned with respect to a nominal inertia tensor, with respect to these uncertainties.

The developed analytical model of inertia considers the SP and the main body as separate components, employing as main assumption an homogeneous distribution of mass. In this case, the inertia tensors of plates and cuboids with respect to their COM are well-known

quantities [55]. The ones associated to a cuboid of sides a, b and c and a plate facing x-axis of sides b and c are reported in (4.3).
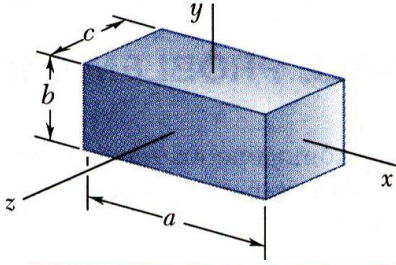
$$J_{cub} = \frac{m}{12} \begin{bmatrix} b^2 + c^2 & 0 & 0 \\ 0 & a^2 + c^2 & 0 \\ 0 & 0 & a^2 + b^2 \end{bmatrix}$$

(4.3)
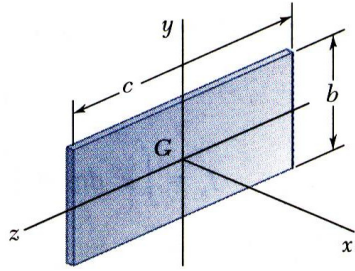
$$J_{plate} = \frac{m}{12} \begin{bmatrix} b^2 + c^2 & 0 & 0 \\ 0 & c^2 & 0 \\ 0 & 0 & b^2 \end{bmatrix}$$

The inertia components of an inclined plate can be retrieved exploiting the formula of the moments of inertia expressed with respect to inclined axes, reported in (4.4) [56]. Computing the inertia of an area tilted of a certain angle is in fact equivalent to computing it with respect to axes inclined of the same angle. The component of inertia associated with the rotation axis will be preserved.
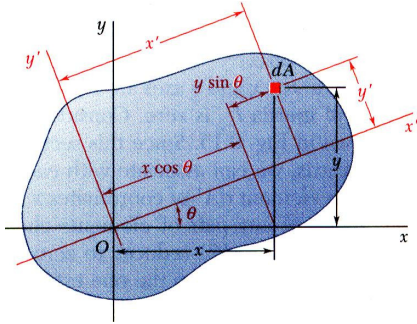
$$J_{x'} = \frac{J_x + J_y}{2} + \frac{J_x - J_y}{2} \cos 2\theta - J_{xy} \sin 2\theta$$

$$J_{y'} = \frac{J_x + J_y}{2} - \frac{J_x - J_y}{2} \cos 2\theta + J_{xy} \sin 2\theta$$

(4.4)

$$J_{x'y'} = \frac{J_x - J_y}{2} \sin 2\theta + J_{xy} \cos 2\theta$$

The CubeSat body can be assimilated to a cuboid, while each of the two SAs to a plate. At $\Delta = 0°$, the SA, characterized by height h and length l, is facing towards z and has therefore the inertia reported in (4.5).

$$J_{SP}\bigg|_{(\Delta=0°)} = \frac{m_{SP}}{12} \begin{bmatrix} l^2 & 0 & 0 \\ 0 & h^2 & 0 \\ 0 & 0 & l^2 + h^2 \end{bmatrix}$$

(4.5)

Parametrizing with respect to the tilt angle Δ, the moments of inertia of the SP in a general case are expressed in (4.6). In this case, the y component is preserved because the rotation is around that axis.

$$
\begin{aligned}
J'_{SP_x} &= \frac{J_x + J_z}{2} + \frac{J_x - J_y}{2} \cos 2\Delta = J_x - (J_x - J_z) \sin^2 \Delta = \frac{ml^2}{12} + \frac{mh^2}{12} \sin^2 \Delta \\
J'_{SP_z} &= \frac{J_x + J_z}{2} - \frac{J_x - J_z}{2} \cos 2\Delta = J_z + (J_x - J_z) \sin^2 \Delta = \frac{ml^2}{12} + \frac{mh^2}{12} \cos^2 \Delta \\
J'_{SP_{xz}} &= \frac{J_x - J_z}{2} \sin 2\Delta = -\frac{mh^2}{12} \sin \Delta \cos \Delta
\end{aligned}
\tag{4.6}
$$

The inertia tensor pf the SP for a generic tilting angle, with respect to its COM, is therefore obtained in (4.7).

$$
J_{SP} = \frac{m_{SP}\, h^2}{12}
\begin{bmatrix}
\left(\frac{l}{h}\right)^2 + \sin^2 \Delta & 0 & 0 \\
0 & 1 & -\sin \Delta \cos \Delta \\
0 & -\sin \Delta \cos \Delta & \left(\frac{l}{h}\right)^2 + \cos^2 \Delta
\end{bmatrix}
\tag{4.7}
$$

The last step is to express J_{SP} with respect to M-Argo COM. To accomplish this, the tensor generalization of the parallel axis theorem allows to transport the inertia tensor of a body in its COM to another point displaced of a vector $\boldsymbol{d}$ with respect to it [57]. The formula and the two vectors used for M-Argo SP are reported in (4.8), where $\otimes$ represents the outer product.

$$
\hat{J}_{SP} = J_{SP} + m_{SP} \left[(\boldsymbol{d} \cdot \boldsymbol{d}) \mathbb{I} - \boldsymbol{d} \otimes \boldsymbol{d} \right]
$$

$$
\boldsymbol{d}_{SP_1} = \left(\frac{b}{2} + l_h + \frac{l}{2} \right)
\begin{bmatrix} 0 \\ -1 \\ 0 \end{bmatrix}
$$

$$
\boldsymbol{d}_{SP_2} = \left(\frac{b}{2} + l_h + \frac{l}{2} \right)
\begin{bmatrix} 0 \\ 1 \\ 0 \end{bmatrix}
\tag{4.8}
$$

The overall inertia is finally computed as the sum of the body and SP inertia tensors, as shown in (4.9).

$$
J = J_{body} + \hat{J}_{SP_1} + \hat{J}_{SP_2}
\tag{4.9}
$$

4.3 Environment

This block provides information on the external bodies and their effects on the simulation in terms of power, forces and torques. Four inner blocks are identified with distinct functions:

compute the gravity force $\boldsymbol{F}_g$, the Sun direction $\hat{\boldsymbol{S}}$, the disturbance torque $\boldsymbol{T}_d$ and the on-board available power P_{av}. Their connections are shown in *Figure 4.3*.
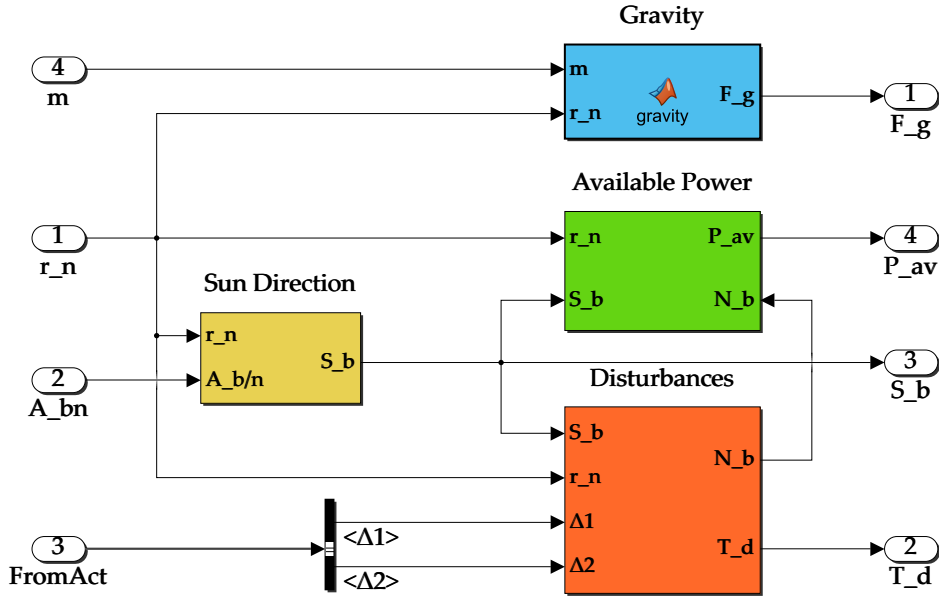
Figure 4.3: Environment block

Gravity

The gravity force is simply given by Newton's Law of Universal Gravitation in (4.10) because the Sun has been considered as main and only contributor for the gravity field. In fact, the scope of these preliminary simulations is to just prove the feasibility of the WOL strategies, which does not require a precise gravity force evaluation. Moreover, during M-Argo deep-space trajectory, the other bodies in the solar system have a mild effect on the trajectory propagation, especially in short windows of integration such as in the case of a WOL process. This assumption will be confirmed later on *section 5.4*, when all the planets will be considered to check the impact of the WOL strategies on the trajectory with respect to the case without WOL.

$$F_g = -\frac{m\mu_\odot}{||\boldsymbol{r}||^3}\,\boldsymbol{r} \qquad \text{where} \quad \mu_\odot = G\,m_\odot \tag{4.10}$$

Sun Direction

The Sun direction with respect to the body frame is required to compute both the available power and the SRP. Given the simple gravity field, the barycenter of the entire mass system is coincident with the Sun position. This means that the s/c position coincides with the Sun-to-s/c vector, and the Sun direction in inertial frame is just given by the opposite of the normalized s/c position. The transformation to the body frame is then obtained with the correspondent DCM matrix, as shown in (4.11).

$$\hat{S}_b = A_{b/n}\hat{S}_n \qquad \hat{S}_n = -\frac{\boldsymbol{r}}{||\boldsymbol{r}||} \tag{4.11}$$

Disturbances

The disturbances are all the external torques acting on the s/c that are not under the direct control of the actuators. In these simulations, only the SRP torque will be considered for reasons that will now be explained in details.

In general, any satellite is subjected to a GG torque due to the different gravity force experienced by some parts of the s/c with respect to others. For instance, long appendages with a counterweight at the end can be used to stabilize the attitude passively thanks to this phenomenon. For deep-space mission, this disturbance torque can be neglected due to the very low relative maximum distance from the Sun of one SP with respect to the other. Since the distance from the main attractor is on the order of AU and not in the order of hundreds of km as in a LEO, the difference between the gravity levels is lower. Moreover, the nominal attitude of M-Argo considers its appendages perpendicular to the Sun, so this effect should be cancelled for the entire duration of the mission.

Another disturbance torque that is usually considered is the one due to drag. In LEO, this is the main cause of orbital decay. In case of M-Argo, the infinitesimal density of the deep space is not expected to produce a force on the faces of the satellite large enough to generate a torque around the COM.

The last disturbance that can be safely neglected, but that is usually accounted for, is the one due to the magnetic field. Again, in a LEO, the Earth magnetic field is strong enough to interact with the magnetic dipole generated by the parasitic currents of the s/c. As it can be seen in *Figure 4.4*, for a 300 km orbit its lowest value is around 20 000 nT. On the other hand, the typical values for the maximum interplanetary magnetic field intensity at 1 AU are about 20 nT [58].

Unlike the previous disturbances, the SRP can not be neglected and shall be considered also
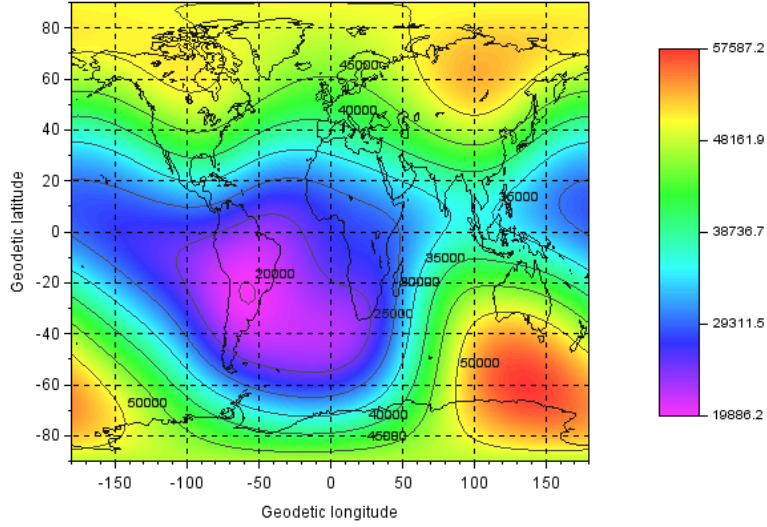
Figure 4.4: Magnetic field intensity in nT at 300 km. Courtesy of González [59]

because of its constant presence, due to the absence of eclipses. The model (1.5) presented in *subsection 1.3.3* is iterated for each face of the s/c to compute the overall SRP torque, considering the area surfaces, their normals and CP locations as defined in *section 2.3*. The solar pressure is computed taking an inverse parabolic solar irradiance model, using (4.12), where G_{SC} is the Solar Constant and r is expressed in AU [60].

$$P = \frac{\Phi_\odot}{c}$$

$$\Phi_\odot = G_{SC} \frac{1}{||\boldsymbol{r}||^2} \qquad G_{SC} = 1362 \, \frac{\text{kW}}{\text{m}^2} \tag{4.12}$$

The block then takes as input the tilting angles Δ_1 and Δ_2, the Sun direction in body frame $\hat{S}_b$ and the s/c position r to compute the SRP disturbance torque at each instant.

Available Power

The available power is computed from the Sun distance according to the fitting law previously saw in *Table 2.5*. However, this law accounts for SP that are completely facing the Sun, and this is not the case during coasting WOL strategies. A *reduction coefficient* λ should be considered, to apply to the maximum power P_{max}. This coefficient depends on the Sun Aspect Angle (SAA) of each panel, labelled as β in (4.13). The SAA is the angle between the SP normal $\hat{n}$ and the sun direction $\hat{S}$. When both the normals are aligned with

$\hat{S}$, the SAA of the two panels are zero and the power is equal to the theoretical one.

$$P_{av} = \lambda\, P_{theory} \qquad \lambda = \frac{1}{N_{SP}} \sum_{i=1}^{N_{SP}} \lambda_i$$

$$\lambda_i = \begin{cases} 0 & |\beta_i| > \frac{\pi}{2} \\ \cos \beta_i & |\beta_i| \le \frac{\pi}{2} \end{cases} \qquad (4.13)$$

$$\beta_i = \arccos\left(\hat{\boldsymbol{n}}_i \cdot \hat{\boldsymbol{S}}_b\right)$$

4.4 Sensors

This block gathers the real physical quantities and after the addition of noises, delays and errors, send the "measured" quantities to the Navigation block in the FromSens bus. In some cases dynamical models of the sensors can be used. However, for these simulations the sensors will be considered ideal because the goal is the demonstration of the algorithms.

Therefore, the IMU will measure an angular rate equal to the real one, as well as the STR for the attitude and the FSS for the Sun direction in body frame. Moreover, for the WOL it is mandatory to have knowledge of the angular momentum on each RW. Therefore, also this quantity is taken as input and inserted into the output bus, whose structure is shown in *Figure 4.5*.

FromSens

$$\omega \qquad A_{b/n} \qquad \hat{S}_b \qquad h_{RW}$$
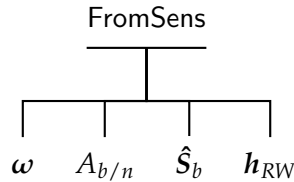
Figure 4.5: FromSens bus

4.5 Actuators

This block embeds the three models of the actuators used in M-Argo during WOL: RWS, gimballed thruster and SADM. An overview of the block is shown in *Figure 4.7*. The output is the FromAct bus, that includes the signals shown in *Figure 4.6*.
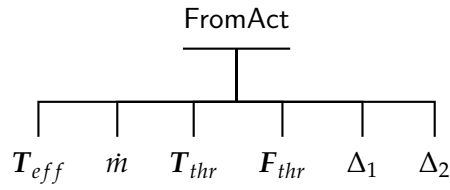
Figure 4.6: FromAct bus
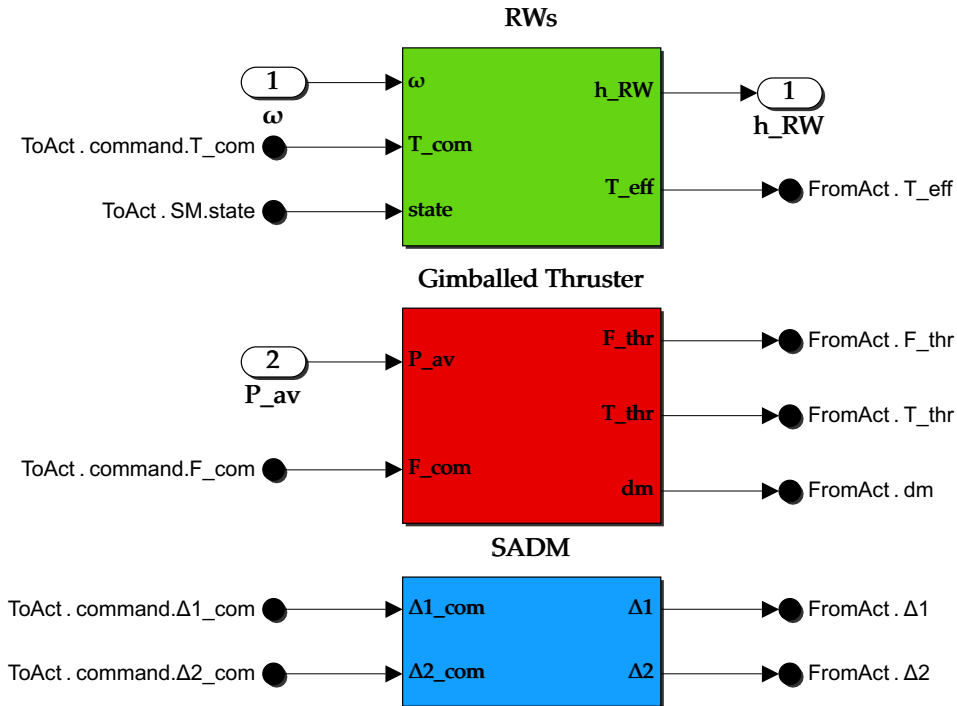
Figure 4.7: Actuators block

Reaction Wheels

The RWS model implements the dynamics using the set of equations (1.3) presented in *subsection 1.3.1*. The input are the angular rate ω and the commanded torque T_{com}. The saturation and maximum torque levels are the ones associated to M-Argo wheels. The configuration matrix is reported in (4.14) and refers to a 4 RWS assembly oriented along $-x$. Moreover, the state is took as additional input because in case its value goes to 3, it means that a WOL singularity has been detected and the commanded torque must be by-passed,

imposing the momentum derivative in (3.18) with a gain of $k = 10^{-4}$.

$$R = \begin{bmatrix} -1 & -1 & -1 & -1 \\ 1 & -1 & 1 & -1 \\ 1 & 1 & -1 & -1 \end{bmatrix} \tag{4.14}$$

The block outputs the angular momentum of the RWS h_{RW} and the effective control torque T_{eff}. The former will be sent to the sensors block while the latter will directly enter the dynamics.

Gimballed Thruster

The thruster model replicates the behaviour of the M-Argo gridded ion engine. The s/c available power in P_{av} and the commanded thrust vector F_{com} are taken as inputs. The specific impulse I_{sp} and available thrust F_{av} are computed from the capped power, according to the fitting laws previously saw in *Table 2.5*. If the commanded thrust level F_{com} is higher than F_{av}, then the actual thrust F_{thr} is capped to that level, according to (4.15).

$$F_{thr} = \begin{cases} F_{av} & F_{com} > F_{av} \\ F_{com} & F_{com} \leq F_{av} \end{cases} \qquad F_{com} = ||\boldsymbol{F}_{com}|| \tag{4.15}$$

Once all the quantities are computed, the equations in (4.16) are used to compute the effective thrust $\boldsymbol{F}_{thr}$, the thruster torque $\boldsymbol{T}_{thr}$ and the mass flow rate $\dot{m}$.

$$\begin{cases} \boldsymbol{F}_{thr} = F_{thr}\hat{\boldsymbol{g}} \\ \boldsymbol{T}_{thr} = \boldsymbol{d}_{thr} \times \boldsymbol{F}_{thr} = \begin{bmatrix} 0 \\ 0 \\ -\frac{c}{2} \end{bmatrix} \times \boldsymbol{F}_{thr} \\ \dot{m} = -\dfrac{F_{thr}}{I_{sp}g_0} \end{cases} \tag{4.16}$$

Solar Array Drive Mechanism

As already discussed previously, the dynamics of the SADM can be neglected and the model can be designed just as a feed-through of the commanded tilt angles. In fact, the maximum frequency that the actuator shall undergo is during SRPW, where two consecutive turns of 90° are performed in a period of 1 h. This results in a tilting rate of 0.05 °/s. Typical values of maximum rotational speed for micro-sat SADM are on the order of ≈ 1 °/s, so the dynamics can be considered instantaneous [61].

4.6 Navigation

The navigation is usually fulfilled applying low-pass filters and attitude determination algorithms to the sensor measurements, to respectively reject noises and determine the attitude.

Given the fact that the sensors information arrives to the OBC in form of exact attitude knowledge and without errors or noises, the navigation task can be practically ignored. As in the case of the sensors block, the navigation block feeds through the FromSens bus to the FromNav bus, copying the same information. The FromNav bus is then routed to the OBC and control blocks.

4.7 OBC

The block representing the computer is one of the most important in the simulation because it performs all the autonomous tasks. The inputs are the FromNav bus and the pointing error ϵ. The output is the FromOBC bus, structured as shown in *Figure 4.9*. An overview of the OBC block is reported in *Figure 4.8*. Three inner blocks can be identified, whose functions will now be explained in more details.

OBDH

The On-Board Data Handling (OBDH) block is in charge of extracting the information stored in the on-board memory, in this case the ephemeris of the pointing vector α and of the reference thrust magnitude F_{ref}. Moreover, processing the data that comes from the sensors, the sun direction in inertial frame can be retrieved and therefore also the DCM linking the pointing frame with the inertial one at each instant, applying the formula saw in *section 3.2*. At this point it is straightforward to extract $\hat{S}_p$ and $A_{b/p}$. The sequence of equations is reported in (4.17).

$$
\begin{aligned}
\hat{S}_n &= A_{b/n}^T \, \hat{S}_b \\
A_{p/n} &= ...(3.2)... \\
\hat{S}_p &= A_{p/n} \, \hat{S}_n \\
A_{b/p} &= A_{b/n} \, A_{p/n}^T
\end{aligned}
\tag{4.17}
$$
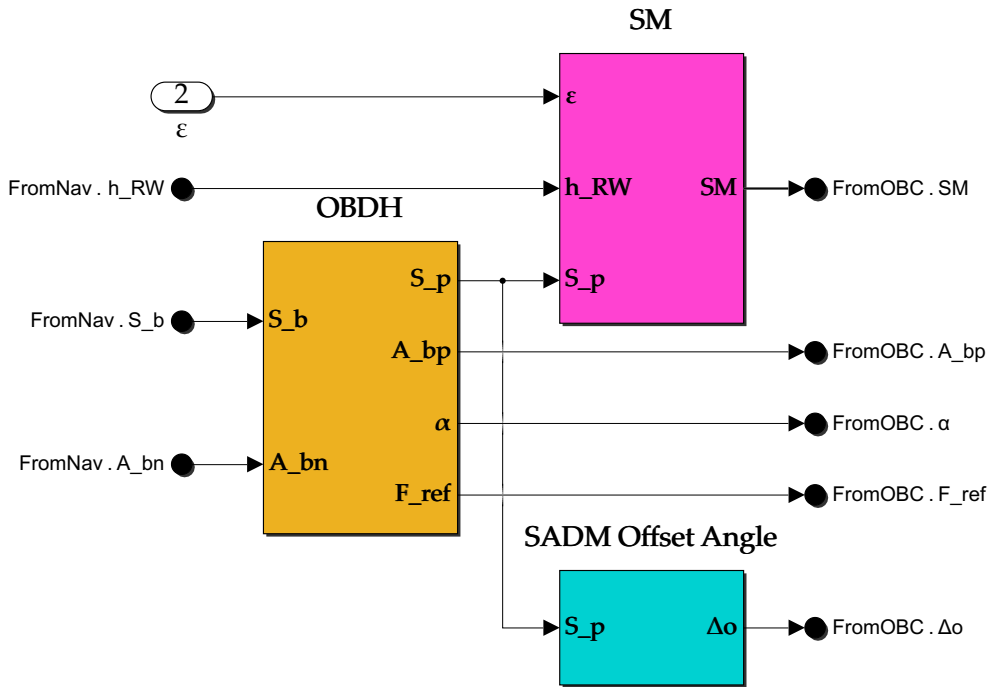
Figure 4.8: OBC block
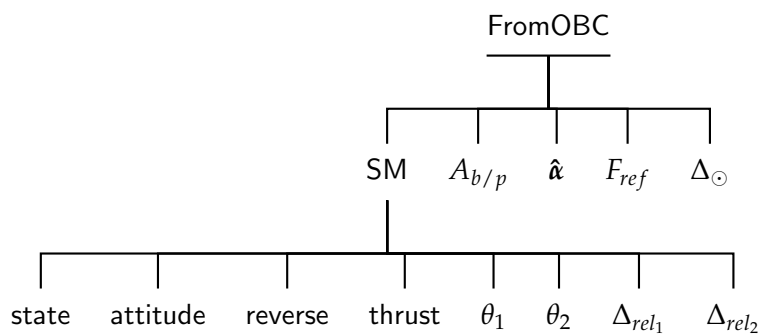
Figure 4.9: FromOBC bus

SM

The sm block embeds all the decision-making logic explained in *section 3.6*, and takes as input the pointing error, computed in the control block, the rws angular momentum, coming from the FromNav bus, and the Sun direction in pointing frame, coming from the obdh. Internally, the equivalent angular momentum is computed and the 6 dynamic flags referring to the momentum component intersections with zero and themselves are evaluated with zero-crossing counters. The thresholds on the pointing error and momentum norms required by the sm are inserted as constant parameters and reported in *Table 4.1*.

	Cruising	Coasting
$\bar{\epsilon}\,[-]$	0.004	0.02
$\bar{h}\,[\text{mNms}]$	0.3	
$\bar{h}_{end}\,[\text{mNms}]$	0.1	

Table 4.1: Thresholds for the pointing error and momentum norm used in the sm

As output of the block, the bus sm embeds all the information that the guidance block will require to generate the correct desired trajectories for the actuators and the attitude, depending on the state. In case of fixed attitude strategies, the two gimbal angles θ_1 and θ_2 are computed according to the algorithm (3.8), while the two tilting angles Δ_1 and Δ_2 are computed according to the truth table in *Table 3.2*. In case of beta and srpw, the guidance block will instead generate the angles in real-time.

SADM Offset Angle

The third block of the obc provides the offset angle that must be considered in the guidance laws in order to face the Sun when $\Delta_{rel} = 0°$. The input is the Sun direction in the pointing frame and the output is $\Delta_\odot$, computed using (3.10).

4.8 Guidance

This block exploits the obc data to provide to the control block the desired state that the s/c should follow. Its internal structure is shown in *Figure 4.10*. The output bus, labelled with FromGuid, is composed by the signals in *Figure 4.11*.
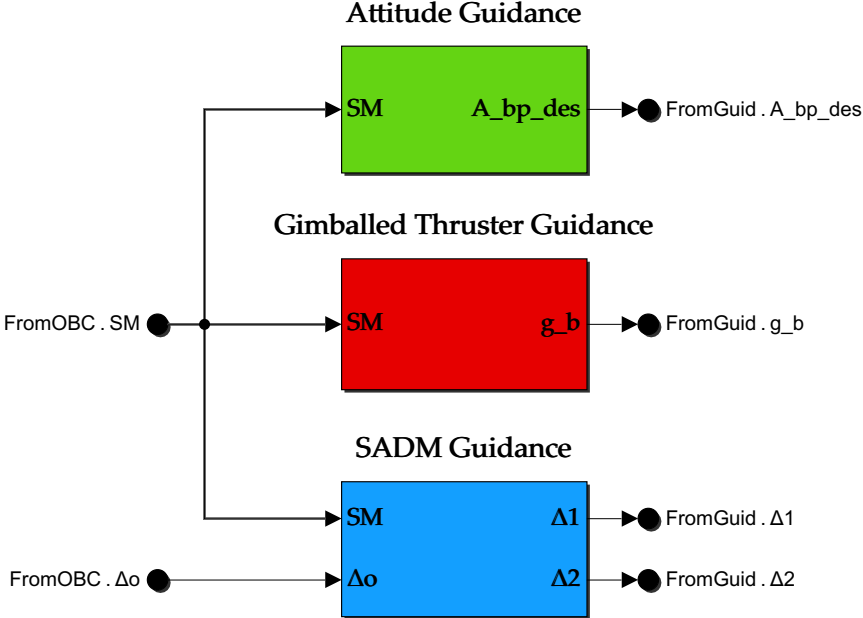
Figure 4.10: Guidance block
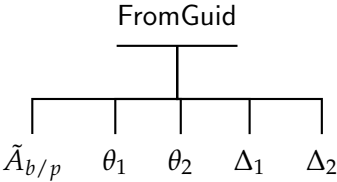
Figure 4.11: FromGuid bus

The attitude guidance block provides the desired attitude at each time step for either the BETA or the SRPW strategy. In case of a fixed attitude strategy, the desired body orientation with respect to the pointing frame is instead set to the identity.

The gimballed thruster guidance blocks provides the desired gimbal angles at each time step for the BETA strategy. The overall guidance law for BETA is reported in (4.18). In case of the Gimbal strategy, instead, the angles are set equal to the ones computed by the SM. For all the other cases, they are set to zero.

$$
\tilde{A}_{b/p} = \begin{bmatrix} \cos\phi_1 & 0 & -\sin\phi_1 \\ 0 & \cos\phi_2 & -\sin\phi_2 \\ \sin\phi_1 & \sin\phi_2 & \sqrt{1 - (\sin\phi_1)^2 - (\sin\phi_2)^2} \end{bmatrix}
$$

$$
\hat{g}_b = \begin{bmatrix} \sin\theta_1 \\ \sin\theta_2 \\ \sqrt{1 - (\sin\theta_1)^2 - (\sin\theta_2)^2} \end{bmatrix}
$$

$$
\phi_1 = \begin{cases} \phi_{max}\sin(\omega t) & \text{reverse} = 1 \\ -\phi_{max}\sin(\omega t) & \text{reverse} = -1 \end{cases}
$$

$$
\phi_2 = \phi_{max}\cos(\omega t) \tag{4.18}
$$

$$
\theta_1 = \begin{cases} -\theta_{max}\cos(\omega t) & \text{reverse} = 1 \\ \theta_{max}\cos(\omega t) & \text{reverse} = -1 \end{cases}
$$

$$
\theta_2 = \theta_{max}\sin(\omega t)
$$

$$
\omega = 2\pi f = \frac{2\pi}{T}
$$

The SADM guidance block provides the desired SA tilting angles at each time step for the SRPW strategy. The overall guidance law for SRPW is reported in (4.19). In case of either SSA or PW strategies, instead, the angles are set equal to the ones computed by the SM. For all the other cases, they are set to zero.

$$\tilde{A}_{b/p} = \begin{bmatrix} \cos\phi_2 & \sin\phi_2 & 0 \\ -\sin\phi_2 & \sqrt{1 - (\sin\phi_1)^2 - (\sin\phi_2)^2} & -\sin\phi_1 \\ 0 & \sin\phi_1 & \cos\phi_1 \end{bmatrix}$$

$$\phi_1 = \phi_{max}\sin(\omega t)$$
$$\phi_2 = \phi_{max}\cos(\omega t)$$

$$\Delta_1 = \begin{cases} \Delta_\odot + 90° \min\left(1, 1 + \cos\left(\omega t + \Delta_\odot\right)\right) & \text{reverse} = 1 \\ \Delta_\odot + 90° \min\left(1, 1 - \cos\left(\omega t + \Delta_\odot\right)\right) & \text{reverse} = -1 \end{cases}$$

$$\Delta_2 = \begin{cases} \Delta_\odot + 90° \min\left(1, 1 - \cos\left(\omega t + \Delta_\odot\right)\right) & \text{reverse} = 1 \\ \Delta_\odot + 90° \min\left(1, 1 + \cos\left(\omega t + \Delta_\odot\right)\right) & \text{reverse} = -1 \end{cases}$$

$$\omega = 2\pi f = \frac{2\pi}{T}$$

(4.19)

All the three blocks use the constant parameters reported in *Table 4.2*.

	BETA	SRPW
$T\,[\text{h}]$	1/3	2
$\phi_{max}\,[°]$	5	20
$\theta_{max}\,[°]$	5	-

Table 4.2: Period and maximum excursion angles of BETA and SRPW strategies

4.9 Control

This last block is in charge of computing the actuators commands in such a way to follow the desired state. An overview of the block is shown in *Figure 4.12*. The inputs are the buses coming from the navigation, guidance and OBC blocks. As output, the bus ToAct is obtained, with the structure reported in *Figure 4.13*.

Attitude Control

FromNav . ω

FromGuid . A_bp_des

FromOBC . A_bp

ω

A_bp_des

A_bp

decision

ε → 2
ε

T_com → ToAct . command.T_com

FromOBC . SM → ToAct . SM

Thruster Control

FromGuid . g_b

FromNav . A_bn

FromOBC . α

FromOBC . F_ref

SM

g_b

A_bn

α

F_ref

F_com → ToAct . command.F_com

SADM Control

FromGuid . Δ1

FromGuid . Δ2

Δ1

Δ2

Δ1_com → ToAct . command.Δ1_com

Δ2_com → ToAct . command.Δ2_com
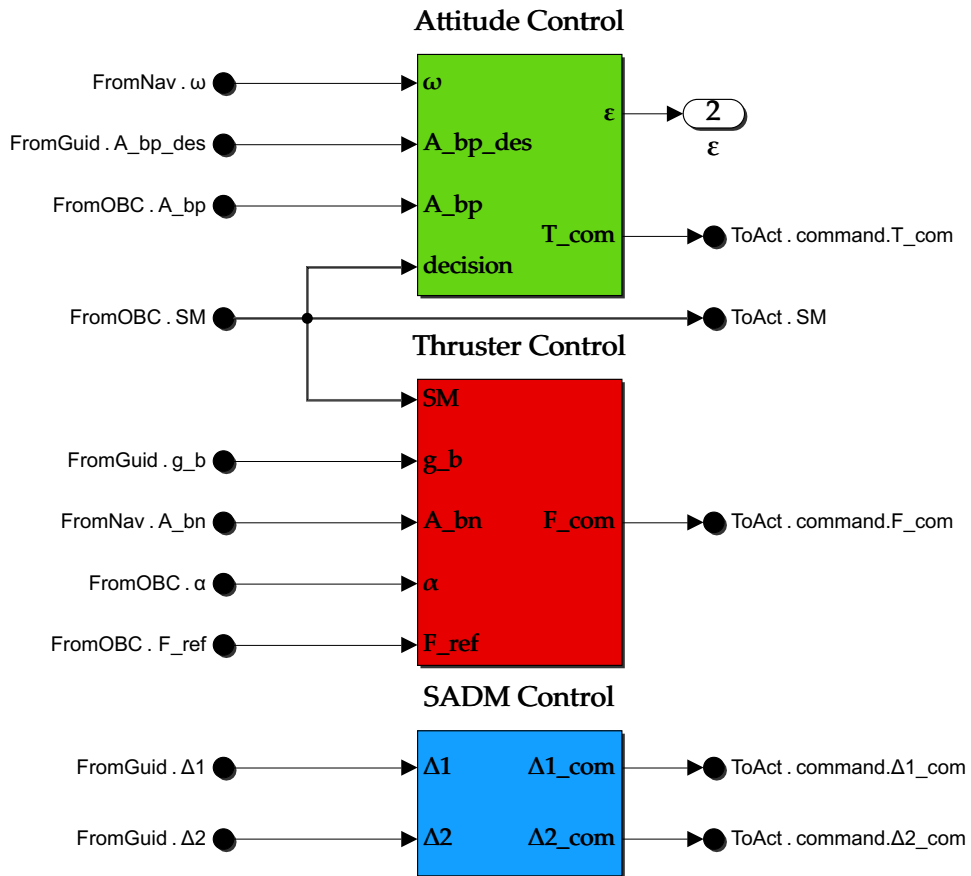
Figure 4.12: Control block

ToAct

command   SM

T_{com} F_{com} $\Delta_{1_{com}}$ $\Delta_{2_{com}}$
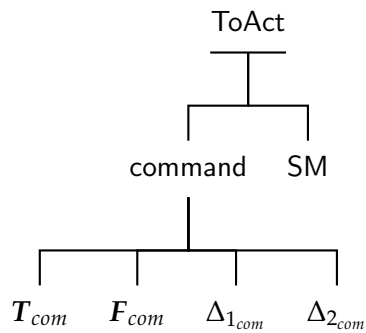
Figure 4.13: ToAct bus

75

Attitude Control

For the attitude control, two controllers were investigated: a Linear Quadratic Regulator (LQR) and a tracking controller. A quick overview of their advantages and drawbacks is required before the choice.

Regarding LQR, the gain of this feedback controller is computed in such a way to minimize the quadratic cost function defined in (4.20), where z and u are respectively the performance and the control of the dynamic system in state-space form [62].

$$u(t) = -K_{LQR}x(t)$$

$$\mathcal{J} = \frac{1}{2}\int_0^\infty \left(z^T W_{zz}z + u^T W_{uu}u \right) dt \qquad (4.20)$$

$$\dot{x}(t) = Ax(t) + Bu(t)$$
$$z(t) = Cx(t) + Du(t)$$

The first term represents the performance, the deviation from the desired state. The second term instead represents the control effort. The goal is to keep as small as possible both terms. In other words, to obtain the best result with the smallest control effort. The weighting matrices are used to trade off the two effects: a W_{zz} much higher than W_{uu} would mean that a good performance is seeked, regardless of the control effort. On the other hand, keeping an high W_{uu} would reduce the actuators torque at the expense of an higher error.

The pointing error ϵ has been chosen as figure of merit for the performance. The vector can be obtained using the inverse hat map operator, as shown in (4.21).

$$\epsilon = \begin{bmatrix} \epsilon_x \\ \epsilon_y \\ \epsilon_z \end{bmatrix} = \left(A_{err}^T - A_{err} \right)^V$$

$$\text{where} \quad A_{err} = A_{b/p}\tilde{A}_{b/p}^T \qquad (4.21)$$

$$A^V = \begin{bmatrix} a_{11} & a_{12} & a_{13} \\ a_{21} & a_{22} & a_{23} \\ a_{31} & a_{32} & a_{33} \end{bmatrix}^V = \frac{1}{2}\begin{bmatrix} a_{32} - a_{23} \\ a_{13} - a_{31} \\ a_{21} - a_{12} \end{bmatrix}$$

Conceptually, ϵ represent a set of angles and therefore its derivative can be set equal to the angular rate. Employing the linearized Euler equations, that neglect the gyroscopic

coupling, the state-space system in (4.22) can be constructed.

$$
\underbrace{\begin{bmatrix} \dot{\epsilon} \\ \dot{\omega} \end{bmatrix}}_{\dot{x}} = \underbrace{\begin{bmatrix} 0 & \mathbb{I} \\ 0 & 0 \end{bmatrix}}_{A} \underbrace{\begin{bmatrix} \epsilon \\ \omega \end{bmatrix}}_{x} + \underbrace{\begin{bmatrix} 0 \\ J^{-1} \end{bmatrix}}_{B} \underbrace{T_{com}}_{u}
$$

$$
z = \epsilon = \underbrace{\begin{bmatrix} \mathbb{I} & 0 \end{bmatrix}}_{C} \underbrace{\begin{bmatrix} \epsilon \\ \omega \end{bmatrix}}_{x}
$$

(4.22)

The optimal feedback gain K is computed solving the matrix algebraic Riccati equation, reported in (4.23).

$$
K_{LQR} = -W_{uu}^{-1} B^T P
$$
$$
\text{where} \quad P \quad \text{s.t.} \quad PA + A^T P + C^T W_{zz} C - PBW_{uu}^{-1} B^T P = 0
$$

(4.23)

To this aim, the weighting matrices used for the two scenarios are reported in (4.24).

$$
\text{cruising} \rightarrow \begin{cases} W_{uu} = \mathbb{I} \\ W_{zz} = 10^8 \, W_{uu} \end{cases}
$$

$$
\text{coasting} \rightarrow \begin{cases} W_{uu} = \mathbb{I} \\ W_{zz} = 10^5 \, W_{uu} \end{cases}
$$

(4.24)

Finally, the commanded torque T_{com} is computed using (4.25).

$$
T_{com} = -K_{LQR} \begin{bmatrix} \epsilon \\ \omega \end{bmatrix}
$$

(4.25)

The LQR is a valid controller to use in case of a fixed or almost-fixed set-point, such as when the angular rate must be set to zero during de-tumbling, or when the body frame is required to be coincident with the pointing frame. In some of the presented strategies, however, the guidance imposes an attitude motion that must be *tracked* in real-time. For this reason, a more suitable choice could be represented by a Lyapunov-stable tracking controller, whose formulation is reported in (4.26) [7].

$$
u = -K_\epsilon \epsilon - K_\omega \, \omega_{err} + \omega \times J\omega - J \left[\omega_{err} \right]^\wedge A_{err} \, \tilde{\omega}
$$

$$
\text{where} \quad \omega_{err} = \omega - A_e \, \tilde{\omega}
$$

(4.26)

In the expression the desired angular rate $\tilde{\omega}$ is employed. This quantity is not known a-priori and has to be numerically computed at each time step from the desired attitude $\tilde{A}_{b/p}$, using (4.27). The formula is obtained inverting the DCM kinematics.

$$
\dot{\tilde{A}}_{b/p} = - \left[\tilde{\omega} \right]^\wedge \tilde{A}_{b/p} \quad \rightarrow \quad \tilde{\omega} = \left(-\dot{\tilde{A}}_{b/p} \, \tilde{A}_{b/p}^T \right)^V
$$

(4.27)

The two gains, reported in (4.28), differ according to the scenario under consideration because the maximum excursion angle ϕ_{max} for SRPW is 5 times larger than for BETA.

$$
\begin{aligned}
\text{cruising} &\rightarrow \begin{cases} K_\epsilon = 0.005 \\ K_\omega = 0.5 \end{cases} \\
\text{coasting} &\rightarrow \begin{cases} K_\epsilon = 0.00005 \\ K_\omega = 0.05 \end{cases}
\end{aligned}
\tag{4.28}
$$

Thruster Control

Regarding the thruster control, the gimbal vector has already been computed but the thrust magnitude is still a free DOF. Its computation relays on the algorithm presented in *section 3.3*. In particular, the commanded thrust $\boldsymbol{F}_{com}$ will have a norm higher than the reference such to still provide the same amount along the original pointing vector. Its full expression is reported in (4.29).

$$
\boldsymbol{F}_{com} = \frac{F_{ref}}{(A_{n/b}\,\hat{\boldsymbol{g}}_b) \cdot \hat{\boldsymbol{\alpha}}}\,\hat{\boldsymbol{g}}
\tag{4.29}
$$

SADM Control

The SADM control is again a feed-through of the tilting angles, because the commanded angles have been already computed exactly in the guidance block.

4.10 RCS Comparison

The RCS block is treated in a separate section because it is not involved in the simulation loop, since none of the WOL techniques presented involves the usage of this system. Nevertheless, it exploits the data produced by several blocks in real-time and therefore can not be used in post-processing, after the simulation is finished.

One of the most interesting aspects in the WOL strategies presented is the possibility to use the main thrust, with a small offset, to generate torques, instead of having a dedicated RCS system on-board. Therefore, it should be interesting to understand how much these methods are more efficient with respect to the case where the WOL is performed with a RCS, which is usually the standard for a deep-space mission.

M-Argo indeed encompasses this system in its architecture, and therefore the comparison can be easily performed, using a real-time RCS model that activates its thrusters to produce the same torques that are produced by the main thruster in the pointing frame. Each RCS thruster, when active, produce a force that depletes the propellant tank. The force is then multiplied for the distance from the COM, to produce "fake" torques, that are not actually used in the simulation loop, but they must be coincident with the ones produced by the WOL strategies. The propellant mass that is consumed by the RCS and the main thruster along the trajectory is then saved to be compared to the original case.

It should be noticed that the RCS could theoretically perform the de-saturation of the same momentum levels in a much shorter time: in this way they are forced to follow the same torques-over-time trend. However, this comparison allows to appreciate the possible savings in mass of the developed strategies, with respect to RCS, under the same "energy" expense. In fact, when it comes to mass consumption, one should consider that the specific impulse of such systems is typically very low when compared to the ion gridded engine, 16 s versus ≈ 3500 s.

As first step, the definition of the torques that the RCS system should replicate is carried out in (4.30). For the Gimbal strategy, the de-saturation torque is the one around δ and β axes, while in BETA it is only the one around α. In this way the RCS system generates only the useful torques and neglect the oscillatory components that do not have a net effect.

$$
\boldsymbol{T}_{RCS} = \begin{cases} \begin{bmatrix} T_{thr_\delta} \\ T_{thr_\beta} \\ 0 \end{bmatrix} & \text{GIMBAL} \\[2em] \begin{bmatrix} 0 \\ 0 \\ T_{thr_\alpha} \end{bmatrix} & \text{BETA} \end{cases}
\tag{4.30}
$$

When the required torques are defined, the problem of thrust *allocation* must be solved. In fact, depending on the distribution of the thrusters on the body, some of them can be switched off because their contribution is not needed. The allocation strategy is straightforward for a set of 12 thrusters and consists in just applying (4.31), where $\boldsymbol{d}_{RCS}$ and $\hat{\boldsymbol{n}}_{RCS}$ have been defined in *section 2.3*.

$$
\boldsymbol{F} = R_{RCS}^\star \boldsymbol{T}_{RCS} \qquad \text{where} \quad R_{RCS} = \boldsymbol{d}_{RCS} \times \hat{\boldsymbol{n}}_{RCS}
\tag{4.31}
$$

However, one must take care that the resulting thrust can not be taken as valid if it results negative. In case of M-Argo configuration, a negative thrust will be obtained always by

half of the RCS thrusters. Therefore, the actual thrust F_{RCS} for each of them follows (4.32). The total thrust will be the sum of all the contributions.

$$F_{RCS} = \sum_{i=1}^{N_{RCS}} F_{RCS_i} \quad \text{where} \quad F_{RCS_i} = \begin{cases} 0 & F_i \leq 0 \\ 2F_i & F_i > 0 \end{cases} \tag{4.32}$$

Once the total thrust is computed, (4.33) can be integrated to retrieve the mass consumption in case RCS were used instead of the WOL techniques presented in this work. The first term in the equation refers to the contribution of the main thruster, that is still used but follows the nominal thrust level F_{ref} and is characterized by a specific impulse associated at each instant with P_{max}.

$$\dot{m} = -\frac{F_{ref}}{I_{sp_{max}} g_0} - \frac{F_{RCS}}{I_{sp_{RCS}} g_0} \tag{4.33}$$

5

Simulation Results

O-NCE the testing environment has been set, the simulation campaign can start. For each scenario, the results of the autonomous WOL for a 3 RWS and 4 RWS assembly will be presented, highlighting the most important aspects. The simulations will be carried out using a variable-step ode45 solver, with relative and absolute tolerances set to 10^{-10}.

5.1 Initial Conditions

The Initial Conditions (ICS) that will be used in each run are reported in *Table 5.1*. The starting date t_0 dictates the initial pose for the scenario under consideration: the position r_0 and the velocity v_0 are directly extracted from the optimal trajectory data, whilst the initial attitude is set coincident with the pointing frame orientation at that date, evaluated with (5.1).

When considering a coasting scenario, the pointing vector is not defined and therefore the pointing frame orientation is set equal to the one used on the previous cruising arc and kept constant throughout all the coasting period.

	Cruising		Coasting	
t_0	04/02/24		10/02/24	
r_0	$\boldsymbol{r}_{ref}(t_0)$		$\boldsymbol{r}_{ref}(t_0)$	
v_0	$\boldsymbol{v}_{ref}(t_0)$		$\boldsymbol{v}_{ref}(t_0)$	
A_{b/n_0}	$A_{p/n}(t_0)$		$A_{p/n}(t_0)$	
$\boldsymbol{\omega}_0$	$\begin{bmatrix} 0 \\ 0 \\ 0 \end{bmatrix}$		$\begin{bmatrix} 0 \\ 0 \\ 0 \end{bmatrix}$	
m_0	$m(t_0)$		$m(t_0)$	
n_{RW}	3	4	3	4
h_0	$\begin{bmatrix} 19 \\ 8 \\ -7 \end{bmatrix}$	$\begin{bmatrix} 15 \\ -8 \\ 4 \\ -19 \end{bmatrix}$	$\begin{bmatrix} -19 \\ 6 \\ -7 \end{bmatrix}$	$\begin{bmatrix} 12 \\ -4 \\ 7 \\ 19 \end{bmatrix}$

Table 5.1: Initial conditions used in the simulations

$$A_{p/n}(t_0) = \begin{bmatrix} \delta & \beta & \alpha \end{bmatrix}^T \qquad \begin{aligned} \alpha &= \hat{\boldsymbol{\alpha}}_0 \\ \beta &= \hat{\boldsymbol{\alpha}}_0 \wedge \hat{\boldsymbol{S}}_0 \\ \delta &= (\hat{\boldsymbol{\alpha}}_0 \wedge \hat{\boldsymbol{S}}_0) \wedge \hat{\boldsymbol{\alpha}}_0 \end{aligned} \tag{5.1}$$

$$\text{where} \quad \begin{aligned} \hat{\boldsymbol{\alpha}}_0 &= \hat{\boldsymbol{\alpha}}(t_0) \\ \hat{\boldsymbol{S}}_0 &= -\frac{\boldsymbol{r}_0}{||\boldsymbol{r}_0||} \end{aligned}$$

The initial angular rate is always set to zero, while the initial mass is evaluated considering a simplified linear relation with time for the propellant consumption, reported in (5.2). From *Table 2.1*, the expected consumed mass of propellant for 2010-UE51 trajectory is equal to $m_p = 0.974 \, \text{kg}$.

$$m(t_0) = m_{tot} - \frac{t_0 - t_{start}}{\text{TOF}} \, m_p \tag{5.2}$$

Finally, the momentum values are chosen randomly, with the only constraint that at least one RW must be saturated.

5.2 Cruising Scenario

For the cruising scenario, the Gimbal and BETA strategies are exploited. Starting from the given ICs, the autonomous WOL will be demonstrated. Special attention should be given throughout all the process on the level of *over-thrust* required to accomplish them, as well as on the propellant mass consumption, if the goal is to prove the feasibility of such techniques but also their efficiency and the fact that do not put constraints in the operations nor on the design.

5.2.1 Orthogonal Assembly

The results of the simulation, considering an assembly of 3 RWS aligned with the body axes, are presented in *Figure 5.1*. The momentum is almost completely dumped: after the de-tumbling and final re-pointing the value of the norm is $h = 0.28$ mNms, the 1.3% of the initial value of $||h_0|| = 21.8$ mNms. The WOL is accomplished in $t = 1.9$ h.

The procedure begins with a Gimbal strategy to remove the momentum on x and y. Then, as soon as h_x crosses h_y, the BETA trajectory is initiated. As it can be seen in the plot, the torque generated by the thruster, expressed in the pointing frame, has a non-null component around α-axis, and this is why the momentum accumulated on that quasi-inertial direction can be off-loaded. The torques generated about the other two axes have a much larger magnitude, but their periodic nature does not cause any momentum accumulation on β and δ. However, since h_z crosses zero before the trajectory ends its harmonic period, a final additional Gimbal strategy is required to dump the remaining momentum.

Another interesting aspect is the over-thrust required to accomplish such torques. During the first gimbal strategy, $F_{com} = 1.006$ mN, just 0.4% higher than the reference value of $F_{ref} = 1.002$ mN. During BETA the over-thrust is expected to be higher because also the attitude motion should be considered as an additional factor of off-setting with respect to the pointing vector. In fact, $F_{com} = 1.009$ mN, 0.7% higher than the reference. These values strongly depend on the maximum gimbal and excursion angles chosen, if they are increased the WOL is performed faster but the risk of ending with a higher momentum value is increased because the oscillations of the momentum components will be higher.

In any case, these low values of over-thrust, together with the very high specific impulse, allow saving a relatively high amount of propellant, when compared to the case where the RCS is used to obtain the same torques. In particular, the additional propellant consumed for the WOL is respectively $\Delta m_p = 0.0014$ g and $\Delta m_{p_{RCS}} = 1.48$ g. The total mass saved is therefore of $\Delta m = 1.476$ g, which translates into a 99.7% of mass savings when using such techniques. This high value is mainly caused by the very low specific impulse of the RCS.
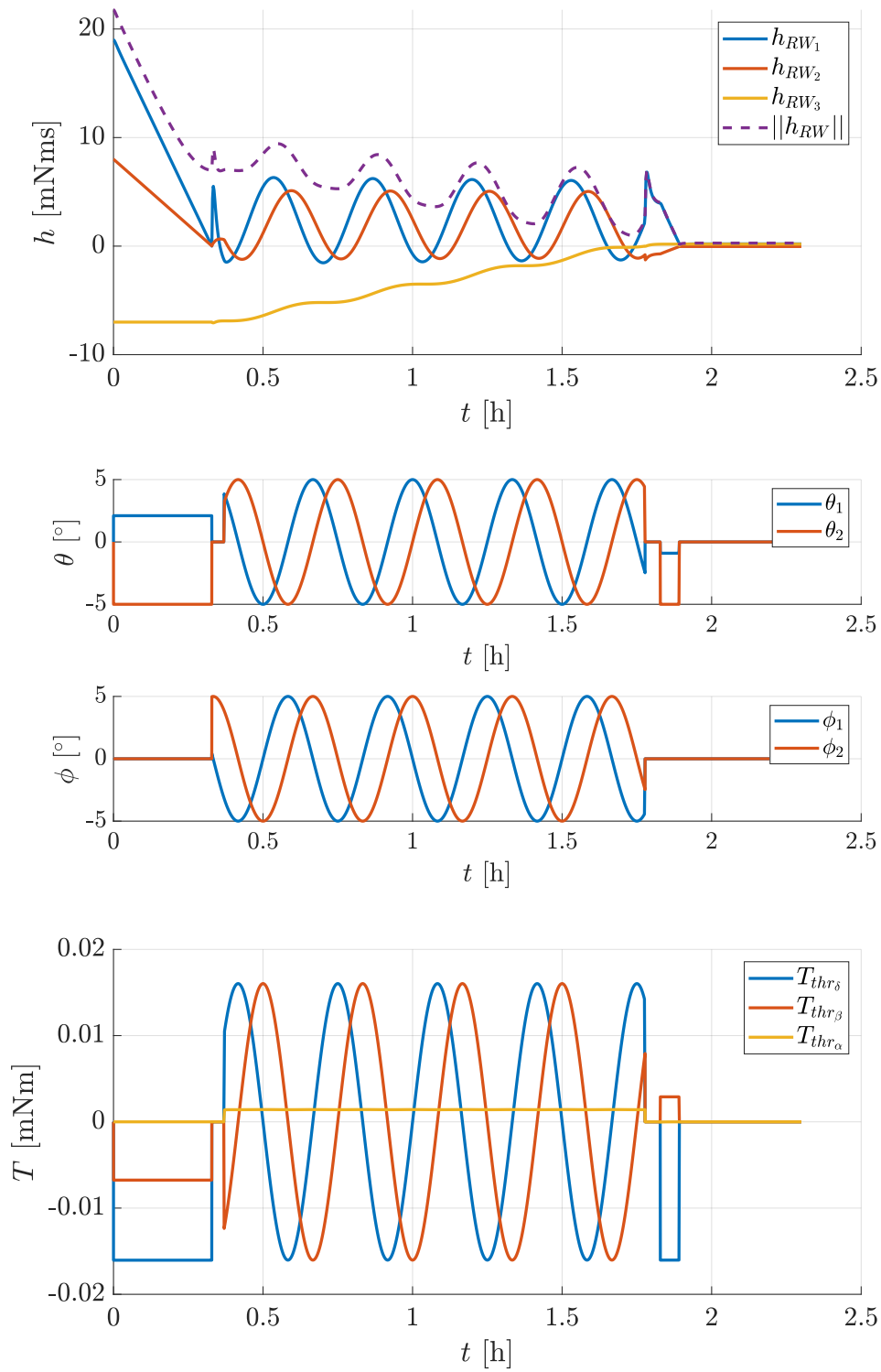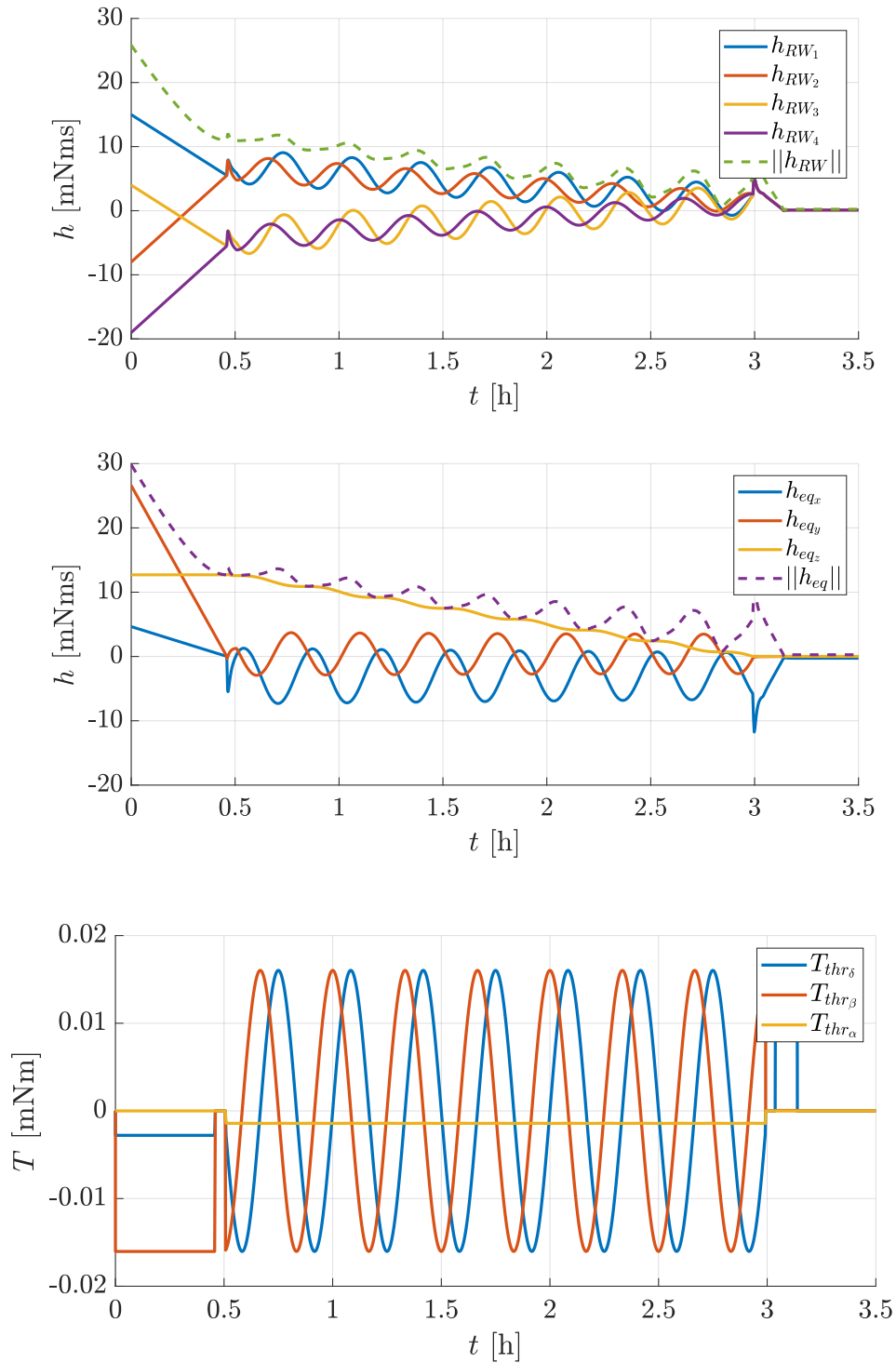
Figure 5.1: Simulation results of the autonomous wol in a cruising scenario with an assembly of 3 rws
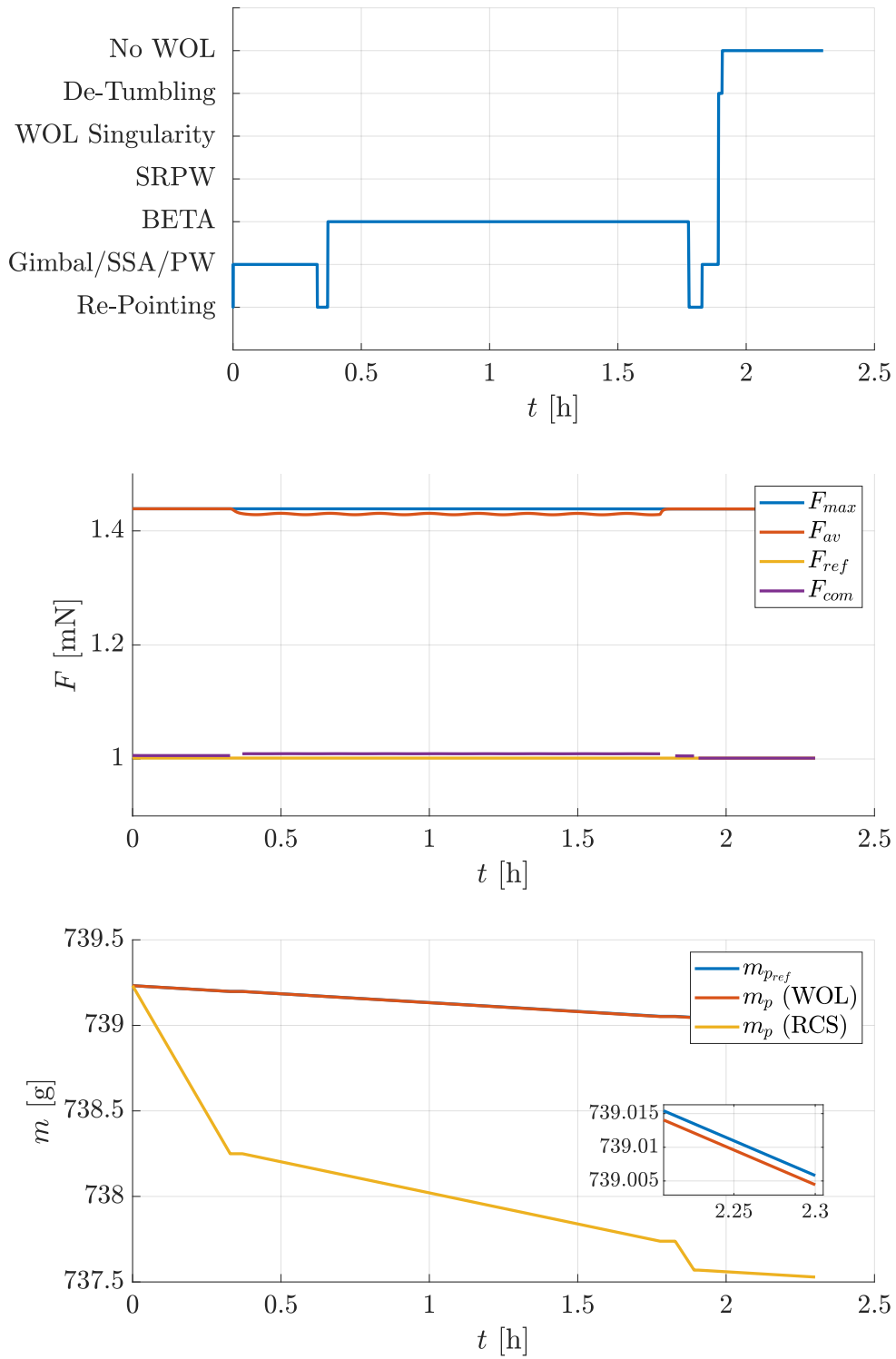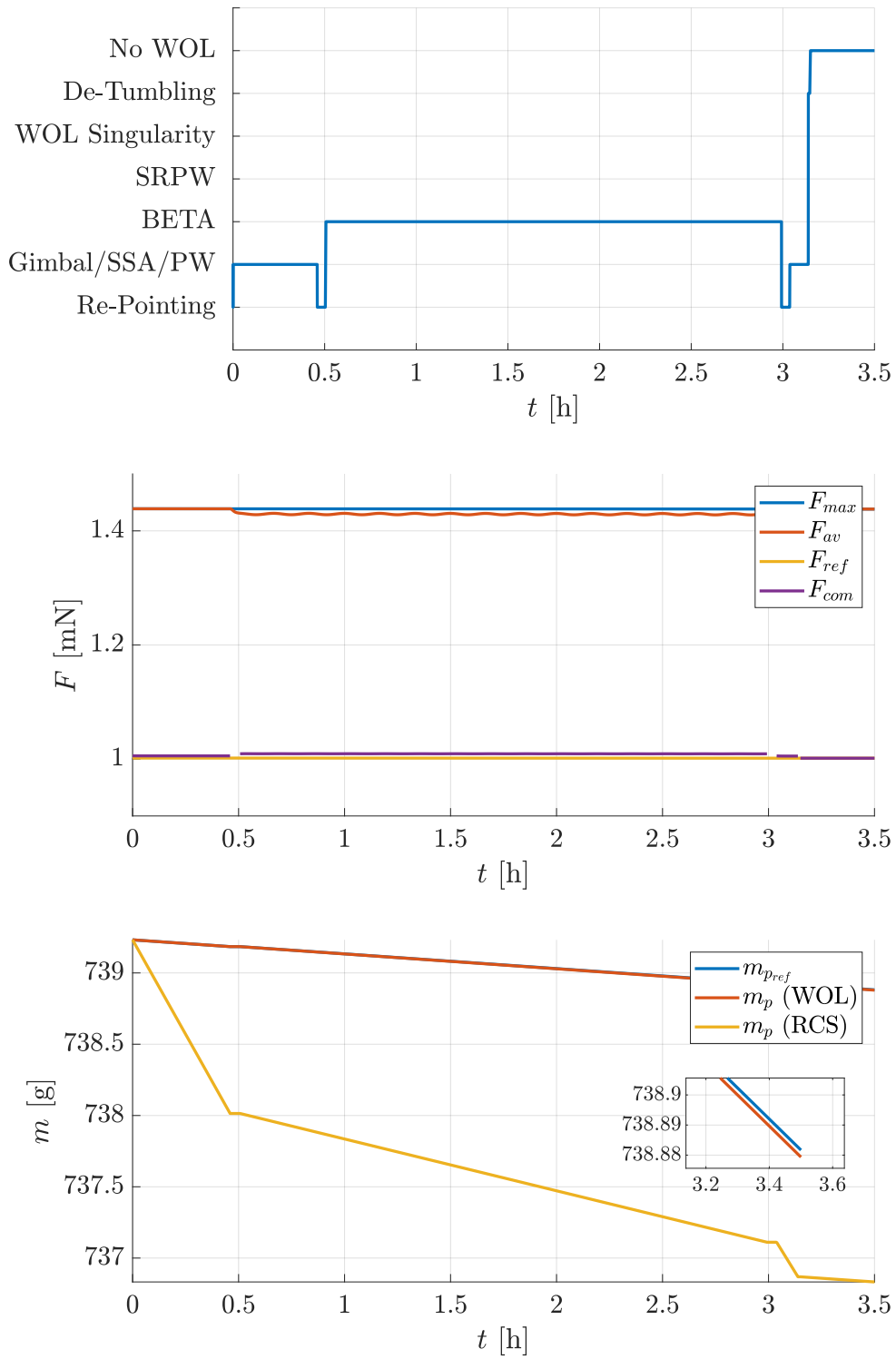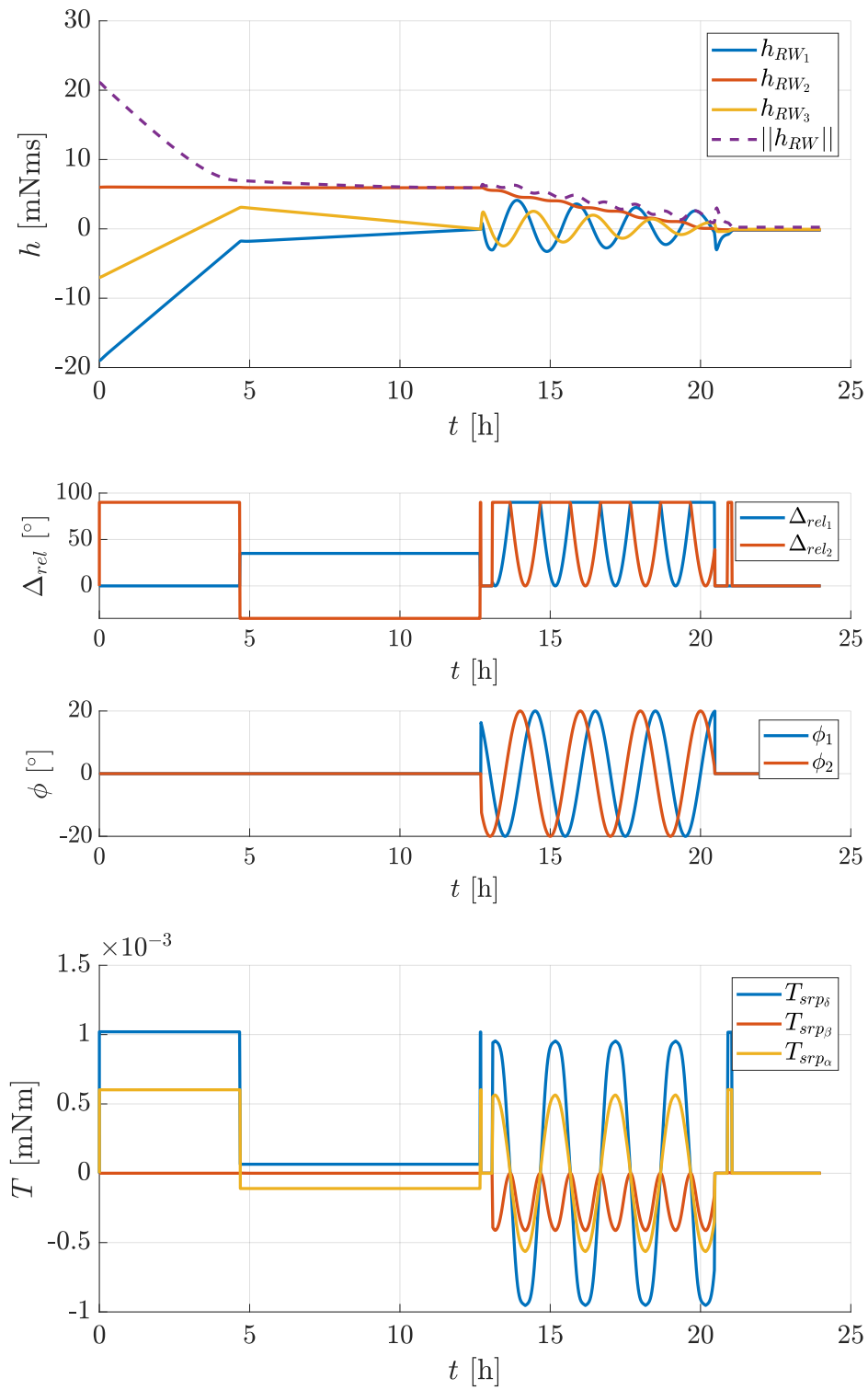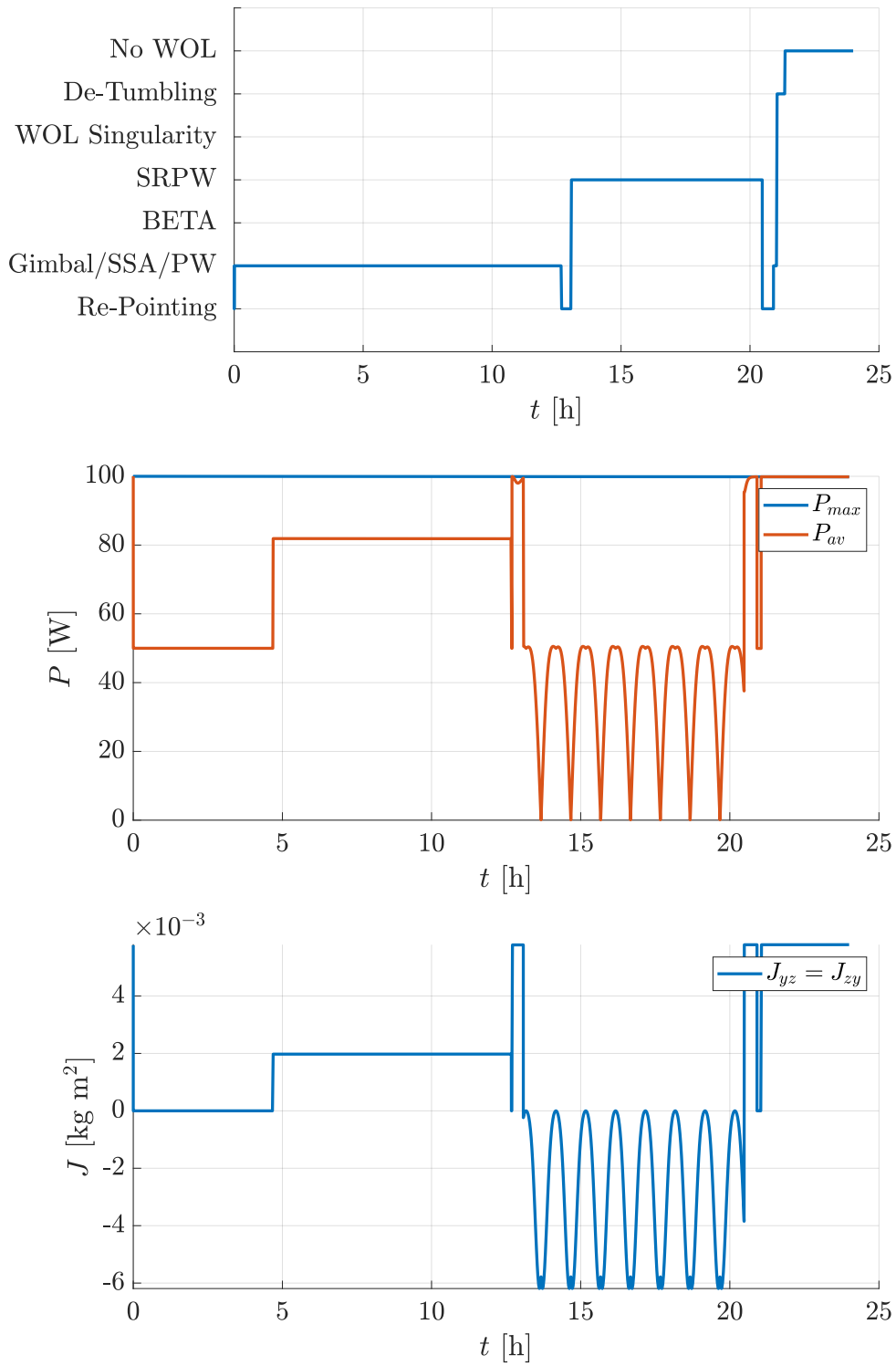
Figure 5.1: Simulation results of the autonomous WOL in a cruising scenario with an assembly of 3 RWS

5.2.2 Pyramid Assembly

The results of the cruising scenario simulation with a pyramid assembly of 4 RWS are presented in *Figure 5.2*. In this case the WOL is completed in $t = 3.15\,$h. The residual momentum is $h = 0.27\,$mNms, the 0.91% of the initial one.

The sequence of strategies is the same as before. However, in this case, the effect they have on the momentum components is the same only when looking at the equivalent momentum. In fact, the actual momentum stored in the wheel will follow a different trend, as can be seen in the figure. In both cases, however, the norm decreases, confirming the fact that the 4 RWS case can be solved as a 3 RWS one. With this particular combination of momentum, the WOL singularity does not occur because the combination of signs that triggers it is never reached.

Looking at mass consumption, figures similar to the previous case can be obtained. In this case, $\Delta m_p = 0.0023\,$g and $\Delta m_{p_{RCS}} = 2.05\,$g and the mass savings is around 99.9%. The moments during which the RCS is less efficient is when it has to generate torques around x and y axes, where 6 RCS thrusters are active at the same time and therefore the low specific impulse of them plays an important role.
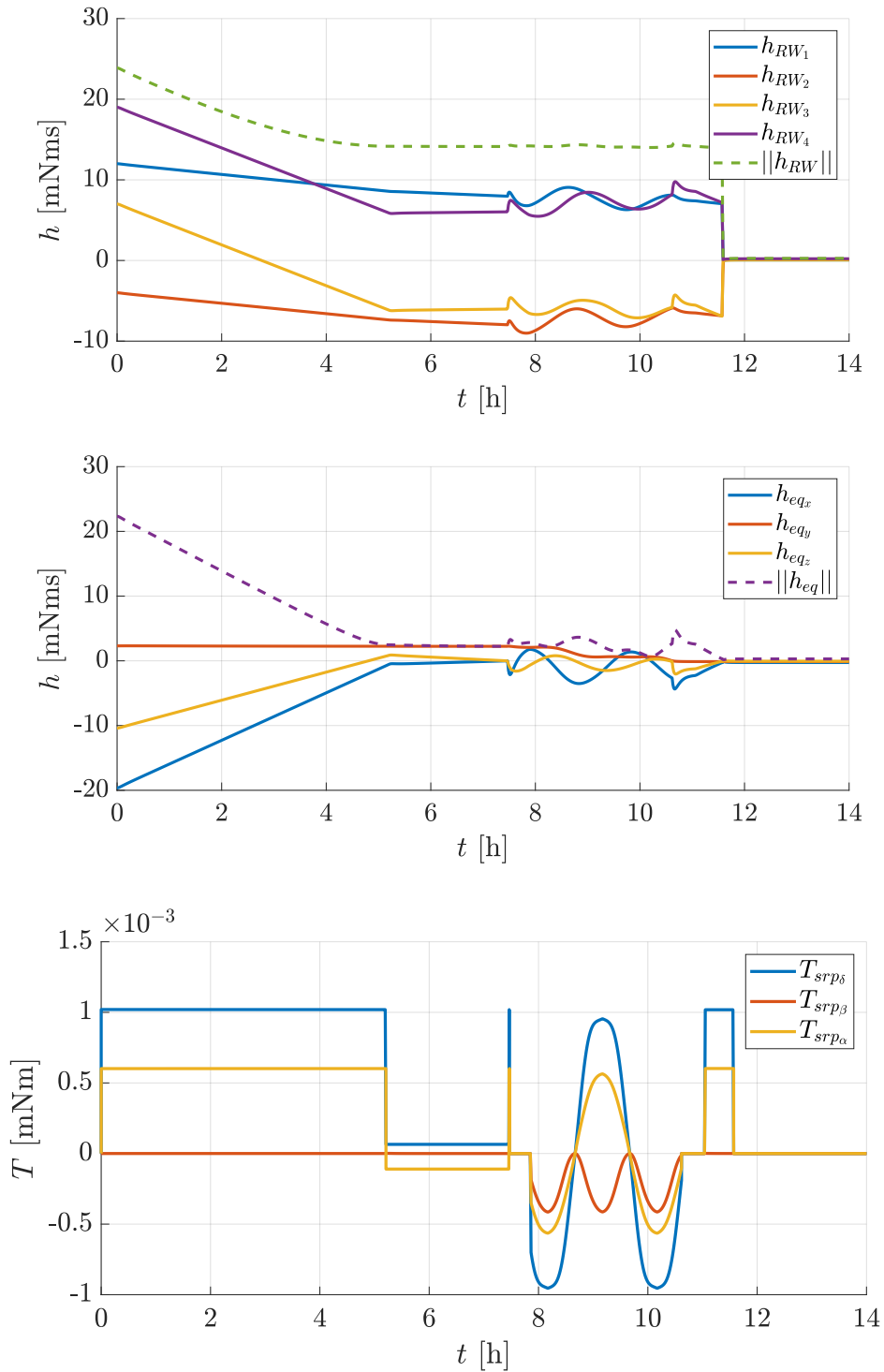
Figure 5.2: Simulation results of the autonomous WOL in a cruising scenario with an assembly of 4 RWS

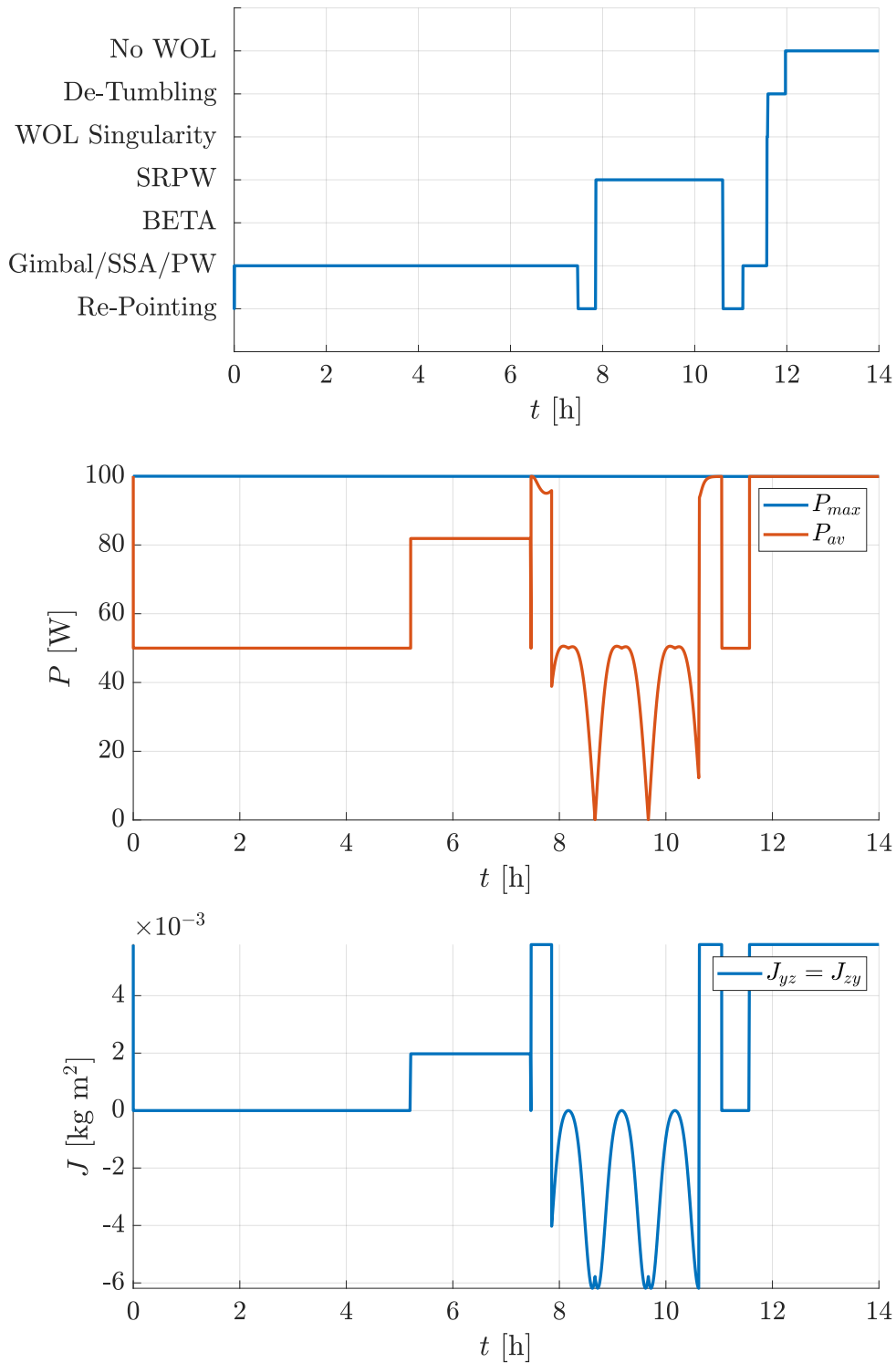Figure 5.2: Simulation results of the autonomous WOL in a cruising scenario with an assembly of 4 RWS

5.3 Coasting Scenario

During the coasting arcs, the SSA, PW and SRPW strategies are employed. The autonomous WOL will be demonstrated, in this case paying attention to the decrease in the power production capabilities and change in the inertia, consequences of the SAS tilting.

5.3.1 Orthogonal Assembly

The results of the simulation, considering a 3 RWS assembly, are presented in *Figure 5.3*. The remaining momentum is the 1.1% of the initial value of $||h_0|| = 21.1$ mNms. The WOL is accomplished in $t = 21.36$ h. As previously stated, the coasting strategies require a much longer time than the cruising ones due to the lightness of the SRP disturbances. However, it is demonstrated that if needed, M-Argo can use one of its coasting arcs, that lasts 24 h, to perform a WOL without any additional consumption of propellant.

The procedure begins with a SSA strategy, followed by a PW after about 5 h, to remove the momentum on x and z. Then, as soon as h_x crosses h_z, the SRPW trajectory is initiated. As it can be seen in the plot, the torque generated by the SAS, expressed in the pointing frame, has oscillatory components on all the axes. However, the component on the β-axis is shifted in magnitude and this results in a net torque effect during the trajectory. The other two components are larger, but they are centered on zero and therefore no momentum is accumulated on δ and α. The WOL closes with a last SSA strategy of some minutes.

The main drawback of using such strategies is the decrease in power production. As it can be seen in the plot, during SSA the power is halved, during PW is around the 80% and in SRPW it oscillates between 0% and 50%. Only during the re-pointing phases, the tilting angles are set to zero and the power produced is equal to the nominal. By carrying out a real-time integration of the power during the simulation, the energy produced is computed to be the 64.8% with respect to the case where no WOL is performed along the same track. This is the price to pay to use these strategies, which are, on the other hand, free of propellant consumption.

Another consequence in the SAS tilting is the change in the inertia properties of the s/c. In particular, when the array is tilted with an angle different than $0°$ or $90°$, the products of inertia assume a non-zero value. This reflects primarily on the control accuracy since the controller is tuned to work with a nominal inertia tensor. However, the tracking controller seems to be robust with respect to the re-distribution of inertia and so this issue does not affect the success of the WOL. The similarity of the J_{yz} plot with P_{av} can be explained by the fact that the reduction coefficient directly depends on the tilting angles, which in turn cause a change in the components of the inertia matrix.

Figure 5.3: Simulation results of the autonomous WOL in a coasting scenario with an assembly of 3 RWS

Figure 5.3: Simulation results of the autonomous WOL in a coasting scenario with an assembly of 3 RWS

5.3.2 Pyramid Assembly

The last case to be studied regards a coasting scenario with an assembly of 4 RWs. The results are presented in *Figure 5.4*.

In this case the remaining momentum percentage is about 1.33%, completing the WOL in about $t = 12\,\text{h}$. The energy produced is 64.5% of the theoretical one.

The procedure in terms of the sequence of strategies is substantially the same as the previous example. However, in this case, it can be clearly noticed the occurrence, at about $t = 11.5$, of the WOL singularity. The equivalent momentum $||h_{eq}||$ has practically reached the zero value, but the actual momentum $||h_{RW}||$ is still high, about $14\,\text{mNms}$. The spin rate is then forcefully decreased bypassing the commanded torque. This action has the effect to dump the actual momentum stored on the wheel and not produce at the same time an attitude drift because the equivalent torque produced by the wheels is zero.

Figure 5.4: Simulation results of the autonomous WOL in a coasting scenario with an assembly of 4 RWS

Figure 5.4: Simulation results of the autonomous WOL in a coasting scenario with an assembly of 4 RWS

5.4 Validation

The astrodynamics simulator that has been presented and the consequent results of the simulations need to be validated through the use of an external simulation framework. CUBORG has been chosen primarily due to its flexibility in terms of modifications and simplicity of use. This numerical toolbox is being developed by the Deep-space Astrodynamics Research & Technology (DART) Team, a research group in Politecnico di Milano specialized in the design of autonomous interplanetary CubeSats [63]. This simulaor is also Simulink-based and uses an arbitrary number of in-house developed libraries with the purpose of performing reliable GNC simulations in many possible CubeSats operative scenarios [12]. The possibility to plug-in new models tailored to one's needs makes it a suitable choice for the purpose of the validation of the WOL strategies.
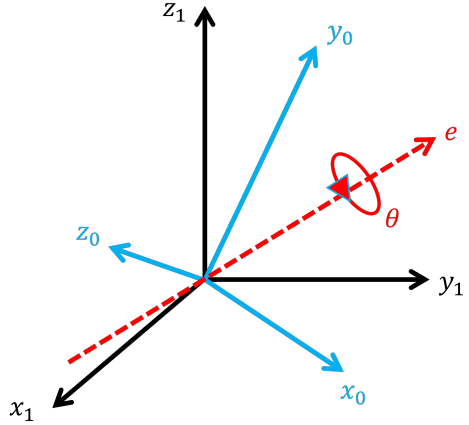
The toolbox relies on many levels on the SPICE information system from Navigation and Ancillary Information Facility (NAIF) [64]. SPICE allows engineers to design missions, plan observations and analyze science data thanks to a team dedicated to the production of high precision, clearly documented and readily used "ancillary information" about several things, such as:

- Position, velocity, size, shape and orientation of planets, satellites, comets, asteroids and spacecraft.

- Orientation of a s/c and its various moving structures.

- Instrument FOV location on a planet's surface or atmosphere.

The software is used, in its MATLAB version Mice, for two main purposes in the context of CUBORG: reading ephemerides and converting quantities from one reference frame to another one. The ephemerides produced with SPICE are used both for the propagation of celestial bodies and as potential data loaded onboard the s/c. In this way, the same WOL simulations performed in the previous section can be repeated in a gravity field that comprises all the planets of the solar system, whose exact locations at each time are extracted from the generated ephemeris. Moreover, the information on the pointing vector and reference thrust can be stored as well in form of ephemerides in the onboard memory.

The goal is to replicate the WOL simulation presented in *subsection 5.2.1*, accounting also for the sensors noises. To this aim, the sensors data in *Figure 2.7* is inserted into the standard CUBORG models for the STR and IMU. The FSS measure the Sun direction but this information is not needed because the knowledge of the pointing frame at each instant is loaded into the onboard memory in form of ephemeris.

The kinematics in CUBORG are expressed with *quaternions*, which are a minimum set of attitude parameters that can be computed starting from the Euler's axis and angle, as reported in (5.3). The control is carried out with a standard CUBORG block, a slewing controller based on the quaternion error.

$$q = \begin{bmatrix} \hat{q} \\ q_x \\ q_y \\ q_z \end{bmatrix} = \begin{bmatrix} \cos \frac{\theta}{2} \\ e_x \sin \frac{\theta}{2} \\ e_y \sin \frac{\theta}{2} \\ e_z \sin \frac{\theta}{2} \end{bmatrix} \tag{5.3}$$

Regarding the developed blocks, the RWS dynamic model and the gimballed thruster model are plugged into the actuators section of the simulator. The guidance algorithms for the attitude and the gimbal are placed into the GNC section, as well as the SM.

The same situation of *subsection 5.2.1* is simulated. The angular momentum trend is depicted in *Figure 5.5*, compared against the ideal one. The strategies are almost practically replicated with the same sequence and duration, apart from the final ones, where an additional BETA plus Gimbal strategy are required to complete the WOL. For this reason, the off-loading time increases to 2 h, while the residual momentum is about 0.5 mNms, being this simulation closer to reality and therefore inherently less precise.

It is possible to notice that the curves are not as smooth as before due to the presence of the sensors' noises. The measured rate and quaternion, carried out respectively by the IMU and STR, are shown in *Figure 5.6* and compared to the ideal WOL case. As expected, the STR measure presents much lower oscillations than the IMU due to its high precision, which is on the scale of arcseconds.

From these comparisons, it is possible to state that the astrodynamics simulator can be considered validated, at least from the rotational dynamics viewpoint. The simulation in CUBORG performed the WOL with the same results of the ideal case, the only differences can be re-conducted to the presence of noises in the system.
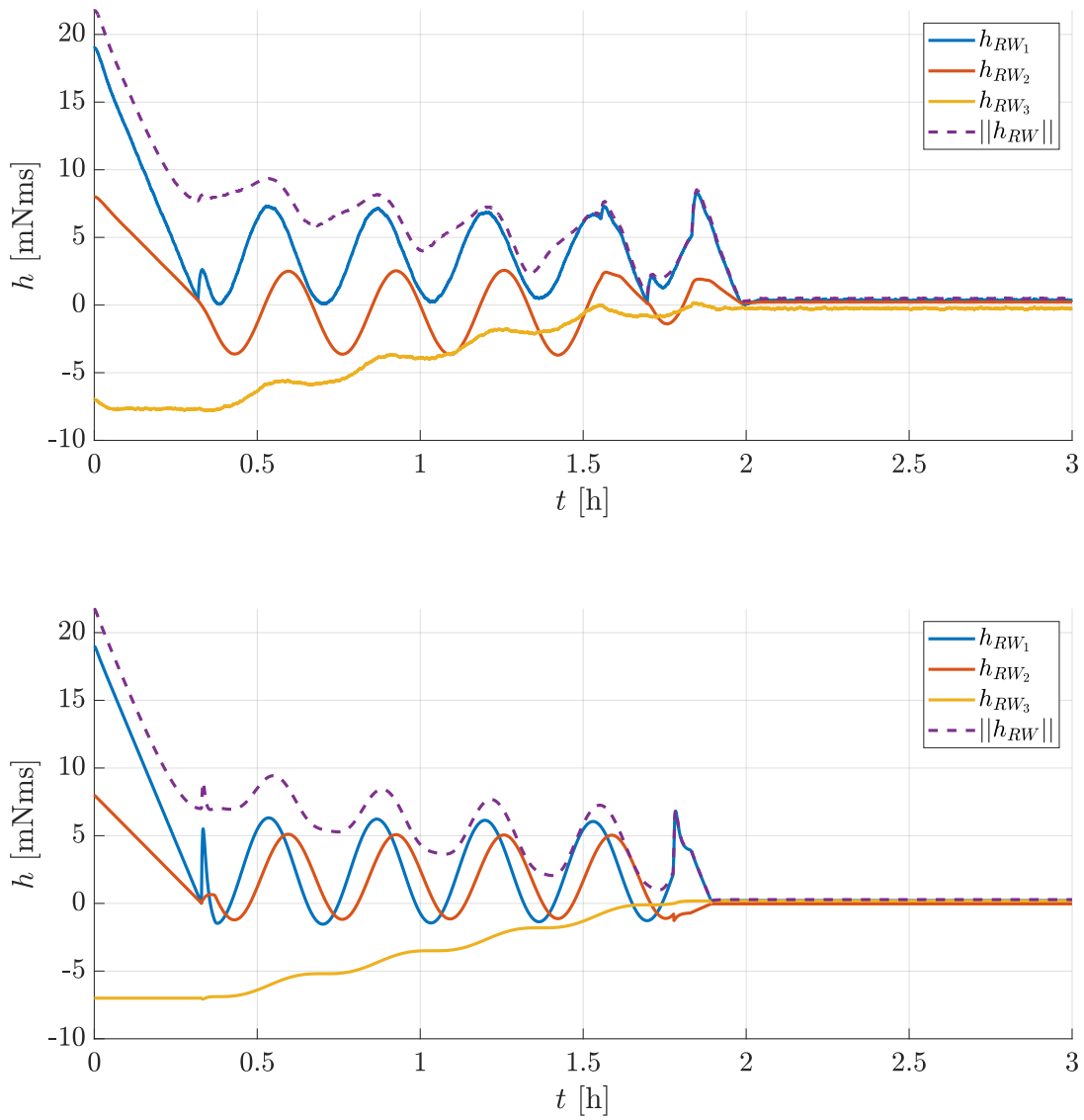
Figure 5.5: Angular momentum trend in the same scenario simulated with CUBORG and with the original simulator
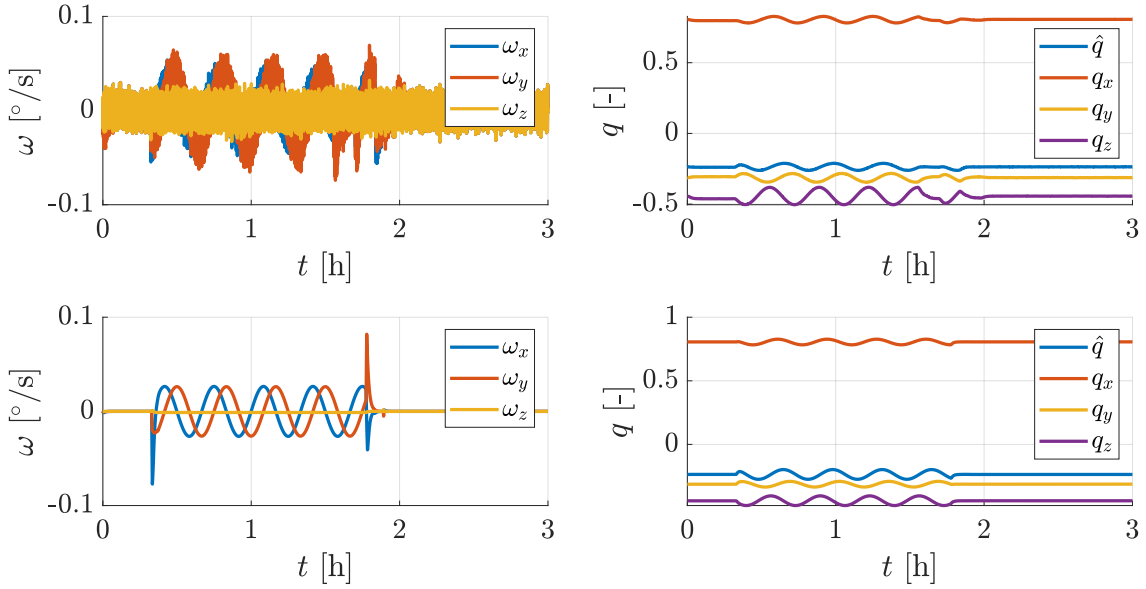
Figure 5.6: Angular rate and quaternion trends in the same scenario simulated with CUBORG and with the original simulator

The ultimate objective of the cruising strategies is to perform the WOL without affecting the mission trajectory. As previously said, during the re-pointing and de-tumbling phases the thruster is switched off and therefore is not following the reference thrust level. When the WOL is being carried out, on the other hand, it is switched on but is never aligned to the reference pointing vector $\hat{\boldsymbol{\alpha}}$. instead, it is directed along $\hat{\boldsymbol{g}}$ and generates a thrust force computed by the algorithm previously seen in (3.5). To check that the trajectory is followed properly and to validate the astrodynamics model also in terms of translational dynamics, three different cases are compared in *Figure 5.7*.

- *No WOL*. This is the nominal trajectory, propagated in CUBORG without performing any WOL. The body frame is always coincident with the pointing frame and the thrust is always equal to the reference one and pointing along $\hat{\boldsymbol{\alpha}}$.

- *WOL*. This is the trajectory followed while performing the WOL in the astrodynamics simulator presented in *chapter 4*.

- *WOL_CUBORG*. This case is equal to the previous one, but CUBORG is used for the simulation.
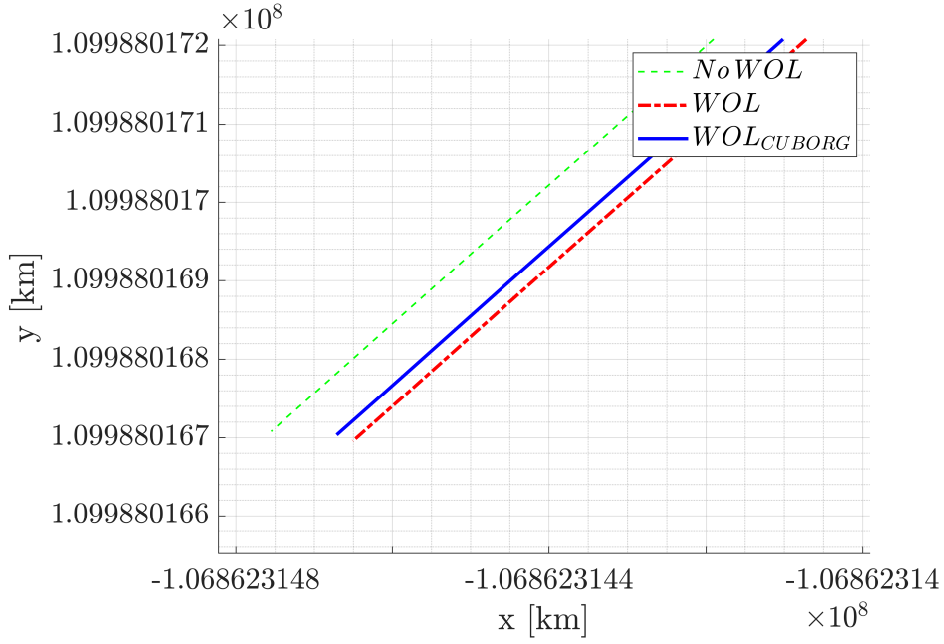
Figure 5.7: Comparison of the trajectory

Setting 3 h for the total simulation time, the final position errors of the three cases are reported in *Table 5.2*. The absolute and relative errors between two cases *a* and *b* are computed using (5.4).

$$\epsilon_{abs}^{[a,b]} = \left|\left|\boldsymbol{x}(t_f)^{[a]} - \boldsymbol{x}(t_f)^{[b]}\right|\right|$$

$$\epsilon_{rel}^{[a,b]} = \frac{\epsilon_{abs}^{[a,b]}}{x_{tot}} \tag{5.4}$$

$$\text{where} \quad x_{tot} = \left|\left|\boldsymbol{x}(t_f)^{[No\,WOL]} - \boldsymbol{x}(t_0)^{[No\,WOL]}\right|\right|$$

	No WOL vs *WOL*	*No WOL* vs WOL_{CUBORG}	*WOL* vs WOL_{CUBORG}
$\epsilon_{abs}\,[\text{m}]$	111	106	37
$\epsilon_{rel}\,[10^{-7}]$	3.43	3.27	1.13

Table 5.2: Absolute and relative errors in the trajectory during a WOL of 3 h

The displacement of the trajectory during the WOL from the nominal path is $\approx 100\,\text{m}$, that in terms of relative error results to be on the order of $\approx 10^{-7}$. Therefore, the WOL

can be performed without any significant risk of deviating from the nominal trajectory. This is valid for both the simulators used, which means that the astrodynamics simulator can be considered validated also from the translational dynamics viewpoint. Considering the same WOL situation, the difference between the two is in fact ≈ 40 m, that can be re-conducted to the presence in CUBORG of a much different gravity field, that considers not only the Sun but all the planets of the solar system.

5.5 Sensitivity Analysis

The simulations of the strategies in 4 specific cases, even if generated from random ICs of angular momentum, can not be considered enough to state that the algorithms are valid and successful for any scenario. For this reason, a *sensitivity* analysis must be carried out. This analysis will deal only with the cruising strategies because they are the ones that should be considered as the first choice due to the low WOL duration and the fact that they do not put power constraints on the system. However, it is possible to replicate the same studies also for the coasting strategies.

The two main uncertainties to face are the initial angular momentum when the WOL is initiated and the displacement of the COM from the geometric center.

5.5.1 Initial Momentum

As first step, a proper random set of ICs must be generated. To have a meaningful comparison of the results, a constraint has to be put on the norm of h_0, in such a way to uniform the initial "energy" of the system. Moreover, an additional constraint is that at least one RW has to be saturated.

In the case of a 3 RWs assembly, the procedure to generate the samples follows (5.5). Firstly, the saturated value h_{max} is assigned to one axis generating a random sign. Then, since the norm is fixed, the other two components can be extracted from the circumference whose radius is equal to ρ, the root square of the difference between the norm and h_{max}. Therefore, a random *angle* is generated and the two momentum components will be the coordinates of the point on the circumference associated with that angle. The function used in the equation is "randi", which allows computing a uniformly distributed set of integer numbers in the provided range. It is easy to verify that the norm of the three components

is equal to $||\boldsymbol{h}||$.

$$
\begin{aligned}
h_1 &= \pm h_{max} \\
h_2 &= \rho \sin \psi \\
h_3 &= \rho \cos \psi \\
\text{where} \quad \rho &= \sqrt{||\boldsymbol{h}||^2 - h_1^2} \\
\psi &= \mathrm{randi}(-180°, 180°)
\end{aligned}
\tag{5.5}
$$

The previous equation generates a set of three angular momentum components with the aforementioned constraints. However, these components must be assigned to random axes if the most general situation is sought. To this aim, the initial momentum is obtained using (5.6), where the function "randperm" allows to generate a random permutation of integers in the provided range.

$$
\boldsymbol{h}_0 = \begin{cases} h_x = h_i \\ h_y = h_j \\ h_z = h_k \end{cases} \quad \text{where} \quad i, j, k = \mathrm{randperm}(1, 3)
\tag{5.6}
$$

The equations are iterated for a total of $n = 500$ samples, considering as norm constraint the value of $||\boldsymbol{h}_0|| = 25 \, \mathrm{mNms}$ and for saturation limit the usual value of $h_{max} = 19 \, \mathrm{mNms}$. To have a visualization of the sample population, one could think of the problem as the generation of random 3D coordinates on a sphere surface with a radius equal to $||\boldsymbol{h}_0||$. The constraint on the saturation of one coordinate can be seen as the intersection of this sphere with the planes associated with h_{max}. Therefore, the random samples take the shape distribution depicted in *Figure 5.8*.

The sensitivity analysis results, considering the aforementioned data, are reported in *Figure 5.9*. The two figures of merit are the norm of the final momentum and the total duration of the WOL procedure. As it can be seen, all the 500 samples complete successfully the WOL, regardless of the initial momentum values. The samples that fall on the right side of the plot are the ones associated with the initial largest component on the z-axis, for which the slower BETA strategy is used. In general, it is possible to state that the WOL during cruising takes a mean time of about 3.1 h and dump the momentum to a norm of 0.28 mNms.

For the same sample data, it is convenient to generate Empiric Cumulative Distribution Function (ECDF) to show the probability for the cruising strategies to complete the WOL under specific thresholds. For instance, looking at *Figure 5.10*, it is possible to see that in 80% of the cases the WOL is completed in less than 4 h and leaving as residual momentum a norm of 0.3 mNms.
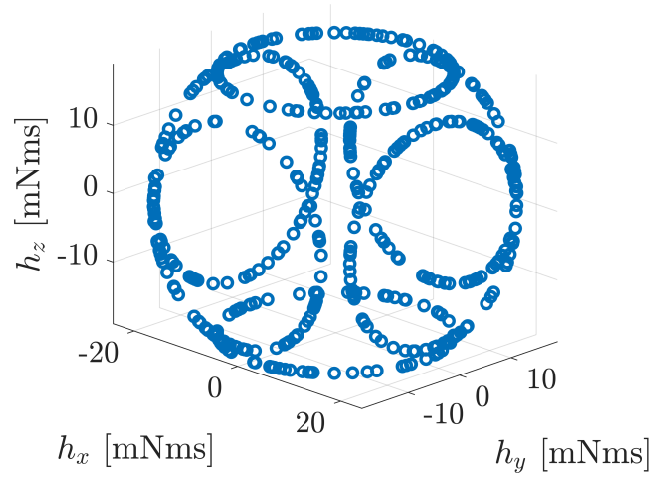
Figure 5.8: Population of 500 samples of initial angular momentum triplets
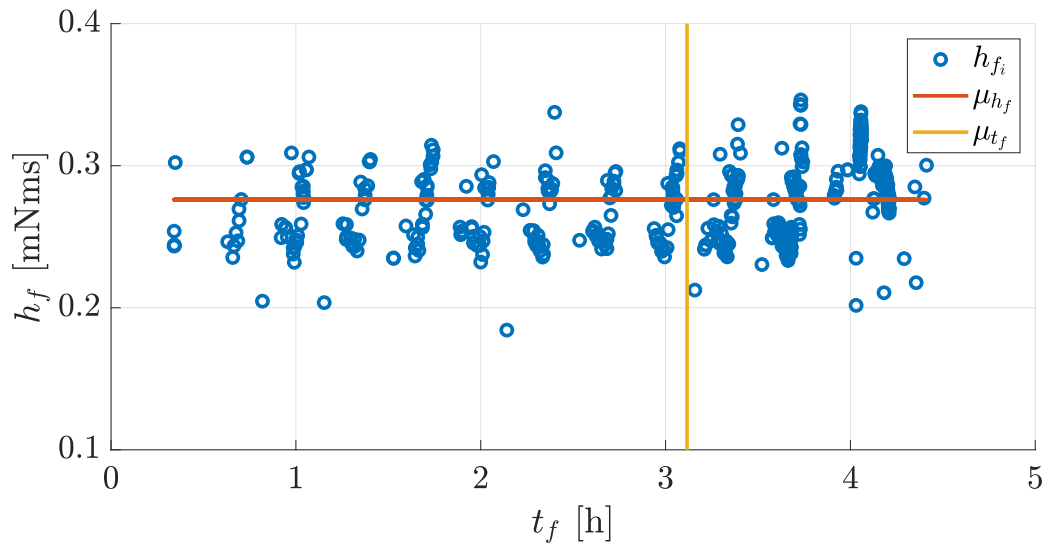
Figure 5.9: Results of the sensitivity analysis for the initial angular momentum
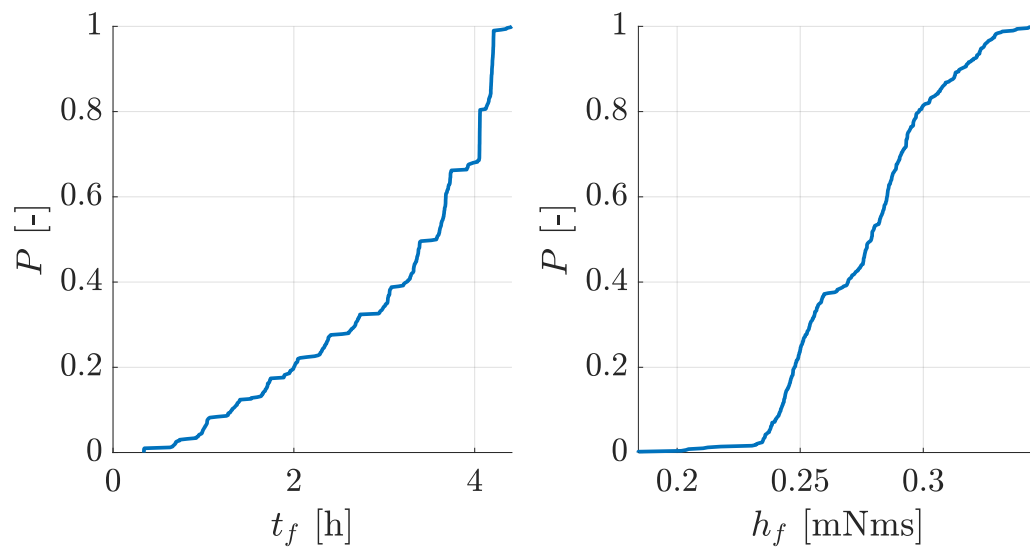
Figure 5.10: ECDF of the total WOL time and norm of the final momentum for different initial momentum

5.5.2 COM Displacement

In *chapter 3*, for the strategies development, it has been assumed that the COM was coincident with the geometric center of the body. This assumption will be now removed and parasitic torques will arise due to the fact that the thruster location will be given by the sum of its geometric position with the COM displacement. The thruster torque expression, defined previously in (3.6), will be therefore modified in (5.7).

$$
\boldsymbol{d}_{thr} = \begin{bmatrix} 0 \\ 0 \\ -\frac{c}{2} \end{bmatrix} + \boldsymbol{d}_{\odot} = \begin{bmatrix} x_{\odot} \\ y_{\odot} \\ z_{\odot} - \frac{c}{2} \end{bmatrix}
$$

$$
\boldsymbol{T} = \boldsymbol{d}_{thr} \times F\hat{\boldsymbol{g}}_{b} = F \begin{bmatrix} y_{\odot}\sqrt{1-(\sin\theta_1)^2-(\sin\theta_2)^2} - (z_{\odot}-\frac{c}{2})\sin\theta_2 \\ (z_{\odot}-\frac{c}{2})\sin\theta_1 - x_{\odot}\sqrt{1-(\sin\theta_1)^2-(\sin\theta_2)^2} \\ x_{\odot}\sin\theta_2 - y_{\odot}\sin\theta_1 \end{bmatrix}
$$

(5.7)

The Gimbal strategy algorithm in (3.8) fixes one angle and computes the other based on the ratio between the momentum values that must be dumped. The same ratio can be computed also in the case of COM displacement, but the resulting implicit equation can not be solved analytically to find one angle as a function of the other. However, as demonstrated in (5.8), the g_z component of the gimbal vector can be approximated to 1 because the angles are always under $5°$.

$$
g_z = \sqrt{1-(\sin\theta_1)^2-(\sin\theta_2)^2} = \sqrt{1-2(\sin 5°)^2} = 0.9924 \approx 1 \tag{5.8}
$$

Employing this approximation, the momentum ratio is then given by (5.9). If the COM displacement is assumed to be known with a certain degree of accuracy, the second angle can be easily computed inverting the expression and the Gimbal strategy can be still exploited without risks.

$$
\frac{h_y}{h_x} \approx \frac{T_y}{T_x} = \frac{-x_{\odot} + \left(z_{\odot} - \frac{c}{2}\right)\sin\theta_1}{y_{\odot} - \left(z_{\odot} - \frac{c}{2}\right)\sin\theta_2} \tag{5.9}
$$

The generalized algorithm is therefore the one expressed in (5.10). If there is no COM displacement, the equations becomes equal to the ideal ones reported in (3.8).

$$|h_x| > |h_y| \rightarrow \begin{cases} \theta_2 = -\theta_{max} \operatorname{sgn}(h_x) \\ \\ \theta_1 = \arcsin\left(\dfrac{\left(y_\oplus - \left(z_\oplus - \dfrac{c}{2}\right)\sin\theta_2\right)\dfrac{h_y}{h_x} + x_\oplus}{z_\oplus - \dfrac{c}{2}} \right) \end{cases}$$

$$\text{(5.10)}$$

$$|h_x| < |h_y| \rightarrow \begin{cases} \theta_1 = \theta_{max} \operatorname{sgn}(h_y) \\ \\ \theta_2 = \arcsin\left(\dfrac{\left(x_\oplus - \left(z_\oplus - \dfrac{c}{2}\right)\sin\theta_1\right)\dfrac{h_x}{h_y} + y_\oplus}{z_\oplus - \dfrac{c}{2}} \right) \end{cases}$$

The effect that this issue has on the BETA strategy is instead more pronounced and difficult to solve. *Figure 5.11* shows how a COM displacement of 5 mm on all the axes makes the dumping of even a low quantity of momentum on z-axis to cause the other two axes to approach the saturation.
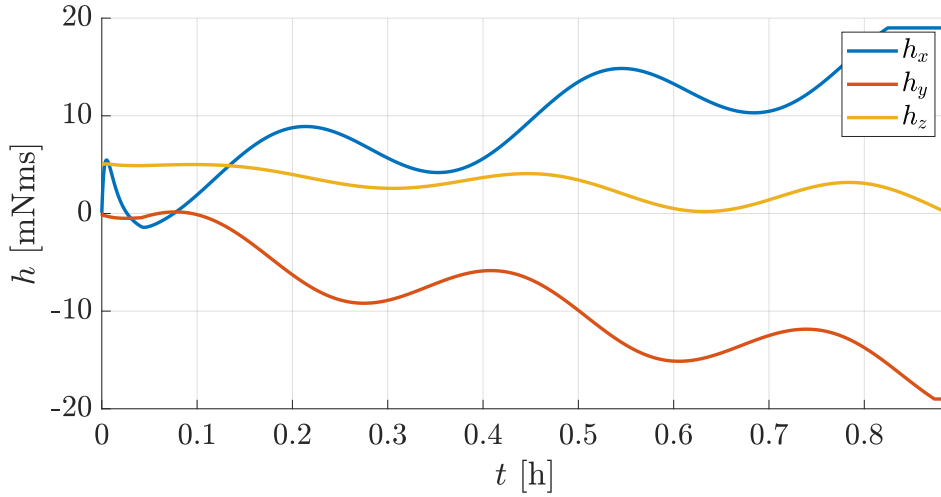
Figure 5.11: Angular momentum trend during BETA strategy in case of COM displacement

The problem can be solved by shifting the gimbal angles trajectory of specific offset angles in such a way to bring the gimbal vector $\hat{g}$ aligned with the vector linking the COM with

the thruster position. The two offset angles $\Delta\theta_1$ and $\Delta\theta_2$ can be computed using (5.11).

$$\Delta\theta_1 = \arctan\left(\frac{x_\oplus}{z_\oplus + \frac{c}{2}}\right)$$
$$\Delta\theta_2 = \arctan\left(\frac{y_\oplus}{z_\oplus + \frac{c}{2}}\right)$$

(5.11)

If the COM displacement can be estimated, it is therefore possible to apply also the BETA strategy without consequences by adding these offset angles to the gimbal angles law in (3.9).

After the correction of the algorithms to take into account this uncertainty, it is possible to perform a final analysis and check the overall robustness of the WOL strategies to both random initial momentum and random displacement of the COM.

While the initial momentum sampling follows the same method of before, the samples of the COM vector $d_\oplus$ are generated using (5.12), imposing as constraint for the norm ρ the value of 1.2 cm. In this case, the entire sphere surface is spanned and the samples are extracted from the coordinates on the surface according to random elevation and azimuth angles.

$$d_\oplus = \begin{cases} x_\oplus = \rho\cos\psi\cos\gamma \\ y_\oplus = \rho\cos\psi\sin\gamma \\ z_\oplus = \rho\sin\psi \end{cases} \quad \text{where} \quad \begin{matrix} \psi = \text{randi}(-90°, 90°) \\ \gamma = \text{randi}(-180°, 180°) \end{matrix}$$

(5.12)

The sensitivity analysis is again carried out with $n = 500$ samples. When the WOL takes more than 10 h, it is considered a failure. This occurs in 4 cases, which means a percentage of success of 99.2%. The COM location of each sample is reported in *Figure 5.12*, where the red dots are the samples that lead to a failure. On the right, the statistics of the failures, reported in *boxplots*, show that they are associated with the cases where the highest COM displacement is on the y-axis. This can be explained by the fact that the largest inertia components are around axes perpendicular to y, where the control is, in fact, more critical.

As it can be seen in *Figure 5.13*, for the successful cases the mean final angular momentum is around 0.26 mNms with a total WOL duration of about 3.5 h. The mean values are close to the results of the previous analysis, therefore the corrections made to the algorithms to account for the COM shift can be considered correct and validated.

For completeness, also the ECDF for these analysis are reported in *Figure 5.14*. It is possible to notice that the curves resemble a normal distribution with mean and standard deviation equal to the ones computed from the resulting data.
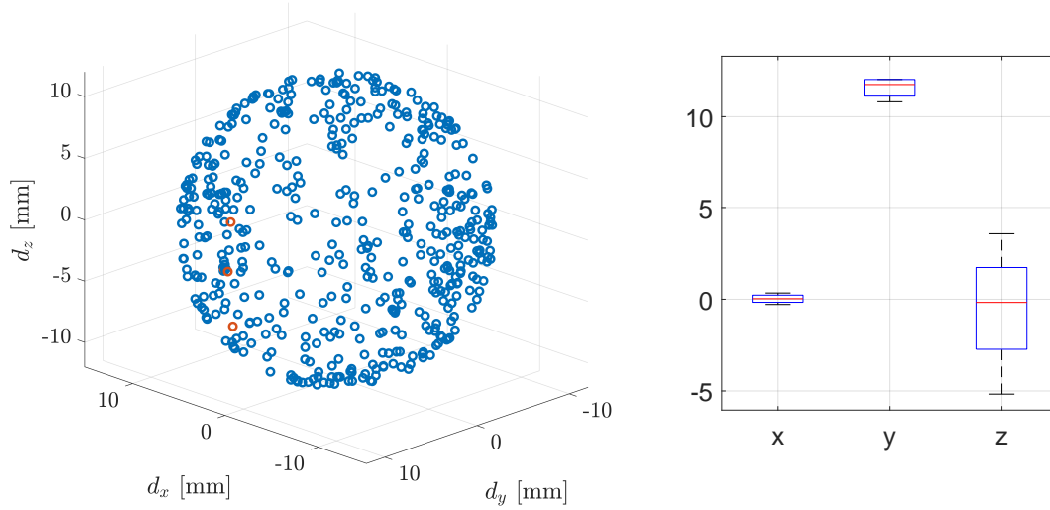
Figure 5.12: Population of 500 samples of com location with respect to the geometric centre and statistic boxplots of the failures
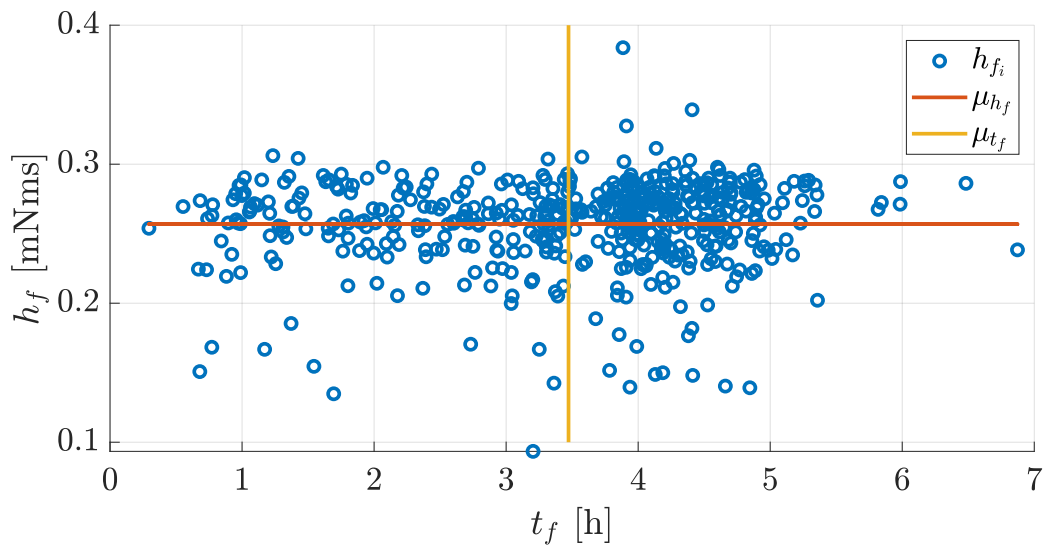
Figure 5.13: Results of the sensitivity analysis for the com displacement
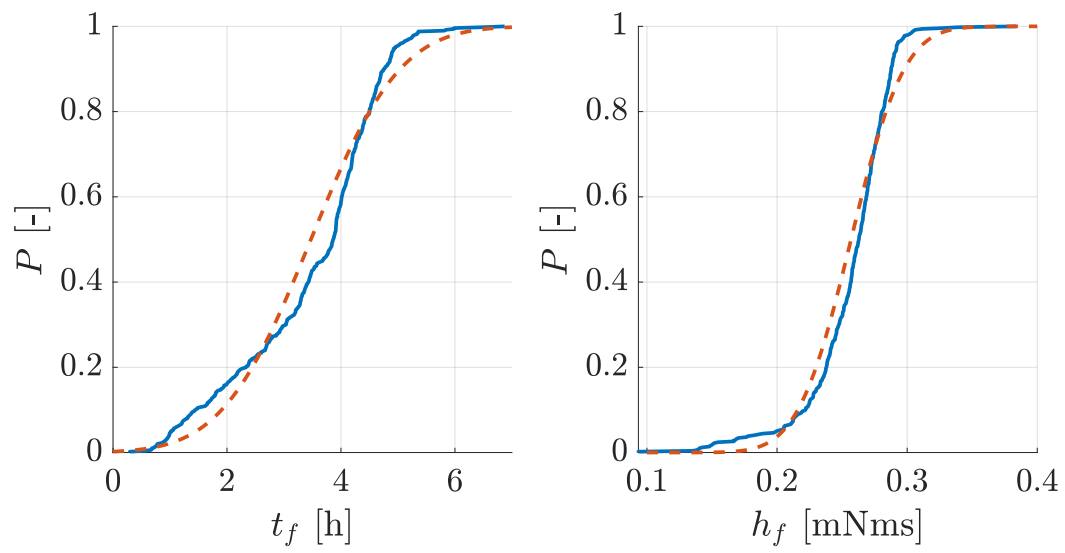
Figure 5.14: ECDF of the total WOL time and norm of the final momentum for different COM displacements

6

Conclusions

F-ROM the accurate description of the algorithms and of the case study under consideration, an astrodynamics simulator was developed to perform testing of the WOL strategies on M-Argo platform. The results allow to answer to the original research question that has been posed in *section 1.4*.

The simulation campaigns of the previous chapter demonstrated the feasibility of the developed techniques in performing the WOL, under different deep-space scenarios and initial conditions, in full autonomy. When coming to uncertainties, the algorithms are robust and can still accomplish the goal with mild differences, that in any case do not affect the mission operations nor the trajectory.

6.1 Lessons Learned

All the presented strategies require the use either of a gimbal mechanism on the main thruster, or a SADM that can deferentially tilt the SAS. The potentially higher cost that these devices could bring is counter-balanced by the fact that the architecture no more need dedicated momentum-management actuators, such as RCS and Magnetotorquers. This is beneficial from the design viewpoint both in terms of mass and volume savings and general efficiency. The additional propellant that the main thruster should provide for the WOL is a very small percentage of the theoretical one that the RCS requires, due to the former's typical higher specific impulse. In the case of coasting strategies, the mass is completely saved, in exchange for a reduced power production capability.

These advantages, coupled with the possibility to completely automate these techniques, are huge advantages when looking at the future deep-space missions based on miniaturized

architectures, such as the ones provided by the CubeSats. It seems that the space industry is becoming more and more biased in favor of this paradigm, and the WOL techniques presented can be considered a promising and effective way to expand both the capabilities and the lifetime of such satellites.

The strategies can also be used as the last resource in case of failure of RCS or Magneto-torquers in current active missions, to still allow the de-saturation of the RWS and re-gain control of the satellite. In fact, even if they have been demonstrated on M-Argo, they can be still employed for any satellite with the proper scaling-up of the thrust level and of the SAS surface, as well as with a tuning of the parameters used in the simulations.

The techniques are valid not only for the two cases of standard orthogonal and pyramid RWS assemblies but actually for any kind of configuration because it is just a matter of equivalent inertial momentum.

When coming to the specific case study, it has been shown that M-Argo is able to remove completely the momentum stored on its wheels, regardless of the saturated axis. The WOL can be performed during one of the cruising arcs, with a duration that is under 4 h in most of the cases. The impact on the overall duration of the cruising arc, which is of 6 days, is therefore just 2.8%. The trajectory error after a typical WOL of 3 h is of about $\approx 100\,\text{m}$, that can be easily fixed with slight corrections on the thrust. If the WOL is performed during coasting arcs, each one lasting 1 day, the whole arc will be likely entirely devoted to the de-saturation because the strategies take several hours. It is important therefore to choose an arc where high power-demanding operations are not expected or can be skipped and postponed to the following coasting arc. In this case, however, the advantage is the propellant-less de-saturation, which enables the saving of a consistent amount of mass.

In particular, a possible way to estimate the overall impact of the de-saturation on M-Argo mission could be to consider the swirl torque treated in *subsection 1.3.2*. The gridded ion engine of M-Argo falls in the class of mN thrust level, therefore the expected parasitic torque will be around $0.2\,\mu\text{Nm}$. Considering the trajectory to 2010-UE51, the total accumulated momentum on the z axis is obtained using (6.1), from the total thrusting time t_{thr}, that is basically the sum of all the 6-days cruising arcs along the entire TOF. The total number of WOLs about the z axis can be therefore approximated to be less than 500.

$$
\begin{aligned}
t_{thr} &= \frac{6}{7}\,\text{TOF} = 498\,\text{d} \\
h_{swirl} &= T_{swirl}\,t_{thr} = 8.6\,\text{Nms} \\
n_{WOL} &= \frac{h_{swirl}}{h_{max}} \approx 453
\end{aligned}
\tag{6.1}
$$

According to *Figure 6.1*, a de-saturation of the z-axis takes approximately 4 h and requires an additional amount of propellant with respect to the one consumed by the thruster of $\approx 0.003\,\text{g}$ if performed with the BETA strategy or $\approx 0.9\,\text{g}$ if performed with RCS.
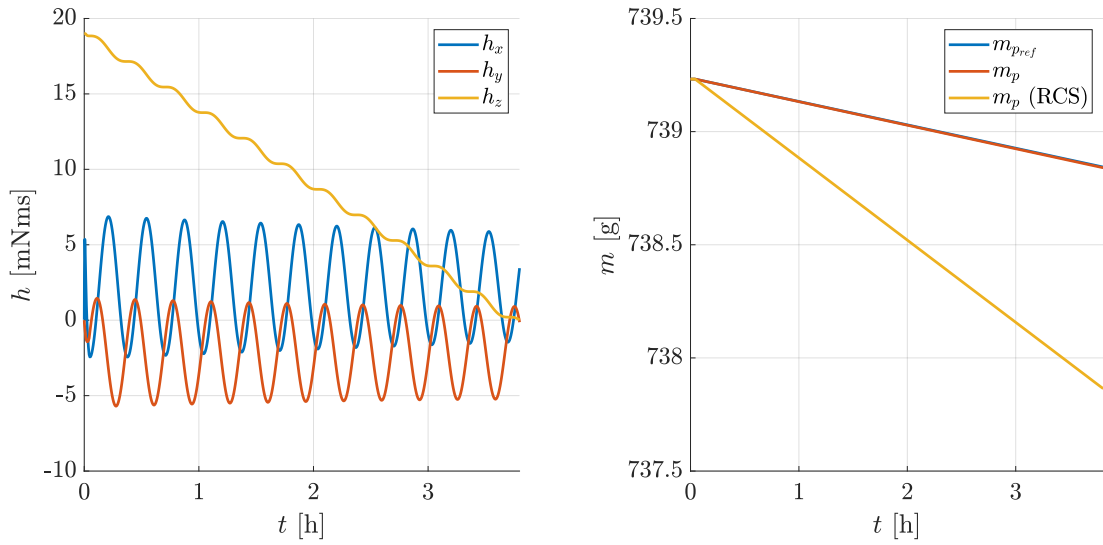
Figure 6.1: De-saturation of *z* axis employing the ʙᴇᴛᴀ strategy and correspondent propellant mass consumption

Therefore, the conclusion is that for the M-Argo mission, the expected additional consumption of propellant to account for the swirl torque can be reduced from a total of $453 \times 0.9 = 407.7\,\mathrm{g}$ to just $453 \times 0.003 = 1.36\,\mathrm{g}$, employing the ʙᴇᴛᴀ strategy instead of de-saturating with the ʀᴄs. This results in a mass savings of 99.6%.

6.2 Future Works

This work can be used as a starting point for future developments or can just be taken as input for the creation of a general toolbox of techniques that can be tailored to any specific mission under consideration.

It could be interesting to check if these strategies can be also employed with other deep-space missions, or in general with any satellite characterized by a gimballed thruster or tiltable sᴀs. To this aim, the proposed astrodynamics simulator has been developed taking into account from the beginning the possibility to change the input data and tune the control parameters with a high degree of flexibility.

A possible open point that could be treated regards the issue discussed in *subsection 1.3.1* for the dead-zone that any reaction wheel experiences when the spin rate approaches the zero value. During strategies that involve periodic attitude motions, the components of

momentum that are not being de-saturated experience oscillations that could make this issue becomes a criticality for the success of the wol.

The coasting and the cruising strategies have been presented and simulated in a complete decoupled way, but one could think of using them at the same time to have a faster or in some cases more efficient de-saturation. The most straightforward example is given by a Gimbal strategy coupled with ssa. The two strategies can be super-imposed to de-saturate at the same time all of the three axes, the x and y with the thruster and the z with the sa tilting. An exploration of the possible combined strategies could be carried out, with special regards to the power availability, that inevitably has to degrade.

Moreover, the ssa and pw strategies could be merged into a single strategy, where an optimal value for the tilting angles should be sought through a minimization process, in order to de-saturate two axes and ending with zero momentum at the same time. This procedure would require an even more accurate model of srp to be used for onboard estimation, and maybe also the possibility to change the optical properties of the sp in real-time.

At last but not least, the most interesting and challenging future work would be represented by the actual testing of these strategies, first with a hardware-in-the-loop integration, and then on an actual in-orbit demonstration. The candidate that should be considered as the straightforward choice is M-Argo, but eventually the strategies could also be tested on other CubeSat platforms such as the deep-space satellites presented in *section 1.1*. Testing of the wol strategies based on the gimballed thrust are indeed programmed to be carried out in the Lunar IceCube mission [5]. This demonstration could be useful to start thinking about a scaling-up in order to apply the same concepts to larger satellites. A possible candidate between the active missions of esa is BepiColombo, whose transfer module is characterized by 4 gimballed ion thrusters and large solar wings. The gimbal in that case is mainly used to correct the thrust vector due to com evolution along the journey to Mercury, while rcs are used for de-saturation [65]. Another alternative that could be considered is the Solar Orbiter mission, whose sas design is, to a large extent, based on the design of BepiColombo [66]. In this case, the close proximity to the Sun could be ideal to test the strategies based on srp. Eventually, the concepts could be applied to any future mission, integrating the s/c architecture with the required components, but on the other hand ending with a design that is free of dedicated momentum-management actuators and potentially more compact and efficient.

Bibliography

[1] Cal Poly CubeSat Laboratory (CPCL). *The CubeSat Program*. URL: https://www.cubesat.org/about (cit. on p. 1).

[2] Nanosats Database. *Figures*. URL: https://www.nanosats.eu/ (cit. on p. 2).

[3] Andrew Klesh and Joel Krajewski. "Marco: Cubesats to mars in 2016." In: (2015) (cit. on p. 2).

[4] Brandon Stiltner et al. "Cold Gas RCS for the NEA Scout CubeSat." In: *AIAA Young Professionals Symposium*. 2017 (cit. on p. 3).

[5] Benjamin K Malphrus et al. "The lunar icecube em-1 mission: Prospecting the moon for water ice." In: *IEEE Aerospace and Electronic Systems Magazine* 34.4 (2019), pp. 6–14 (cit. on pp. 3, 112).

[6] Nanosats Database. *Lunar IceCube*. URL: https://www.nanosats.eu/sat/lunar-icecube (cit. on p. 3).

[7] A. Romero Calvo, J. Biggs, and F. Topputo. "Attitude Control For the LUMIO CubeSat in Deep Space." In: *70th International Astronautical Congress (IAC 2019)*. 2019, pp. 1–13 (cit. on pp. 4, 7, 77).

[8] Roman Kruzelecky et al. "Vmmo lunar volatile and mineralogy mapping orbiter." In: 48th International Conference on Environmental Systems. 2018 (cit. on p. 4).

[9] Hannah R Goldberg et al. "The Juventas CubeSat in Support of ESA's Hera Mission to the Asteroid Didymos." In: (2019) (cit. on p. 4).

[10] Fabio Ferrari et al. "Preliminary mission profile of Hera's Milani CubeSat." In: *Advances in Space Research* 67.6 (2021), pp. 2010–2029 (cit. on p. 4).

[11] ESA. *M-Argo: Journey of a suitcase-sized asteroid explorer*. Feb. 2021. URL: https://www.esa.int/Enabling_Support/Space_Engineering_Technology/Shaping_the_Future/M-Argo_Journey_of_a_suitcase-sized_asteroid_explorer (cit. on pp. 4, 18).

[12] DART. *A CUBesat ORbit and GNC tool*. Politecnico di Milano, 2021 (cit. on pp. 5, 95).

[13] Charles Grassin. *Reaction Wheel Attitude Control*. URL: https://charleslabs.fr/en/project-Reaction+Wheel+Attitude+Control (cit. on p. 6).

[14] David S Bayard. "An optimization result with application to optimal spacecraft reaction wheel orientation design." In: *Proceedings of the 2001 American Control Conference.(Cat. No. 01CH37148)*. Vol. 2. IEEE. 2001, pp. 1473–1478 (cit. on p. 7).

[15] Zuliana Ismail and Renuganth Varatharajoo. "A study of reaction wheel configurations for a 3-axis satellite attitude control." In: *Advances in Space Research* 45.6 (2010), pp. 750–759 (cit. on p. 7).

[16] NASA. *State of the Art of Small Spacecraft Technology*. Oct. 2020. URL: https://www.nasa.gov/smallsat-institute/sst-soa-2020 (cit. on pp. 8, 9).

[17] Enpulsion. *NANO Datasheet*. URL: https://www.enpulsion.com/order/enpulsion-nano/ (cit. on p. 9).

[18] ThrustMe. *NPT-30 Datasheet*. URL: https://satsearch.co/products/thrustme-npt30-i2-1u-electric-propulsion-system (cit. on p. 9).

[19] Satt Paris-Saclay. *Successful space test for the first electric iodine propulsion system!* URL: https://satt-paris-saclay.fr/2021/01/18/thrustme-successful-space-test-for-the-first-electric-iodine-propulsion-system/ (cit. on p. 9).

[20] Busek. *Bit-3 Datasheet*. URL: https://www.busek.com/bit3 (cit. on p. 9).

[21] Hiroki Kawahara et al. "Ground experiment for the small unified propulsion system: I-COUPS installed on the small space probe: Procyon." In: *Joint Conference of 30th International Symposium on Space Technology and Science, 34th International Electric Propulsion Conference and 6th Nano-satellite Symposium. Hyogo-Kobe, Japan: IEPC, ISTS*. Vol. 201. 2015 (cit. on p. 9).

[22] H Leiter, M Berger, and M Rath. "Evolution of the AIRBUS DS GmbH radio frequency ion thruster family." In: *Proceedings of the Joint Conference of 30th ISTS, 34th IEPC and 6th NSAT, Kobe-Hyogo, Japan*. 2015, pp. 4–10 (cit. on p. 9).

[23] Stephen A Samples and Richard E Wirz. "Development of the MiXI Thruster with the ARCH Discharge." In: *Plasma Research Express* 2.2 (2020), p. 025008 (cit. on p. 9).

[24] Neil A Arthur. "Ion Thruster Produced Roll Torque." In: *AIAA Propulsion and Energy 2019 Forum*. 2019, p. 4166 (cit. on pp. 9, 10).

[25] Hitoshi Kuninaka et al. "Status of Microwave Discharge Ion Engines on Hayabusa Spacecraft." In: *43rd AIAA/ASME/SAE/ASEE Joint Propulsion Conference & Exhibit*. 2007, p. 5196 (cit. on pp. 9, 10).

[26] Elena Tremolizzo, Helmut Meier, and Denis Estublier. "In-flight disturbance torque evaluation of the smart-1 plasma thruster." In: *Proceedings of the 18th International Symposium on Space Flight Dynamics*. Vol. 548. 2004, pp. 303–306 (cit. on p. 9).

[27] John R Brophy, Charles E Garner, and Steven C Mikes. "Dawn ion propulsion system: Initial checkout after launch." In: *Journal of Propulsion and Power* 25.6 (2009), pp. 1189–1202 (cit. on p. 9).

[28] VACCO. *CubeSat Propulsion Systems from VACCO Industries*. URL: https://cubesat-propulsion.com/ (cit. on p. 11).

[29]   Nano Avionics. *CubeSat Magnetorquer SatBus MTQ*. URL: https://nanoavionics.com/cubesat-components/cubesat-magnetorquer-satbus-mtq/ (cit. on p. 11).

[30]   Michael Tsay et al. "Flight development of iodine BIT-3 RF ion propulsion system for SLS EM-1 CubeSats." In: (2016) (cit. on p. 12).

[31]   Joakim Kugelberg et al. "Accommodating electric propulsion on SMART-1." In: *Acta Astronautica* 55.2 (2004), pp. 121–130 (cit. on p. 12).

[32]   David Pidgeon et al. "Two Years of On-Orbit Performance of SPT-100 Electric Propulsion." In: *24th AIAA International Communications Satellite Systems Conference*. 2006, p. 5353 (cit. on p. 12).

[33]   Thomas Randolph et al. "Three-Axis Electric Propulsion Attitude Control System with a Dual-Axis Gimbaled Thruster." In: *47th AIAA/ASME/SAE/ASEE Joint Propulsion Conference & Exhibit*. 2011, p. 5586 (cit. on pp. 13, 34).

[34]   F Landis Markley and John L Crassidis. *Fundamentals of spacecraft attitude determination and control*. Springer, 2014 (cit. on p. 14).

[35]   Andrei Kornienko et al. "Disturbance Torque Compensation of the BepiColombo Spacecraft during Interplanetary Cruise Flight using Solar Sailing Effect." In: *AIAA Guidance, Navigation, and Control (GNC) Conference*. 2013, p. 5120 (cit. on p. 14).

[36]   Yaroslav Mashtakov, Stepan Tkachev, and Mikhail Ovchinnikov. "Use of external torques for desaturation of reaction wheels." In: *Journal of Guidance, Control, and Dynamics* 41.8 (2018), pp. 1663–1674 (cit. on p. 15).

[37]   Naohiro Hayashi et al. "Attitude Control and Angular Momentum Unloading of Spacecraft only with Reaction Wheels and Solar Radiation Pressure Torque." In: *The 23rd Workshop on JAXA Astrodynamics and Flight Mechanics*. 2013, p. 75 (cit. on p. 15).

[38]   Nazareth S Bedrossian et al. "Zero-propellant maneuver guidance." In: *IEEE Control Systems Magazine* 29.5 (2009), pp. 53–73 (cit. on p. 16).

[39]   Siddharth Kedare and Steve Ulrich. "Formulation of Torque-Optimal Guidance Trajectories for a CubeSat with Degraded Reaction Wheels." In: *AIAA Guidance, Navigation, and Control Conference*. 2016, p. 0088 (cit. on p. 16).

[40]   Jesse Pietz and Nazareth Bedrossian. "Momentum dumping using only CMGs." In: *2003 AIAA GN&C Conference*. 2003, pp. 11–13 (cit. on p. 16).

[41]   Francesco Topputo et al. "Envelop of reachable asteroids by M-ARGO CubeSat." In: *Advances in Space Research* 67.12 (2021), pp. 4193–4221 (cit. on p. 19).

[42]   V Franzese et al. "Deep-Space Optical Navigation for M-ARGO Mission." In: *The Journal of the Astronautical Sciences* (2021), pp. 1–22 (cit. on p. 19).

[43]   ESA. *5th ESA CubeSat Industry Days*. URL: https://atpi.eventsair.com/QuickEventWebsitePortal/5thcubesatindustrydays/website (cit. on pp. 22, 24, 26).

[44]   GomSpace. *NanoPower MSP*. URL: https://gomspace.com/shop/subsystems/power/msp-solar-panels.aspx (cit. on p. 22).

115

[45] Meike List et al. "Modelling of solar radiation pressure effects: Parameter analysis for the microscope mission." In: *International Journal of Aerospace Engineering* 2015 (2015) (cit. on p. 23).

[46] Sodern. *Auriga CP Datasheet*. URL: https://www.sodern.com/sodern_virtual_ booth/Virtual_Visit/our_products/auriga_cp/index.html (cit. on p. 25).

[47] GomSpace. *NanoSense FSS Datasheet*. URL: https://gomspace.com/shop/subsystems/ attitude-orbit-control-systems/nanosense-fss-(1).aspx (cit. on p. 25).

[48] Sensonor. *STIM300 Datasheet*. URL: https://www.sensonor.com/products/inertial- measurement-units/stim300/ (cit. on p. 25).

[49] GomSpace. *NanoTorque GSW-600*. URL: https://gomspace.com/shop/subsystems/ attitude-orbit-control-systems/nanotorque-gsw-600.aspx (cit. on p. 26).

[50] VectorNav. *Attitude Representations*. URL: https://www.vectornav.com/resources/ inertial-navigation-primer/math-fundamentals/math-attituderep (cit. on p. 29).

[51] Mathworks. *Stateflow*. URL: https://www.mathworks.com/products/stateflow. html (cit. on p. 53).

[52] Mathworks. *Simulink*. URL: https://www.mathworks.com/products/simulink.html (cit. on p. 58).

[53] James R Wertz. *Spacecraft attitude determination and control*. Vol. 73. Springer Science & Business Media, 2012 (cit. on p. 59).

[54] William Premerlani and Paul Bizard. "Direction cosine matrix imu: Theory." In: *Diy Drone: Usa* (2009), pp. 13–15 (cit. on p. 60).

[55] Wikipedia. *List of moments of inertia*. URL: https://en.wikipedia.org/wiki/List_ of_moments_of_inertia (cit. on p. 61).

[56] Rajib Kumar Bhattacharjya. *ME 101: Engineering Mechanics L19-21*. URL: https: //www.iitg.ac.in/rkbc/me101/Presentation/L19-21.pdf (cit. on p. 61).

[57] AR Abdulghany. "Generalization of parallel axis theorem for rotational inertia." In: *American Journal of Physics* 85.10 (2017), pp. 791–795 (cit. on p. 62).

[58] SpaceWeatherLive. *The Interplanetary Magnetic Field (IMF)*. URL: https://www. spaceweatherlive.com/en/help/the-interplanetary-magnetic-field-imf. html (cit. on p. 64).

[59] David González et al. "Modelling and Simulation of Very Low Earth Orbits." In: *8th European Conference for Aeronautics and Space Sciences (EUCASS)*. 2019 (cit. on p. 65).

[60] Jozef Van der Ha and Daniele Stramaccioni. "Thermal Radiation Effects on Deep-Space Trajectories." In: *Advances in the Astronautical Sciences* 136 (Jan. 2010), pp. 1861–1880 (cit. on p. 65).

[61] Honeybee Robotics. *Solar Array Drive Assemblies*. URL: https://www.honeybeerobotics. com/products/solar-array-drive-assemblies/ (cit. on p. 68).

[62] Alberto Bemporad et al. "The explicit linear quadratic regulator for constrained systems." In: *Automatica* 38.1 (2002), pp. 3–20 (cit. on p. 76).

[63] DART. *DART Team*. URL: https://dart.polimi.it/team/ (cit. on p. 95).

[64] NAIF. *SPICE Toolkit*. URL: https://naif.jpl.nasa.gov/naif/toolkit.html (cit. on p. 95).

[65] C Steiger et al. "BepiColombo–solar electric propulsion system operations for the transit to Mercury." In: *36th International Electric Propulsion Conference*. 2019 (cit. on p. 112).

[66] Anton Lindner et al. "Solar Orbiter Solar Array - Exceptional Design for a Hot Mission." In: *2019 European Space Power Conference (ESPC)*. 2019, pp. 1–7. DOI: 10.1109/ESPC.2019.8932039 (cit. on p. 112).

List of Figures

List of Tables